

ABSTRACT

CLEAVES, HELEN LARRABEE. Global Sensitivity Analysis and Reduced Order Modeling for High-dimensional Systems. (Under the direction of Alen Alexanderian.)

Global sensitivity analysis (GSA) is an area of uncertainty quantification that provides methods for quantifying how the uncertainty in the output of mathematical models is connected to the uncertainties in the input parameters. GSA methods are commonly used to identify influential and non-influential model parameters. Understanding which parameters have the most impact on the output provides valuable insight and can guide input dimension reduction. A sizable portion of existing GSA techniques focus on the sensitivity analysis of quantities of interest (QoIs) that are scalar, deterministic, or have a modest number of input parameters. However, there are many practical, real-world models that do not fall into these categories. Thus, the unifying goal of this thesis is to investigate GSA in the context of lesser-studied QoIs. We develop derivative-based GSA theory and computational methods for 1) function-valued QoIs, 2) QoIs with high-dimensional input parameters and 3) stochastic QoIs. The proposed computational methods utilize spectral representations to exploit problem structure and produce efficient, scalable numerical methods for GSA. The utility of the proposed techniques and computational methods are demonstrated in the context of a diverse set of physical and biological systems governed by differential equations. Specific applications include epidemiology, subsurface flow, biotransport, and molecular dynamics.

© Copyright 2021 by Helen Larrabee Cleaves

All Rights Reserved

Global Sensitivity Analysis and Reduced Order Modeling for High-dimensional Systems

by
Helen Larrabee Cleaves

A dissertation submitted to the Graduate Faculty of
North Carolina State University
in partial fulfillment of the
requirements for the Degree of
Doctor of Philosophy

Applied Mathematics

Raleigh, North Carolina

2021

APPROVED BY:

Pierre Gremaud

Ralph Smith

Richard Longland

Alen Alexanderian
Chair of Advisory Committee

DEDICATION

To my parents, Faunce and Margaret, who have always loved and supported me.

BIOGRAPHY

Helen Cleaves grew up in Piermont, New Hampshire and later pursued a Bachelor of Science degree in Mathematics at The University of San Francisco in San Francisco, California. Following the completion of her Bachelors degree she moved to Raleigh to attend North Carolina State University. She received her Masters in 2018 and PhD in 2021. While in the graduate program, she participated in an internship at Sandia National Laboratories.

ACKNOWLEDGEMENTS

Firstly, I would like to thank my advisor for his unwavering help and support as well as the members of my committee, Pierre Gremaud, Ralph Smith, and Richard Longland for their guidance. I would also like to acknowledge the financial support of the National Science Foundation through the grant DMS-1745654 as well as that of the North Carolina Department of Mathematics. I am grateful for the opportunity and experience provided by my internships at Sandia National Labs and my internship mentor Mark Wilson. Finally, I would like to thank my friends, including the entirety of the LB108 basement (past and present). If I had to do it again, I definitely wouldn't do it without you.

TABLE OF CONTENTS

LIST OF TABLES	vii
LIST OF FIGURES	viii
Chapter 1 INTRODUCTION	1
1.1 Survey of literature and existing approaches	2
1.2 Outline of thesis	3
Chapter 2 BACKGROUND	6
2.1 Sobol indices for scalar outputs	6
2.2 Derivative-based global sensitivity measures	10
2.3 Karhunen Loève expansions	12
Chapter 3 GLOBAL SENSITIVITY ANALYSIS FOR VECTORIAL QUANTITIES OF INTEREST	14
3.1 Introduction	14
3.2 Vectorial Sobol' indices	15
3.3 DGSMs for vectorial QoIs	17
3.4 Active subspace methods for vectorial QoIs	18
3.5 A motivating application problem	20
3.6 Conclusions	22
Chapter 4 DERIVATIVE-BASED GLOBAL SENSITIVITY ANALYSIS FOR MOD- ELS WITH HIGH-DIMENSIONAL INPUTS AND FUNCTIONAL OUT- PUTS	24
4.1 Introduction	24
4.2 Preliminaries	25
4.2.1 The basic setup	25
4.2.2 Variance-based sensitivity analysis for functional outputs	26
4.2.3 Functional Sobol' indices	27
4.3 Derivative-based GSA for functional QoIs	29
4.4 Adjoint-based GSA for models governed by elliptic PDEs	35
4.5 Numerical examples	39
4.5.1 Sensitivity analysis for a model of cholera epidemics	39
4.5.2 Sensitivity analysis in a subsurface flow problem	42
4.5.3 Application to biotransport in tumors	47
4.6 Conclusions	52
Chapter 5 GLOBAL SENSITIVITY DRIVEN INPUT DIMENSIONALITY REDUC- TION FOR REAXFF PARAMETERIZATIONS OF SILICA-BASED GLASSES	55
5.1 Introduction	55
5.2 ReaxFF parameters and QoIs	56
5.3 Numerical results	58
5.4 Conclusions	60

Chapter 6	STRUCTURE EXPLOITING METHODS FOR FAST UNCERTAINTY QUANTIFICATION IN MULTIPHASE FLOW THROUGH HETEROGENEOUS MEDIA	61
6.1	Introduction	61
6.2	Model description	65
6.2.1	Mathematical formulation of the continuous problem.	65
6.2.2	Numerical solver	67
6.2.3	Numerical experiment	67
6.3	Modeling under uncertainty	69
6.3.1	Modeling uncertainty in material properties	70
6.3.2	The QoIs under study	71
6.4	Spectral representations of random processes	72
6.4.1	Karhunen Loève expansions	72
6.4.2	Polynomial chaos expansions for $f_i(\boldsymbol{\theta})$.	73
6.4.3	Bispectral surrogates	74
6.5	Method	76
6.5.1	Parameter screening	76
6.5.2	Polynomial chaos surrogates for KL modes	79
6.5.3	Correlation structure of the output	80
6.6	Numerical results	82
6.6.1	Gas saturation at the outflow boundary	82
6.6.2	Gas flux at the outflow boundary	86
6.6.3	Gas saturation across the domain	87
6.6.4	Using the surrogate model	89
6.7	Conclusion	93
Chapter 7	SENSITIVITY ANALYSIS FOR STOCHASTICALLY FORCED DIFFERENTIAL EQUATIONS	94
7.1	Introduction	94
7.2	Random ordinary differential equations	95
7.3	Motivating application	99
7.4	Methods	101
7.4.1	Smooth random functions for approximating noise in dynamical systems	101
7.4.2	Derivative-based global sensitivity analysis	104
7.4.3	Analytical investigations of $\nu_j^{(1)}$	105
7.5	Numerical results	107
7.5.1	Derivative-based GSA for the GBM forcing term	107
7.5.2	Derivative-based GSA for the OU forcing term	110
7.6	Conclusion	110
Chapter 8	CONCLUSION	112

LIST OF TABLES

Table 3.1	Standard deviation of the components f_i , $i = 1, \dots, 5$	22
Table 4.1	Cholera model parameters from [6, 51].	40
Table 4.2	Model parameters for the biotransport problem.	48
Table 5.1	Summary of the studied QoIs, corresponding x units, and involved parameters. Note that for QoIs B_{ij} , and A_{ijk} , $i, j, k \in \{1, 2\}$, the inclusion of certain subsets of θ_{ij}^{od} , θ_{ijk}^{ag} , and θ_{ijkl}^t in θ depends on the compound being modeled.	57
Table 5.2	List of studies performed in this work. Each quantity of interest (QoI), isolated (single) atom energy ($S_i(\theta)$) radial bond energy ($B_{ij}(x, \theta)$), angular bending energy ($A_{ijk}(x, \theta)$) is listed with their respective varied parameters, total number of samples (N_s), total non-influential parameters, and number of samples with LAMMPS errors (N_e). Subscripts denote atom types, where 1 represents O and 2 represents Si.	59
Table 6.1	Left: parameter values for the porous medium and fluid characteristics used in test case 1. Right: parameter values for domain size, boundary and initial conditions, total injection time and total simulation time. . .	68
Table 6.2	Surrogate parameter values and e_{rel} errors for surrogate models.	88
Table 7.1	Model parameters for (7.11) [36].	100
Table 7.2	Noise parameter values used to simulate $\mathbf{z}(t, \theta, \omega)$ in (7.11).	100
Table 7.3	Columns left to right: noise type, wave number, seconds compute one smooth white noise sample, seconds to compute one realizations of noise term, seconds to solve one realization of x_1 from system in (7.11).	102

LIST OF FIGURES

Figure 3.1	Classical total Sobol' indices for each f_i , $i = 1, \dots, 5$, and the vectorial indices (the last panel). Dashed line corresponds to $S_j = 0.05$	21
Figure 3.2	Comparison of pdfs for full (blue) and reduced (red) model; the reduced model has $\theta_1, \theta_2, \theta_3, \theta_4$, and θ_5 fixed at nominal values, last panel: the impact of fixing inessential variables on standard deviation of the system components.	22
Figure 4.1	The infected population $I(t; \theta)$ with $\theta = 0$	40
Figure 4.2	Pointwise-in-time DGSMs $v_j(I(t, \cdot))$ (left) and functional DGSMs $\mathfrak{R}_j(I; [0, t])$ (right) for $t \in [0, 150]$	42
Figure 4.3	Left: The functional Sobol indices and the corresponding bounds proven in Theorem 4.3.1 for the cholera model; right: the same information as in the left plot, except we use log-scale on y -axis to clearly show $\mathfrak{S}_j^{\text{tot}}(I; \mathcal{X})$ and the corresponding bound, for small indices; the dashed black line indicates $y = 0.05$ that could be a reasonable tolerance to decide which random input is unimportant.	42
Figure 4.4	Mean log-permeability field. The black dots indicate point source locations.	43
Figure 4.5	Left: the normalized eigenvalues of the log-permeability field covariance operator; right: the ratios r_k , for $k = 1, \dots, 1000$	44
Figure 4.6	Realizations of the log-permeability field (left), and the corresponding pressure fields (right).	45
Figure 4.7	A few realizations of the QoI (left), eigenvalues of the output covariance operator versus those of the log-permeability field (middle). Eigenvalues of the output covariance, with successively larger MC samples sizes for computing the output KLE (right).	45
Figure 4.8	Left: DGSM-based bound in (Theorem 4.3.1) calculated for various sample sizes. Right: standard deviation fields for full model versus that of the reduced model.	46
Figure 4.9	pdf estimate for equally spaced points, $[-1, 1]$	47
Figure 4.10	The domain \mathcal{D} . The inner and outer boundaries are equipped with Neumann and Dirichlet boundary conditions and are denoted by Γ_N and Γ_D , respectively.	48
Figure 4.11	The functional DGSM-based bounds of pressure fields in a tumor with uncertain permeability. Top left: Convergence study with the MC sample size $N_{MC} = 500, 750$, and 1500 . Top right: Comparison of DGSM-based bounds for different annulus sizes, namely the annulus outer radii of 1 mm , 2 mm , and 3 mm . Bottom left: Comparison of DGSM-based bounds for different correlation lengths, namely 0.5 mm , 1 mm , and 2 mm . Bottom right: DGSM-based bounds calculated with different combinations of the KLE dimensions of the input and output.	51
Figure 4.12	Distribution of the points where PDFs of pressures are extracted, and the corresponding RSD field (contour).	52

Figure 4.13	Comparison of PDFs constructed from the DGSM-based ROM (left column) and KL-based ROM (right column) with variable fidelity at points P_1 , P_2 and P_3	53
Figure 6.1	A schematic of the proposed <i>bispectral</i> surrogate modeling approach. .	62
Figure 6.2	Gas saturation (left) and liquid and gas pressures (right) at the inflow boundary.	69
Figure 6.3	Liquid (left) and gas (right) flux at the outflow boundary.	69
Figure 6.4	Left: the porosity permeability relation and the distributions of point-wise porosity and permeability. Right: a few realizations of the porosity field.	71
Figure 6.5	A few realizations of the time evolution of left: gas saturation at the inflow boundary, right: gas flux at the outflow boundary.	72
Figure 6.6	Left: gas saturation at $t^* = 300,091$ years, right: space time evolution of gas saturation.	72
Figure 6.7	Fifty point comparison of the true model to the linear model for $S(t, \theta)$ at left: $t = 400,234$ years, middle: $t = 500,106$ years. Right: screening indices s_j for $S(t, \theta)$ calculated using Algorithm 3 with 500 full QoI samples. Scores above $tol = 0.002$ displayed only.	83
Figure 6.8	Left: comparison of ratio λ_k/λ_1 , $k = 1 \dots, 30$ for $\lambda_i(C_{qoi})$ corresponding to $S(t, \theta)$ computed with various sample sizes, right: r_k as defined in (2.9), $k = 1, \dots, 10$, for $S(t, \theta)$. Dotted line corresponds to 0.99.	83
Figure 6.9	Left: cross validation results for $\tau = \{1, 1.1, \dots, 3.9, 4\}$ and $N_{ord} = \{1, 2, 3, 4\}$ for gas saturation, right: comparison of sample standard deviations of $S(t, \theta)$ and $S_{N_{qoi}}^{PC}(t, \theta^r)$ computed on 200 sample points.	84
Figure 6.10	Comparison of normalized histograms for $S(t, \theta)$ and pdf estimates of the surrogate $S_{N_{qoi}}^{PC}(t, \theta^r)$ for a variety of times $t \in [0, T_f]$	85
Figure 6.11	Left: comparison of the true model to the linear model for $Q(t, \theta)$ at $t = 500,106$ years, middle: screening indices for $Q(t, \theta)$, right: comparison of sample standard deviations of $Q(t, \theta)$ and $Q_{N_{qoi}}^{PC}(t, \theta^r)$ computed with 200 sample points.	86
Figure 6.12	Comparison of normalized histograms for $Q(t, \theta)$ and pdf estimates of the surrogate $Q_{N_{qoi}}^{PC}(t, \theta^r)$ for a variety of times $t \in [0, T_f]$	87
Figure 6.13	Results for $S(x, \theta; t^*)$ with $t^* = 600,043$ years. Left: comparison of the true model and the linear model for gas saturation across the domain, middle: screening indices for $S(x, \theta; t^*)$, right: ratio λ_k/λ_1 , $k = 1, \dots, 30$ for $\lambda_k(C_{qoi})$ corresponding to $S(x, \theta; t^*)$	89
Figure 6.14	Top row, left to right: sample realizations of $S(x, \theta; t^*)$ for times 100,099, 300,091, and 600,043 years; bottom row, left to right: comparison of sample standard deviation of $S(x, \theta; t^*)$ and $S_{N_{qoi}}^{PC}(x, \theta; t^*)$ computed on 200 sample points.	89
Figure 6.15	Comparison of normalized histograms and pdf estimates for left: max saturation value of S_{max} , middle: first time $S_{N_{qoi}}^{PC}(t, \theta^r)$ is above 20% S_{max} , right: max flux value Q_{max}	90
Figure 6.16	From top left counter clockwise: functional total Sobol' indices for $S_{N_{qoi}}^{PC}(t, \theta^r)$, functional total Sobol' indices for $Q_{N_{qoi}}^{PC}(t, \theta^r)$, total Sobol' indices for S_{max} , total Sobol' indices for Q_{max}	91

Figure 6.17	Left: correlation matrix for $S_{N_{\text{qoi}}}^{\text{PC}}(t, \theta^r)$ computed using the analytic formula in (6.24), middle: correlation matrix for $Q_{N_{\text{qoi}}}^{\text{PC}}(t, \theta^r)$ computed using the analytic formula in (6.24) right: cross-correlation structure of $S_{N_{\text{qoi}}}^{\text{PC}}(t, \theta^r)$ and $Q_{N_{\text{qoi}}}^{\text{PC}}(t, \theta^r)$ computed using the analytic formula in (6.25).	92
Figure 7.1	Left to right: GBM realizations when $\mu < -\sigma^2/2$, $\mu = -\sigma^2/2$, and $\mu > -\sigma^2/2$, with initial valued $X_0 = 5$	97
Figure 7.2	Realizations of the OU process for various k , and $\mu = 35$, $X_0 = 5$, and $\sigma = 1$	98
Figure 7.3	Flow of lead in and out of the human body.	99
Figure 7.4	Top row: comparison of realizations for $x_1(t, \theta, \omega)$ with GBM noise computed with $\lambda = 0.1$ (black) and $\lambda = 10$ (red). Bottom row: comparison of realizations for $x_1(t, \theta, \omega)$ with OU noise computed with $\lambda = 0.1$ (black) and $\lambda = 10$ (red).	103
Figure 7.5	Top: mean (left) and standard deviation (right) comparison of $x_1(t, \theta, \omega)$ with $N_\Omega = 1,000$ simulations of the GBM noise computed with $\lambda = 0.1$ (black) and $\lambda = 10$ (red). Bottom: mean (left) and standard deviation (right) comparison of $x_1(t, \theta, \omega)$ with $N_\Omega = 1,000$ simulations of the OU noise computed with $\lambda = 0.1$ (black) and $\lambda = 10$ (red).	104
Figure 7.6	Left: a few realizations of the noise term L constructed with a GBM, right: corresponding trajectories of x_1	108
Figure 7.7	Estimated pdfs for $\bar{v}_j^{(2)}$, $j = 1, \dots, N_p$, computed with $N_\Omega = 1,000$ samples.	109
Figure 7.8	Comparison of normalized DGSMs $\bar{v}_j^{(1)}$ (black) and median of $\bar{v}_j^{(2)}$ (red) estimated for x_1 with GBM forcing term. Dashed line corresponds to $tol = 0.05$	109
Figure 7.9	Left: a few realizations of the noise term L constructed with the OU process, middle: corresponding trajectories of x_1 , right: comparison of normalized DGSMs for $\bar{v}_j^{(1)}$ (black) and median of $\bar{v}_j^{(2)}$ (red) estimated for x_1 with OU forcing term. Results above 7×10^{-3} displayed only.	110

Scientists formulate systems of interconnected mathematical equations to model real-world phenomena. These mathematical models provide a tangible means for studying the processes they emulate. For example, models can be used to run simulations, make predictions, or guide experimental design. However, the insights gained through modeling are only as reliable as the models they are informed by. In practice, many models have uncertainties in both inputs and outputs. Mathematical tools are needed for understanding how these uncertainties impact model behavior. Global sensitivity analysis (GSA) provides tools for addressing this challenge.

GSA methods apportion the uncertainties in the output of mathematical models to the uncertainties in the input model parameters [90]. There are a variety of applications for GSA. For example, GSA can be used to inform input dimension reduction, enable risk assessment, and guide model development. Traditionally, GSA methods have been developed for scalar quantities of interest (QoIs). However, scientific progress has generated increasingly intricate mathematical systems. Many such models give rise to high-dimensional input parameters, QoIs that are vector-valued (or *vectorial*), or time- or space-dependent QoIs (referred to as *function-valued* or *functional* QoIs). Furthermore, due in part to increased complexity, such systems can be computationally expensive to simulate or perform GSA upon. The motivation for the research presented in this thesis is the development of efficient GSA methods for lesser-studied QoIs, with an emphasis on QoIs with high-dimensional inputs and outputs that are expensive to compute. We also explore GSA for stochastic QoIs.

At-a-glance. In this thesis we present generalizations of traditional derivative-based GSA approaches for the cases of vectorial QoIs and functional QoIs. Additionally, we examine a known relationship between derivative-based and variance-based GSA techniques for scalar QoIs and generalize this relation for the cases of vectorial QoIs and functional QoIs. Also

explored is derivative-based GSA for stochastic QoIs. We present numerical methods for computing the proposed GSA tools. The numerical procedures for the functional, deterministic QoIs achieve efficiency by exploiting model structure via spectral representations. We demonstrate the effectiveness of the developed GSA approaches and computational methods by performing numerical studies on QoIs arising from systems of differential equations. For a more extensive summary of material covered and contributions see section 1.2.

1.1 Survey of literature and existing approaches

A great amount of progress has been made in theory and numerical methods for variance-based GSA over the past three decades [31, 41, 42, 59, 69, 84, 90, 91, 99–102, 104]. The variance-based GSA tools considered most often in the present work are the Sobol’ indices [91, 99, 100]. Detailed for scalar, vector-valued, and function-valued QoIs in sections 2.1, 3.2, and 4.2 respectively, Sobol’ indices apportion percentages of the total QoI variance to variations in input parameters. Techniques for estimating classical Sobol’ indices have been explored in [78, 83, 88, 89, 92].

There are a number of recent efforts targeting variance-based GSA for vectorial or functional QoIs. Specifically, the works [6, 20, 41, 61, 108] discuss variance-based GSA for vectorial and functional outputs. Similar to their scalar counterparts, computing variance-based GSA measures for functional QoIs is computationally challenging. The computational challenges can be reduced significantly by employing surrogate models [3, 6, 31, 46, 94, 104]. However, surrogate model construction itself becomes computationally challenging for models with high-dimensional input parameters.

An alternative to Sobol’ indices are Shapley values [79, 80, 103]. Similar to Sobol’ indices, Shapley values determine the relative importance of parameters based on impact to the output variance. Shapley values are especially popular for models with dependent parameters. However, the cost of estimating Shapely values often exceeds the cost of computing the Sobol’ indices.

Variance-based GSA emphasizes the second moment of the QoI. However, the variance does not always characterize the behavior of a distribution sufficiently. The moment-independent importance measures [9, 16, 17] address this shortcoming. The works [16, 17] compare the QoI distribution and the QoI distribution conditioned on a subset of the input variables. The sensitivity measures constructed in [9] examine the loss entropy of the output. Moment-independent importance measures can be informative, however, in practice they can be expensive to estimate.

Another well-studied GSA approach is derivative-based analysis. Generally cheaper to estimate than variance-based measures, derivative-based measures are often useful for identifying unimportant inputs. In the present thesis, we focus on the derivative-based global sen-

sitivity measures (DGSMs) proposed in [59, 101]. For models with statistically independent inputs, DGSMs can be used to bound the total Sobol’ indices [60, 101]. We discuss DGSMs for scalar, vector-valued, and function-valued QoIs in sections 2.2, 3.3, and 4.3, respectively.

The active subspace method [27–29] and the corresponding activity scores are another set of popular derivative-based GSA tools. The active subspace quantifies the directions in the input parameter space along which the QoI varies most. The activity scores provide approximate screening indices by utilizing the information gained from the active subspace computations. In particular, the authors of [28] show that activity scores can be used to approximate the DGSMs. While active subspace methods have mostly targeted scalar QoIs, the recent works [54, 114] generalize these methods to vectorial outputs. Further details for active subspaces for vectorial and functional outputs are discussed in sections 3.3 and 6.5.

Closely related to derivative-based GSA is the parameter screening method referred to as Morris screening [53, 72]. This approach involves sampling a finite-difference approximation of the partial derivative of the output with respect to the input parameters at randomly chosen points in the parameter space. Morris screening can be an effective and efficient approach to input dimension reduction for expensive to evaluate QoIs after which more informative GSA techniques can be deployed.

1.2 Outline of thesis

This section is an overview of the research and contributions of this thesis. A large portion of the research contained in the upcoming chapters is either published or submitted for publication. Specifically, the work accomplished in chapter 4 is based on the article [25], published in the SIAM Journal on Scientific Computing, the efforts reported in chapter 5 are peer-reviewed and published in the CSRI Summer 2020 Proceedings [85], and the efforts detailed in chapter 6 have been collected into a manuscript and submitted to a peer-reviewed journal [26].

CHAPTER 2: BACKGROUND. In this chapter, we review definitions and properties of Sobol’ indices and DGSMs for scalar QoIs. Also covered in this chapter is the Karhunen–Loève expansion—a spectral decomposition instrumental to the computational methods in both chapter 4 and 6.

CHAPTER 3: GLOBAL SENSITIVITY ANALYSIS FOR VECTORIAL QUANTITIES OF INTEREST. We review variance-based GSA for vectorial outputs and extend derivative-based methods for vectorial QoIs. We present numerical results to illustrate the value of generalizing GSA techniques for vectorial QoIs.

Contributions. GSA for vector-valued QoIs is a natural intermediate step between GSA for scalar QoIs and the GSA methods developed in chapter 4 for functional QoIs. This chapter studies variance-based GSA and introduces derivative-based GSA for vectorial outputs. Additionally, we prove the proposed generalization of the DGSMs produces the vectorial

equivalent of the upper bound on the total Sobol' index proven in [60, 101] for scalar QoIs. We also discuss approximation of the vectorial DGSMs via activity scores. We estimate the generalized total Sobol indices for an application problem describing a genetic feedback loop.

CHAPTER 4: DERIVATIVE-BASED GLOBAL SENSITIVITY ANALYSIS FOR MODELS WITH HIGH-DIMENSIONAL INPUTS AND FUNCTIONAL OUTPUTS

We present a framework for derivative-based GSA for models with high-dimensional input parameters and functional outputs. We combine ideas from derivative-based GSA, random field representation via Karhunen–Loève expansions, and adjoint-based gradient computation to provide a scalable computational framework for computing the proposed derivative-based GSA measures. We illustrate the strategy for a nonlinear ODE model of cholera epidemics and for elliptic PDEs with application examples from geosciences and biotransport.

Contributions. In this chapter, we develop suitable extensions of DGSMs for functional QoIs. We adhere to the generalization for the Sobol' indices proposed in [6, 41] and prove the DGSM extension can be used to form an upper bound on the functional total Sobol' index. Furthermore, we present a framework for efficient computation of the functional DGSM-based bound that combines a low-rank Karhunen–Loève expansion representation of the functional QoI with adjoint-based gradient computation. Additionally, we present a comprehensive set of numerical results. In particular, we consider three application problems (i) a nonlinear system of ODEs modeling the spread of cholera [51] (ii) a problem motivated by porous medium flow [1], and (iii) an application problem involving biotransport in tumors [5]. For (i) we numerically compare the DGSM-based upper bound with the functional total Sobol' indices. In (ii) we implement the proposed adjoint-based numerical framework to assess parametric sensitivities of the pressure field on a domain boundary. Lastly, in (iii) we perform a similar analysis for QoI corresponding to the pressure distribution in certain subdomains of a tumor model.

CHAPTER 5: GLOBAL SENSITIVITY DRIVEN INPUT DIMENSIONALITY REDUCTION FOR REAXFF PARAMETERIZATIONS OF SILICA-BASED GLASSES

Accuracy of classical atomistic molecular dynamics (MD) simulations originates from the quality of the interatomic potential, defining pair-wise atomic energetic interactions. The reactive force field, ReaxFF is an example of a complex potential having multiple contributions to the system energy and therefore multiple parameters to define the potential. In an effort to understand the relationships between these parameters and simulated properties, we deploy a global sensitivity analysis approach to screen these parameters and to guide input dimension reduction.

Contributions. In this chapter, we compute the functional DGSMs defined in chapter 4 to screen the input parameters for QoIs corresponding to a system of reactive potentials. We analyze a variety of QoIs arising from the energetic interactions between silicon and oxygen in the context of silica-based glasses. We include a set of numerical results which reveal several non-influential parameters of the studied energetic properties.

CHAPTER 6: STRUCTURE EXPLOITING METHODS FOR FAST UNCERTAINTY QUANTIFICATION IN MULTIPHASE FLOW THROUGH HETEROGENEOUS MEDIA In this chapter, we present a computational framework for dimension reduction and surrogate modeling to accelerate uncertainty quantification in computationally intensive models with high-dimensional inputs and function-valued outputs. The driving application is multiphase flow in saturated-unsaturated porous media in the context of radioactive waste storage [18, 19]. We demonstrate the effectiveness of the proposed surrogate modeling approach with a comprehensive set of numerical experiments, where we consider a number of function-valued (temporally or spatially distributed) QoIs.

Contributions. Our proposed methods are applicable to a broad class of problems involving systems for which gradient evaluation exceeds the computational budget. We provide a comprehensive overview of the motivation application. We propose a fast-to-compute, gradient-free, screening metric that utilizes ideas from active subspaces [27] to perform initial parameter dimension reduction. Following parameter screening, we combine two different spectral approaches to generate an efficient surrogate model in a reduced-dimensional uncertain parameter space. We refer to this surrogate as the *bispectral surrogate*. Additionally, a variety of statistical studies are conducted with the constructed bispectral surrogate to showcase the versatility of the surrogate model. In particular, we perform model predictions, compute variance-based global sensitivity indices, and study statistical model response behavior. Our computational results also provide valuable insight regarding the response of complex porous media flow models to uncertainties in material properties.

CHAPTER 7: SENSITIVITY ANALYSIS FOR STOCHASTICALLY FORCED DIFFERENTIAL EQUATIONS We focus on derivative-based GSA for stochastic QoIs. Specifically, we examine stochastically forced differential equations that give rise to random ordinary differential equations (RODEs). We demonstrate the proposed derivative-based GSA methods in the context of an RODE with a stochastic source term, describing the flow lead in the human body.

Contributions. We use both analytical and numerical techniques to highlight the subtleties of incorporating stochasticity into GSA. We accomplish this by proposing and investigating two possible DGSMs. The two proposed DGSMs measure different properties of the QoI. We emphasize that the viability of a particular DGSM formulation depends on the QoI being investigated and the sensitivity information desired. We advocate for a numerical approach for solving RODEs that is inspired by the work done in [38] and relies on smooth approximations of a random processes. A major benefit of the deployed scheme is that the resulting RODEs can be solved using traditional numerical methods for ODEs, while maintaining standard convergence rates. The proposed numerical method is also straight-forward to implement.

CHAPTER 8: CONCLUSION In this final chapter, we provide concluding remarks and directions for future work.

Background material for this thesis is covered in this chapter. We discuss Sobol' and total Sobol' indices for scalar quantities of interest (QoIs) in section 2.1. Definitions and properties for derivative-based global sensitivity measures (DGSMs) for scalar QoIs are presented in section 2.2. Lastly, in section 2.3, we present details for the Karhunen Loève expansion (KLE)—a spectral decomposition utilized in the computational methods proposed in chapter 4 and chapter 6.

2.1 Sobol indices for scalar outputs

Sobol' indices are variance-based global sensitivity measures used to rank the relative influence of input parameters. The information presented in this section is primarily drawn from [91, 99, 100, 102].

Let $\boldsymbol{\theta} = [\theta_1 \dots \theta_{N_p}]^T$ be the uncertain parameter vector that takes values in $\Theta \subseteq \mathbb{R}^{N_p}$. Throughout this thesis, we will abuse notation by denoting both the uncertain variable and its realizations by the same symbol $\boldsymbol{\theta}$. We consider the probability space $(\Theta, \mathcal{B}, \mu)$, where \mathcal{B} is the Borel σ -algebra on Θ and μ is the law of the uncertain parameter vector $\boldsymbol{\theta}$. In the present work, Θ is of the form $\Theta = \Theta_1 \times \Theta_2 \times \dots \times \Theta_{N_p}$, where $\Theta_j \subseteq \mathbb{R}$, $j = 1, \dots, N_p$. We assume the components of the input parameter vector θ_j , $j = 1, \dots, N_p$, are real-valued, independent random variables and admit probability density functions $\pi_j(\theta_j)$, in which case

$$\mu(d\boldsymbol{\theta}) = \prod_{j=1}^{N_p} \pi_j(\theta_j) d\theta_j.$$

Next, let $K = \{1, 2, \dots, N_p\}$ be an index set, $U = \{j_1, j_2, \dots, j_m\}$ be a subset of K , and U^c be the

complement of U in K , $U^c = K \setminus U$. We denote $\boldsymbol{\theta}_U = [\theta_{j_1} \ \theta_{j_2} \ \dots \ \theta_{j_m}]^\top$ and consider the scalar QoI $f : \Theta \rightarrow \mathbb{R}$. We denote the *expectation* of f as

$$\mathbb{E}\{f\} = \int_{\Theta} f(\boldsymbol{\theta}) \mu(d\boldsymbol{\theta}).$$

We define the *conditional expectation* of f [98],

$$\mathbb{E}\{f|\boldsymbol{\theta}_U\} = \int_{\Theta_U^c} f(\boldsymbol{\theta}) \mu(d\boldsymbol{\theta}_{U^c}).$$

where

$$\Theta_U^c = \prod_{j \in U^c} \Theta_j, \quad \text{and} \quad \mu(d\boldsymbol{\theta}_{U^c}) = \prod_{j \in U^c} \pi_j(\theta_j) d\theta_j.$$

Now, we consider the following decomposition for f

$$f(\boldsymbol{\theta}) = f_0 + \sum_{\substack{U \subseteq K \\ U \neq \emptyset}} f_U(\boldsymbol{\theta}_U). \quad (2.1)$$

Where the f_U 's are functions of only the corresponding parameter set $\boldsymbol{\theta}_U$. Since the components of $\boldsymbol{\theta}$ are independent we have that for each f_U [100]

$$\int_{\Theta_j} f_U \pi_j(\theta_j) d\theta_j = 0, \quad \text{for all } j \in U.$$

Consequently, the f_U 's are pairwise orthogonal in $L^2(\Theta)$, and we refer to (2.1) as the ANOVA decomposition of f .

Each term in the summation in (2.1) can then be calculated as

$$\begin{aligned} f_0 &= \mathbb{E}\{f\}, \\ f_{\{i\}} &= \mathbb{E}\{f|\theta_i\} - f_0, \\ f_{\{i, j\}} &= \mathbb{E}\{f|\theta_i, \theta_j\} - f_{\{i\}} - f_{\{j\}} - f_0, \\ &\vdots \\ f_U(\boldsymbol{\theta}_U) &= \mathbb{E}\{f|\boldsymbol{\theta}_U\} - f_0 - \sum_{\substack{V \subseteq U \\ V \neq \emptyset}} f_V(\boldsymbol{\theta}_V). \end{aligned}$$

For clarity, we provide an example. Let $f(\boldsymbol{\theta}) = f(\theta_1, \theta_2, \theta_3)$. Then, the index set is $K = \{1, 2, 3\}$ and we have the following decomposition for f

$$\begin{aligned} f(\theta_1, \theta_2, \theta_3) &= f_0 + f_{\{1\}}(\theta_1) + f_{\{2\}}(\theta_2) + f_{\{3\}}(\theta_3) + \\ &\quad f_{\{1, 2\}}(\theta_1, \theta_2) + f_{\{1, 3\}}(\theta_1, \theta_3) + f_{\{2, 3\}}(\theta_2, \theta_3) + \\ &\quad f_{\{1, 2, 3\}}(\theta_1, \theta_2, \theta_3). \end{aligned}$$

Where

$$\begin{aligned}
f_0 &= E\{f\}, \\
f_{\{1\}} &= E\{f|\theta_1\} - f_0, \\
f_{\{2\}} &= E\{f|\theta_2\} - f_0, \\
f_{\{3\}} &= E\{f|\theta_3\} - f_0, \\
f_{\{1, 2\}} &= E\{f|\theta_1, \theta_2\} - f_0 - f_{\{1\}} - f_{\{2\}}, \\
f_{\{1, 3\}} &= E\{f|\theta_1, \theta_3\} - f_0 - f_{\{1\}} - f_{\{3\}}, \\
f_{\{2, 3\}} &= E\{f|\theta_2, \theta_3\} - f_0 - f_{\{2\}} - f_{\{3\}}, \\
f_{\{1, 2, 3\}} &= E\{f|\theta_1, \theta_2, \theta_3\} - f_0 - f_{\{1\}} - f_{\{2\}} - f_{\{3\}} - f_{\{1, 2\}} - f_{\{1, 3\}} - f_{\{2, 3\}}.
\end{aligned}$$

We take the variance of both sides of (2.1) resulting in the following decomposition of the total variance $D(f) = \text{Var}\{f\}$ of f according to

$$D(f) = \sum_{\substack{U \subseteq K \\ U \neq \emptyset}} D_U(f),$$

where $D_U(f) = E_{\theta_U}\{f_U(\theta_U)^2\}$, with $E_{\theta_U}\{\cdot\}$ indicating expectation with respect to θ_U . Then, we can define the first and total order Sobol' indices as follows:

$$S_U(f) = \frac{D_U(f)}{D(f)} \quad \text{and} \quad S_U^{\text{tot}}(f) = \frac{D_U^{\text{tot}}(f)}{D(f)}, \quad (2.2)$$

where $D(f) > 0$ and

$$D_U^{\text{tot}}(f) = D_U(f) + \sum_{\substack{V \subseteq U \\ V \neq \emptyset}} D_V(f).$$

Note that,

$$S_U^{\text{tot}}(f) = \frac{D(f) - D_{U^c}(f)}{D(f)} = 1 - \frac{D_{U^c}(f)}{D(f)} = 1 - S_{U^c}(f).$$

When the index set U is a singleton, $U = \{j\}$, $j \in \{1, \dots, N_p\}$, we denote the corresponding first and total order Sobol' indices by $S_j(f)$ and $S_j^{\text{tot}}(f)$, respectively.

By construction, the first order Sobol' and total Sobol' indices have the following properties [58]

- i $S_U(f) \in [0, 1]$, $S_U^{\text{tot}}(f) \in [0, 1]$,
- ii $\sum_{\substack{U \subseteq K \\ U \neq \emptyset}} S_U = 1$,
- iii $S_U \leq S_U^{\text{tot}}$.

Properties (i) and (ii) prompt the interpretation of both S_U and S_U^{tot} as the *percentage* the

corresponding parameter sets contribute to the variance of f . The first order Sobol' index $S_U(f)$ represents the portion of the total variance that can be apportioned to θ_U *alone*. On the other hand, the total Sobol' index S_U^{tot} quantifies the variation of f due to θ_U , including the higher order interactions with the other input parameters. If $S_U^{tot} \approx 0$ then the parameters in θ_U are considered *unimportant* or *non-influential*. Consequently, the total Sobol' indices place an ordering on the relative importance of the input parameters using the convention if $S_j^{tot}(f) > S_i^{tot}(f)$ then θ_j is more important than θ_i . The last property (iii) is useful for distinguishing the influence of a parameter (or set of parameters) on their own versus the influence of the higher-order parameter interactions on the total variance of f .

Error estimate for fixing nonessential parameters in scalar QoIs. The total Sobol' index has been linked to the error incurred by fixing a subset of input parameters. In particular, the relative approximation error given by

$$\varepsilon(\theta_U) = \frac{1}{D} \int_{\Theta} (f(\theta) - f(\theta_U, \theta_{U^c}))^2 \mu(d\theta). \quad (2.3)$$

Note, this approximation error is relative to the total variance of the function. Consider the following the theorem proposed by [102],

Theorem 2.1.1. *For an arbitrary θ_U the error $\varepsilon(\theta_U) \geq S_U^{tot}(f)$ and the expected value is $E\{\varepsilon(\theta_U)\} = 2S_U^{tot}(f)$.*

Theorem 2.1.1 further supports the concept of separating the input parameters into important and unimportant sets. Explicitly, fixing important parameters (parameters with a large total Sobol' index) will result in large relative approximation error. Similarly, (on average) fixing unimportant parameters to their nominal value results in only a small changes of the QoI.

Numerical estimation of Sobol' indices is often done using Monte Carlo (MC) or quasi-MC sampling [78, 83, 88, 89, 92]. However, due in part to the sheer number of necessary model evaluations, estimating Sobol' indices via MC integration can become computationally impractical for expensive-to-evaluate QoIs. To mitigate computing costs, it is common to construct a cheap-to-evaluate surrogate model for the QoI and then compute the indices of the surrogate. In particular, polynomial chaos expansion (PCE) surrogates are a popular method for estimating the Sobol' indices; e.g. [4, 15, 31, 104] and section 6.4.2. However, for models with high-dimensional input parameters, the computations required for surrogate model construction can become computationally infeasible.

Many important properties of the classical Sobol' indices rely on the assumption of independent inputs. Methods for addressing the formation and interpretation of Sobol' indices in the context of dependent inputs is an interesting area of research; see e.g. [48, 105, 111]. A related topic is the question of robustness to uncertainty in input distribution. To compute the Sobol' indices we must assume a distribution for each of the input parameters. However, in practice these chosen distributions are often a best guess, as there is not enough information

to determine them exactly. Therefore, to reliably interpret Sobol' indices, we must understand the influence of perturbations in parameter distributions on the computed Sobol' indices; see, e.g., [49, 50].

The index is a valuable GSA tool. In the present thesis we present details on extensions of Sobol' indices for both vector-valued QoIs (Chapter 3) and function-valued QoIs (Chapter 4). Both chapters also include numerical results concerning the corresponding generalized total Sobol' indices computed for real world application problems. Lastly, in Chapter 6, we demonstrate the viability of the constructed bispectral surrogate model by using it to compute the total Sobol' indices of the studied QoIs.

2.2 Derivative-based global sensitivity measures

Derivative-based sensitivity analysis is a prevalent GSA tool for instances when a QoI is differentiable with respect to the input parameters. In practice, derivative-based analysis has been observed to be less expensive than its variance-based counterpart. When gradients can be estimated efficiently, the difference in computational expense makes derivative-based analysis invaluable for models with high-dimensional input parameters. The focus of this section is derivative-based global sensitivity measures (DGSMs) for scalar QoIs. The primary references for this section are [57, 60, 101].

We consider a scalar-valued random variable $f : \Theta \rightarrow \mathbb{R}$. Here f and its partial derivatives are assumed to be square integrable. We focus on the following commonly used DGSM

$$v_j(f) = \int_{\Theta} \left(\frac{\partial f}{\partial \theta_j} \right)^2 \mu(d\theta), \quad j = 1, \dots, N_p. \quad (2.4)$$

Unlike total Sobol' indices (section 2.1), DGSMs *cannot* be used to place an ordering on the relative importance of the input variables. Rather, DGSMs are used to identify *unimportant* input parameters. Intuitively, if $v_j(f)$ is small, it implies the partial derivative does not change 'too much' within the parameter domain, suggesting that changes in θ_j do not substantially impact the QoI. Without further assumptions on the input parameters, analyzing nonlinear systems should be done with caution. Fortunately, for QoIs with independent parameters the intuition that a small $v_j(f)$ implies θ_j is unimportant is justified by the existence of a DGSM-based upper bound on the total Sobol' index [60],

Theorem 2.2.1. *Let f be a scalar random variable satisfying the following assumptions*

- i $f \in L^2(\Theta, \mathcal{B}, \mu)$,
- ii $\frac{\partial f}{\partial \theta_j} \in L^2(\Theta, \mathcal{B}, \mu)$,
- iii The input parameters $\theta_1, \dots, \theta_{N_p}$ are independent random variables, following a Boltzmann measure,

then we have the following DGSM-based upper bound for the total Sobol index

$$S_j^{tot}(f) \leq c_j^p \frac{v_j(f)}{\text{Var}\{f\}}, \quad (2.5)$$

where the constant c_j^p depends on the corresponding pdf for θ_j .

A measure π is a *Boltzmann measure* on \mathbb{R} if it is absolutely continuous with respect to the Lebesgue measure and its density can be expressed as $d\pi(\theta) = ce^{-v(\theta)}d\theta$, where c is a constant and $v(\theta)$ is a continuous function. A non-exhaustive list of Boltzmann distributions includes the normal, exponential, Beta, and Gamma distributions. For a complete list see [60]. The research done in [101] proved the above bound also holds for independent, uniformly distributed input parameters.

In the case of independent inputs, the DGSM-based bound in (2.2.1) can be used as criterion for input parameter dimension reduction. For dependent input variables, the intuitive interpretation of the DGSMs can also be used judiciously to implement input dimension reduction. Once the input parameter space has been reduced, it is common practice to apply more computationally expensive and informative GSA tools (such as Sobol' indices) to the remaining input variables.

The estimation of v_j can be accomplished via a MC sampling procedure. It has been observed in practice that the number of samples required for a sufficiently accurate estimate of v_j 's is less than the number of samples required for Sobol' indices [57]. Naturally, estimating the DGSMs also involves the computation of the partial derivatives for the QoI with respect to the input parameters. This is commonly done via finite-difference, the sensitivity equations (for QoIs originating from systems of differential equations) [68, 93], automatic differentiation, or complex-step methods. For more general QoIs (e.g. vectorial or functional QoIs), systems with expensive model evaluations, large input parameter dimension, or combinations therein, direct estimation of the DGSMs can become computationally expensive. One can also approximate DGSMs via active subspaces and the corresponding activity scores [27, 28].

DGSMs are heavily featured throughout this thesis. In chapter 3, we include details for extending DGSMs to vector-valued QoIs. Also presented in chapter 3, are details for approximating DGSMs via activity scores. In chapter 4, we propose a novel extension of DGSMs for function-valued inputs and present an efficient numerical framework for estimating the functional DGSMs. We compute the DGSMs of a reactive potential model in chapter 5 to identify unimportant model inputs. The relationship between activity scores and DGSMs resurfaces in chapter 6, wherein we use it to justify the proposed method for input parameter screening. Lastly, in chapter 7, we discuss DGSMs for stochastic models.

2.3 Karhunen Loéve expansions

We provide details regarding the Karhunen Loéve expansion (KLE). Throughout this thesis we will utilize KLEs to facilitate efficient GSA computations for function-valued QoIs. A function-valued or functional QoI $f(\boldsymbol{\theta}, s)$, is a function of $\boldsymbol{\theta} \in \Theta$, and $s \in \mathcal{X}$ when \mathcal{X} is a compact set in \mathbb{R}^d , $d = 1, 2, 3$. For models governed by systems of differential equations, \mathcal{X} often represents a temporal or spatial domain.

We assume $f(s, \boldsymbol{\theta})$ is a mean-squared continuous random process. Such processes admit spectral representations, as given by a Karhunen Loéve expansion (KLE) [63, 66]:

$$f(s, \boldsymbol{\theta}) = \bar{f}(s) + \sum_{i=1}^{\infty} \sqrt{\lambda_i} f_i(\boldsymbol{\theta}) \Phi_i(s). \quad (2.6)$$

Here $\bar{f}(s)$ is the mean of the process, (λ_i, Φ_i) are the eigenpairs of the covariance operator \mathcal{C}_{qoi} of the process,

$$\mathcal{C}_{\text{qoi}} \Phi_i = \lambda_i \Phi_i, \quad i = 1, 2, \dots, \quad (2.7)$$

and $f_i(\boldsymbol{\theta})$ are the KL modes,

$$f_i(\boldsymbol{\theta}) = \frac{1}{\sqrt{\lambda_i}} \int_{\mathcal{X}} (f(s, \boldsymbol{\theta}) - \bar{f}(s)) \Phi_i(s) ds, \quad i = 1, 2, 3, \dots \quad (2.8)$$

An approximation $f_{N_{\text{qoi}}}(s, \boldsymbol{\theta})$ to $f(s, \boldsymbol{\theta})$ can be obtained by truncating (2.6) and retaining the first N_{qoi} terms in the series. In many physical and biological models the eigenvalues of \mathcal{C}_{qoi} decay rapidly. Consequently, such QoIs can be represented with sufficient accuracy by a truncated KLE with a small N_{qoi} . We refer to such processes to as “low-rank”.

We rely on Nyström’s method to compute the KLE [56]. This approach, as used throughout the present work, requires sample averaging to approximate the covariance kernel, because we do not in general have a closed-form expression for the output covariance operator. Typically, a modest number of QoI evaluations is sufficient for accurately estimating the dominant eigenpairs of the covariance operator \mathcal{C}_{qoi} . To determine a suitable value for the number N_{qoi} of terms in a truncated KLE, we consider

$$r_k = \frac{\sum_{i=1}^k \lambda_i}{\sum_{i=1}^{\infty} \lambda_i}. \quad (2.9)$$

The quantity r_k represents the fraction of the average variance of f captured by the first k eigenvalues. The steps for computing the truncated KLE of f are included in Algorithm 1, which is adapted from [7]. The truncated KLE of a functional QoI is employed in both chapter 4 and chapter 6.

Algorithm 1 Computing the truncated KLE of f

Input: Quadrature nodes s_k and weights w_k , $k = 1, \dots, m$; Function evaluations $y_k^j = f(s_k, \theta_j)$, $k = 1, \dots, m$, $j = 1, \dots, N_s$; r_k tolerance $0 < tol < 1$.

Output: Eigenpairs (λ_i, Φ_i) of the output covariance operator, and KL modes evaluations $f_i(\theta_j)$, $j = 1, \dots, N_s$, $i = 1, \dots, N_{\text{qoi}}$.

- 1: Compute mean $M_k = \frac{1}{N_s} \sum_{j=1}^{N_s} y_k^j$, $k = 1, \dots, m$.
 - 2: Center process $f_k^c(s_k, \theta_j) = y_k^j - M_k$, $k = 1, \dots, m$.
 - 3: Compute covariance matrix \mathbf{C} .

$$\mathbf{C}_{kl} = \frac{1}{N_s - 1} \sum_{j=1}^{N_s} f_k^c(s_k, \theta_j) f_l^c(s_l, \theta_j), \quad k, l = 1, \dots, m.$$
 - 4: Let $\mathbf{W} = \text{diag}(w_1, w_2, \dots, w_m)$ solve:

$$\mathbf{W}^{1/2} \mathbf{C} \mathbf{W}^{1/2} \mathbf{v}_k = \lambda_k \mathbf{v}_k, \quad k = 1, \dots, m.$$
 - 5: Determine N_{qoi} .
 - 6: **for** $k = 1, \dots, m$ **do**
 - 7: Compute $r_k = \frac{\sum_{l=1}^k \lambda_l}{\sum_{l=1}^m \lambda_l}$.
 - 8: **if** $r_k > tol$ **then**
 - 9: $N_{\text{qoi}} = k$; **BREAK**
 - 10: **end if**
 - 11: **end for**
 - 12: Compute $\Phi_k = \mathbf{W}^{-1/2} \mathbf{v}_k$, $k = 1, \dots, N_{\text{qoi}}$.
 - 13: Compute KL modes.

$$f_i(\theta_j) = \frac{1}{\sqrt{\lambda_i}} \sum_{k=1}^m w_k f_k^c(s_k, \theta_j) \Phi_i(s_k), \quad i = 1, \dots, N_{\text{qoi}}, \quad j = 1, \dots, N_s.$$
 - 14: Compute $f_{N_{\text{qoi}}}(s, \theta_j) = \sum_{k=1}^{N_{\text{qoi}}} \sqrt{\lambda_k} f_i(\theta_j) \Phi_k(s)$.
-

GLOBAL SENSITIVITY ANALYSIS FOR VECTORIAL QUANTITIES OF
INTEREST

3.1 Introduction

A large portion of global sensitivity analysis (GSA) literature deals with scalar-valued functions of independent random inputs. In this chapter, we consider vector-valued quantities of interest (QoIs):

$$\mathbf{y} = \mathbf{f}(\boldsymbol{\theta}), \quad \mathbf{y} \in \mathbb{R}^{N_{\text{qoi}}}, N_{\text{qoi}} > 1. \quad (3.1)$$

GSA for vector-valued QoIs has been the subject of recent works [41, 54, 61, 114]. In the present chapter, we review variance-based GSA for vectorial outputs. Then, we propose suitable generalizations of derivative-based GSA techniques for vectorial outputs, including derivative-based global sensitivity measures (DGSMs) and active subspace methods. Due to the information included, this chapter serves as an informative precursor to the GSA developed for functional QoIs in chapter 4.

The chapter is organized as follows. In section 3.2, we discuss a generalization of the classical Sobol indices for vectorial QoIs and corresponding properties. Similarly, a generalization of the scalar DGSMs is presented in section 3.3. Also in this section, we propose and prove a vectorial DGSM-based upper bound on the vectorial total Sobol' indices. In section 3.4, we discuss active subspace methods for vectorial QoIs, including an approximation for the vectorial DGSMs. Lastly, we compute the vectorial total Sobol' indices for a biochemical feedback loop and present the numerical results in section 3.5. Concluding remarks are given in section 3.6.

3.2 Vectorial Sobol' indices

At first glance, the straight-forward approach for performing GSA on vectorial QoIs of the form (3.1) is to apply scalar QoI techniques to each component f_i , $i = 1, \dots, N_{\text{qoi}}$ separately. However, the interpretation of the results can become difficult as the variance of different components f_i can be drastically different and also different sets of parameters might be important to different components. In section 3.5, a computational example is presented to illustrate such situations.

We consider the following generalization Sobol' indices for vectorial QoIs [41]. First, recall the definitions for Sobol' and Total Sobol' indices given in section 2.1 for which K represents an index set, $U \subseteq K$, and $U^c = K \setminus U$. Now, consider a function $\mathbf{f} : \Theta \rightarrow \mathbb{R}^{N_{\text{qoi}}}$, where $N_{\text{qoi}} > 1$ and $\Theta \subseteq \mathbb{R}^{N_p}$ is the random parameter space.

$$\mathbf{f}(\boldsymbol{\theta}) = \begin{bmatrix} f_1(\boldsymbol{\theta}) \\ f_2(\boldsymbol{\theta}) \\ \vdots \\ f_{N_{\text{qoi}}}(\boldsymbol{\theta}) \end{bmatrix}.$$

Let $\mathbf{\Gamma} \in \mathbb{R}^{N_{\text{qoi}} \times N_{\text{qoi}}}$ be the covariance matrix of the random vector \mathbf{f} . Moreover, let $\mathbf{\Gamma}_U$ be the covariance matrix corresponding to the random vector $\mathbf{E}\{\mathbf{f}|\boldsymbol{\theta}_U\}$. Following [41], we define the first order (vectorial) Sobol' indices as:

$$S_U := \frac{\text{Tr}(\mathbf{\Gamma}_U)}{\text{Tr}(\mathbf{\Gamma})}.$$

It is straightforward to note that

$$S_U(\mathbf{f}) = \frac{\sum_{i=1}^{N_{\text{qoi}}} \text{Var}\{\mathbf{E}\{f_i|\boldsymbol{\theta}_U\}\}}{\sum_{j=1}^{N_{\text{qoi}}} \text{Var}\{f_j\}}.$$

We can analogously define the vectorial total Sobol' indices.

$$S_U^{\text{tot}}(\mathbf{f}) = 1 - S_{U^c}$$

We record the following useful representation of S_U and S_U^{tot} in terms of the classical (coordinatewise) Sobol' indices.

Lemma 3.2.1. *Let $S_U(f_i)$, $S_U^{\text{tot}}(f_i)$ be the classical first order and total Sobol' indices respectively for*

$f_i, i = 1, \dots, N_{\text{qoi}}$, and assume $\text{Var}\{f_i\} > 0, \forall i$. Then, we have

$$\begin{aligned} S_U(\mathbf{f}) &= \sum_{i=1}^{N_{\text{qoi}}} w_i S_U(f_i), \quad U \in K, \quad \text{and,} \\ S_U^{\text{tot}}(\mathbf{f}) &= \sum_{i=1}^{N_{\text{qoi}}} w_i S_U^{\text{tot}}(f_i), \quad U \in K, \end{aligned} \tag{3.2}$$

with $w_i = \text{Var}\{f_i\} / \text{Tr}(\mathbf{\Gamma}), i = 1, \dots, N_{\text{qoi}}$.

Proof. The first statement follows from the following calculation, where we also use $\text{Tr}(\mathbf{\Gamma}) = \sum_{i=1}^{N_{\text{qoi}}} \text{Var}\{f_i\}$:

$$\begin{aligned} \sum_{i=1}^{N_{\text{qoi}}} w_i S_U(f_i) &= \sum_{i=1}^{N_{\text{qoi}}} \left(\frac{\text{Var}\{f_i\}}{\sum_{j=1}^{N_{\text{qoi}}} \text{Var}\{f_j\}} \right) \frac{\text{Var}\{E\{f_i | \boldsymbol{\theta}_U\}\}}{\text{Var}\{f_i\}} \\ &= \frac{\sum_{i=1}^{N_{\text{qoi}}} \text{Var}\{E\{f_i | \boldsymbol{\theta}_U\}\}}{\sum_{j=1}^{N_{\text{qoi}}} \text{Var}\{f_j\}}. \\ &= S_U(\mathbf{f}). \end{aligned}$$

Next, we prove the second statement:

$$\begin{aligned} \sum_{i=1}^{N_{\text{qoi}}} w_i S_U^{\text{tot}}(f_i) &= \sum_{i=1}^{N_{\text{qoi}}} w_i (1 - S_{U^c}(f_i)) \\ &= \sum_{i=1}^{N_{\text{qoi}}} w_i - \sum_{i=1}^{N_{\text{qoi}}} w_i S_{U^c}(f_i) \\ &= \frac{\sum_{i=1}^{N_{\text{qoi}}} \text{Var}\{f_i\}}{\sum_{j=1}^{N_{\text{qoi}}} \text{Var}\{f_j\}} - \sum_{i=1}^{N_{\text{qoi}}} w_i S_{U^c}(f_i) \\ &= 1 - S_{U^c}(\mathbf{f}) = S_U^{\text{tot}}(\mathbf{f}). \end{aligned}$$

Note that the first equality results from a property of the classical scalar Sobol' indices. \blacksquare

The above relationship between vectorial and scalar Sobol' indices is natural. As mentioned previously, simply computing the componentwise Sobol' indices does not account for the impact of the variance of each f_i . The w_i 's address this concern by weighting the componentwise scalar Sobol' indices by their corresponding contribution to the overall variance. Therefore, the representation given in by Lemma 3.2.1 is both insightful and supports the chosen definition for vectorial Sobol' indices as the natural generalization.

The numerical frameworks and computational concerns for the vectorial Sobol' indices are similar to their scalar counterparts (see section 2.1). In particular, for models with high-dimensional input parameters, or expensive to compute QoIs, computing the Sobol' indices via sampling can be infeasible. Analogous to the scalar case, techniques for initial parameter screening and input dimension reduction can help mitigate some of these computational

concerns. In the next section, we discuss definitions and properties of derivative-based global sensitivity measures (DGSMs) for vectorial QoIs.

3.3 DGSMs for vectorial QoIs

Recall from section 2.2, that for scalar QoIs $f : \Theta \rightarrow \mathbb{R}$, the usual DGSMs are given by

$$\nu_j(f) = \int_{\Theta} \left(\frac{\partial f}{\partial \theta_j} \right)^2 \mu(d\boldsymbol{\theta}), \quad j = 1, \dots, N_p.$$

For $f : \Theta \rightarrow \mathbb{R}^{N_{\text{qoi}}}$, we introduce the vectorial DGSMs:

$$\mathcal{N}_j(\mathbf{f}) = \sum_{i=1}^{N_{\text{qoi}}} \int_{\Theta} \left(\frac{\partial f_i}{\partial \theta_j} \right)^2 \mu(d\boldsymbol{\theta}) = \sum_{i=1}^{N_{\text{qoi}}} \nu_j(f_i), \quad j = 1, \dots, N_p. \quad (3.3)$$

The next result illustrates a connection between vectorial total Sobol' indices and vectorial DGSMs. We specifically consider the case where the random inputs are independent, identically distributed (iid) according to either the standard normal distribution or the uniform distribution.

Proposition 3.3.1. *Let $\mathbf{f} : \Theta \rightarrow \mathbb{R}^{N_{\text{qoi}}}$ be a vector-valued random variable and let $\mathbf{\Gamma}$ be its covariance matrix. Assume the random inputs $\theta_1, \dots, \theta_{N_p}$ are iid and distributed according to standard normal distribution or the uniform distribution. Then,*

$$S_j^{\text{tot}}(\mathbf{f}) \leq c_j^p \frac{\mathcal{N}_j(\mathbf{f})}{\text{Tr}(\mathbf{\Gamma})}, \quad j = 1, \dots, N_p$$

where

$$c_j^p = \begin{cases} (b-a)^2 / \pi^2, & \text{if } \theta_j \sim U(a, b), \\ \sigma_j^2, & \text{if } \theta_j \sim \mathcal{N}(0, \sigma_j^2). \end{cases}$$

Proof. Let $D_i = \text{Var}\{f_i\}$. We recall that for a fixed $i \in \{1, \dots, N_{\text{qoi}}\}$, using Theorem 2.2.1,

$$S_j^{\text{tot}}(f_i) \leq c_j^p \frac{\nu_j(f_i)}{D_i},$$

Therefore, using Lemma 3.2.1,

$$S_j^{\text{tot}}(\mathbf{f}) = \sum_{i=1}^{N_{\text{qoi}}} S_j^{\text{tot}}(f_i) w_i \leq \sum_{i=1}^{N_{\text{qoi}}} c_j^p \left(\frac{\nu_j(f_i)}{D_i} \right) \left(\frac{D_i}{\sum_{i=1}^{N_{\text{qoi}}} D_i} \right) = c_j^p \frac{\mathcal{N}_j(\mathbf{f})}{\text{Tr}(\mathbf{\Gamma})}.$$

■

The above result can be extended for independent parameters distributed according to a Boltzmann distribution. Similar to the scalar case discussed in Theorem 2.2.1, a small vectorial

DGSM-based upper bound means the vectorial total Sobol' index is also small, implying the corresponding parameter is non-influential. Thus, the vectorial DGSM-based upper bound can be used to screen input parameters and implement dimension reduction.

3.4 Active subspace methods for vectorial QoIs

As previously mentioned, there is a connection between DGSMs for scalar QoIs and the active subspace [27]. Recall, the active subspace seeks to find low-dimensional subspaces of the uncertain parameter space most influential to variations of the QoI. Active subspaces give rise to the so called *activity scores*. It has been shown that the activity scores can be used to estimate the DGSMs [28]. In this section, we demonstrate that a similar relationship exists for vectorial QoIs.

Approaches to generalize active subspace methods for vectorial QoIs are addressed in [54, 114]. In the present work, we take the following approach. Let $\mathbf{J} \in \mathbb{R}^{N_{\text{qoi}} \times N_p}$ be the Jacobian matrix of \mathbf{f} :

$$J_{ij} = \frac{\partial f_i}{\partial \theta_j}, \quad i = 1, \dots, N_{\text{qoi}}, \quad j = 1, \dots, N_p.$$

We consider the matrix $\mathbf{C} \in \mathbb{R}^{N_p \times N_p}$ given by,

$$\mathbf{C} = \mathbb{E} \{ \mathbf{J}^T \mathbf{J} \}.$$

The symmetric positive semi-definite matrix \mathbf{C} plays a central role in the method of active subspaces. The activity scores are generalized to the vectorial case as follows:

$$\alpha_j(\mathbf{f}; r) = \sum_{k=1}^r \lambda_k \langle \mathbf{e}_j, \mathbf{u}_k \rangle^2, \quad j = 1, \dots, N_p, \quad r \leq N_p, \quad (3.4)$$

where $(\lambda_k, \mathbf{u}_k)$ are the eigenpairs of \mathbf{C} , the \mathbf{e}_i 's are the canonical basis vectors in \mathbb{R}^{N_p} , and the value of r corresponds to the *numerical rank* of \mathbf{C} . The activity scores are most effective if there is a large gap in the eigenvalues, especially in the case when $r \ll N_p$.

To derive a connection between vectorial DGSMs $\mathcal{N}_j(\mathbf{f})$ and the activity scores $\alpha_j(\mathbf{f}, r)$ we first consider the following technical lemma which provides a useful spectral representation of $\mathcal{N}_j(\mathbf{f})$.

Lemma 3.4.1. *We have,*

$$\mathcal{N}_j(\mathbf{f}) = \langle \mathbf{e}_j, \mathbf{C} \mathbf{e}_j \rangle = \sum_{k=1}^{N_p} \lambda_k \langle \mathbf{e}_j, \mathbf{u}_k \rangle^2, \quad j = 1, \dots, N_p,$$

where $\langle \cdot, \cdot \rangle$ denotes the Euclidean inner product, and \mathbf{e}_j is the j th coordinate vector in \mathbb{R}^{N_p} .

Proof. For the first equality consider,

$$\langle \mathbf{e}_j, \mathbf{C} \mathbf{e}_j \rangle = C_{jj} = \sum_{k=1}^{N_p} \mathbb{E} \left\{ \left(\frac{\partial f_k}{\partial \theta_j} \right)^2 \right\} = \mathcal{N}_j(\mathbf{f}).$$

For the second equality, recall the spectral decomposition $\mathbf{C} = \sum_{k=1}^{N_p} \lambda_k \mathbf{u}_k \mathbf{u}_k^\top$. We insert this representation of \mathbf{C} into the first equality to get

$$\begin{aligned} \mathcal{N}_j(\mathbf{f}) &= \langle \mathbf{e}_j, \mathbf{C} \mathbf{e}_j \rangle = \langle \mathbf{e}_j, \left(\sum_{k=1}^{N_p} \lambda_k \mathbf{u}_k \mathbf{u}_k^\top \right) \mathbf{e}_j \rangle \\ &= \sum_{k=1}^{N_p} \lambda_k \langle \mathbf{e}_j, \mathbf{u}_k \rangle \langle \mathbf{u}_k, \mathbf{e}_j \rangle \\ &= \sum_{k=1}^{N_p} \lambda_k \langle \mathbf{e}_j, \mathbf{u}_j \rangle^2. \end{aligned}$$

■

Now, consider the following proposition which formalizes a connection between DGSMs and activity scores for vectorial QoIs.

Proposition 3.4.1. *For each $j \in \{1, \dots, N_p\}$,*

$$\alpha_j(\mathbf{f}; r) \leq \mathcal{N}_j(\mathbf{f}) \leq \alpha_j(\mathbf{f}; r) + \lambda_{r+1}.$$

Proof. Consider,

$$\alpha_j(\mathbf{f}, r) = \sum_{k=1}^r \lambda_k \langle \mathbf{e}_j, \mathbf{u}_k \rangle^2 \leq \sum_{k=1}^{N_p} \lambda_k \langle \mathbf{e}_j, \mathbf{u}_k \rangle^2$$

for $r \leq N_p$. Using the result of Lemma 3.4.1 we have the first inequality. Similarly, the second inequality follows from

$$\begin{aligned} \mathcal{N}_j(\mathbf{f}) &= \sum_{k=1}^{N_p} \lambda_k \langle \mathbf{e}_j, \mathbf{u}_k \rangle^2 \\ &= \sum_{k=1}^r \lambda_k \langle \mathbf{e}_j, \mathbf{u}_k \rangle^2 + \sum_{k=r+1}^{N_p} \lambda_k \langle \mathbf{e}_j, \mathbf{u}_k \rangle^2 \\ &\leq \sum_{k=1}^r \lambda_k \langle \mathbf{e}_j, \mathbf{u}_k \rangle^2 + \lambda_{r+1} \sum_{k=r+1}^{N_p} \langle \mathbf{e}_j, \mathbf{u}_k \rangle^2 \\ &\leq \alpha_j(\mathbf{f}; r) + \lambda_{r+1} \|\mathbf{e}_j\|_2^2 = \alpha_j(\mathbf{f}; r) + \lambda_{r+1}, \end{aligned}$$

and the proof is complete. ■

The utility of this result is realized in problems with high-dimensional parameter spaces

for which the eigenvalues λ_j decay rapidly to zero; in such cases, this result implies that $\mathcal{N}_j(\mathbf{f}) \approx \alpha_j(\mathbf{f}; r)$, for a small r .

3.5 A motivating application problem

In this section, we compute and compare the componentwise total Sobol' indices and the vectorial total Sobol' indices discussed in section 3.2 to analyze a biochemical system modeling a genetic positive feedback loop [11]. The purpose of this study is to demonstrate that computing the componentwise Sobol' indices can lead to hard to interpret results, illustrating the necessity of the vectorial Sobol' indices.

The reaction rate equations. For the present genetic loop mechanism, the reaction rate equations (RREs) describing the concentration of system species in the thermodynamic limit are given by:

$$\begin{aligned}\dot{x} &= 2\theta_2 y - 2\theta_1 x^2 + \theta_7 m - \theta_8 x, \\ \dot{y} &= \theta_1 x^2 - \theta_2 y + \theta_4 d_r - \theta_3 y d_0, \\ \dot{d}_0 &= \theta_4 d_r - \theta_3 y d_0, \\ \dot{d}_r &= \theta_3 y d_0 - \theta_4 d_r, \\ \dot{m} &= \theta_5 d_0 + \theta_6 d_r - \theta_9 m,\end{aligned}$$

where x and y are respectively, the protein monomer and dimer concentrations at time t , the quantity d_0 denotes the concentration of the promoter sites that are free of the dimer, d_r denotes the concentration of the promoter sites that are bound to the protein, and m is the concentration of the mRNA.

The uncertain input is a vector of dimension $N_p = 9$ with entries corresponding to reaction rates. We model the uncertain parameters as $\theta_i = \hat{\theta}_i + 0.1\hat{\theta}_i a_i$, where $a_i \sim \mathcal{U}(-1, 1)$, $i = 1, \dots, N_p$. The nominal values $\hat{\theta}_i$ of these rate constants were taken from [11] and are as follows:

$$\hat{\boldsymbol{\theta}} = \begin{bmatrix} 25 & 1000 & 50 & 1000 & 1 & 10 & 3 & 1 & 6 \end{bmatrix}^T.$$

The initial conditions [11] are given by,

$$x(0) = 10, y(0) = 0, d_0(0) = 20, d_r(0) = 0, m(0) = 0.$$

We consider the state vector,

$$\mathbf{X} = \begin{bmatrix} x & y & d_0 & d_r & m \end{bmatrix}^T,$$

and note that $\mathbf{X} = \mathbf{X}(t; \boldsymbol{\theta})$. The quantity of interest considered here is

$$\mathbf{f}(\boldsymbol{\theta}) = \frac{1}{T_f} \int_0^T \mathbf{X}(t; \boldsymbol{\theta}) dt,$$

where $T_f = 50$ represents the final time.

Vectorial GSA. We begin by computing the componentwise total Sobol' indices, $S_j(f_i)$, for $i = 1, \dots, N_{\text{qoi}}$, $j = 1, \dots, N_p$, as well as the vectorial total Sobol' indices. To do this we use the software package UQtk [32, 33] to construct third order orthogonal polynomial surrogates for each of the components of \mathbf{f} . We then compute the componentwise and vectorial total Sobol' indices with the constructed surrogates, and use the results to approximate the corresponding indices of the QoI. This framework allows for both efficiency, and a high level of accuracy. In panels 1–5 of Figure 3.1 we display the total Sobol' indices for each component of the vector \mathbf{f} . The vectorial total Sobol' indices, $S_j^{\text{tot}}(\mathbf{f})$ are displayed in panel 6 of Figure 3.1. The dashed line in Figure 3.1 corresponds to $S_j = 0.05$. For the componentwise indices, we also report the standard deviation of the respective components in Table 3.1. We observe that the standard deviations of the components of \mathbf{f} have a range of different magnitudes. We also note that the componentwise Sobol' indices have notable variations across components, while vectorial indices provide a common ranking of the parameters.

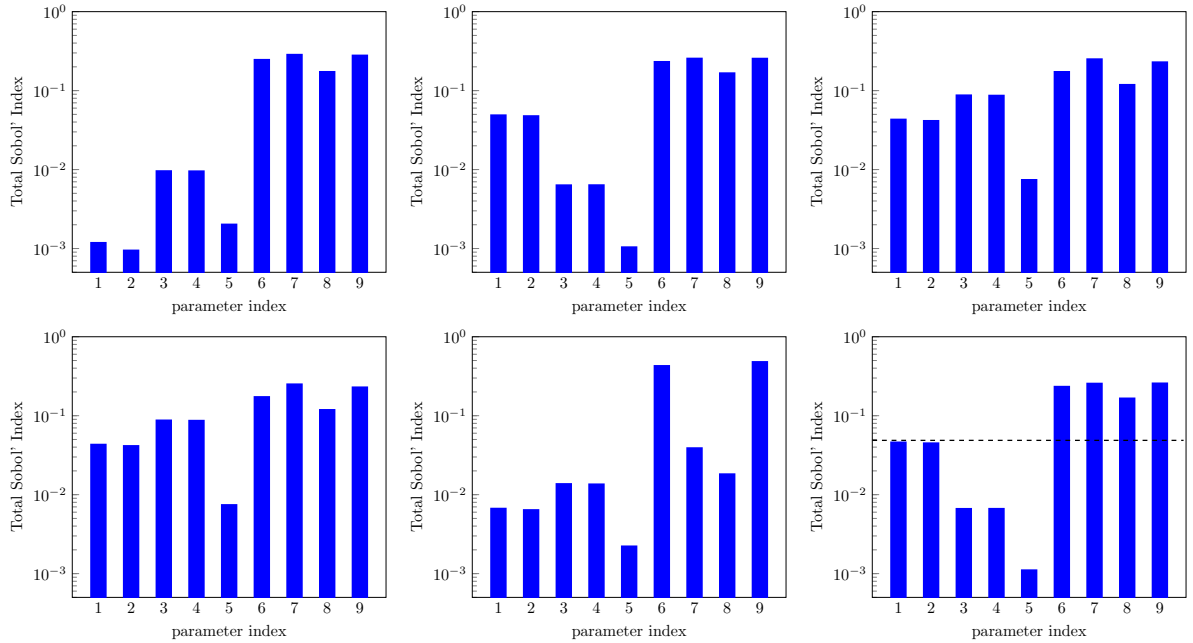


Figure 3.1 Classical total Sobol' indices for each f_i , $i = 1, \dots, 5$, and the vectorial indices (the last panel). Dashed line corresponds to $S_j = 0.05$.

Next, we use the convention that if $S_j^{\text{tot}}(\mathbf{f}) < 0.05$ then the input parameter θ_j is unimportant. The vectorial Sobol' indices in Figure 3.1 indicate that variables θ_i , $i = 1, \dots, 5$ are inessential. We fix this set of parameters to their nominal values and resample the resulting system. We denote the reduced QoI as \mathbf{f}^r . In the first five panels of Figure 3.2, we compare pdfs of the components for \mathbf{f} and \mathbf{f}^r . In the last panel of Figure 3.2 we display the impact of

Table 3.1 Standard deviation of the components f_i , $i = 1, \dots, 5$.

component	f_1	f_2	f_3	f_4	f_5
standard deviation	4.87×10^2	2.02×10^3	41.6	41.6	1.55×10^2

fixing the inessential variables on the standard deviation of each component of \mathbf{f} and \mathbf{f}^r . We observe only minor differences between the results for the full model and the reduced model, indicating that the chosen vectorial Sobol' indices provide an effective method for identifying unimportant variables for an entire vector and can be used to guide model parameter reduction.

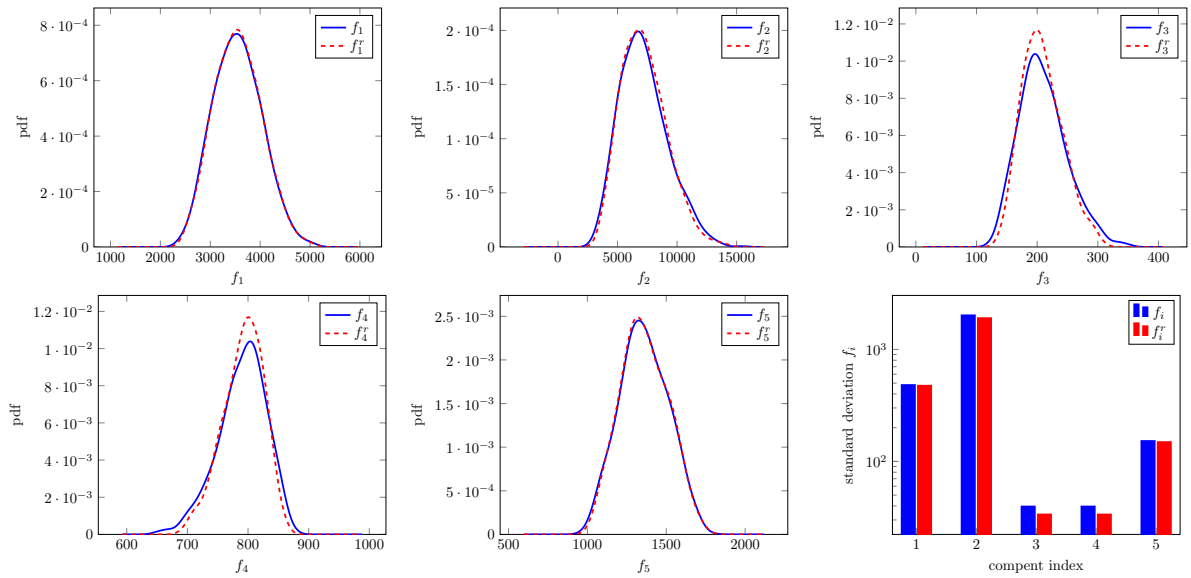


Figure 3.2 Comparison of pdfs for full (blue) and reduced (red) model; the reduced model has $\theta_1, \theta_2, \theta_3, \theta_4$, and θ_5 fixed at nominal values, last panel: the impact of fixing inessential variables on standard deviation of the system components.

The next logical step is to compute the DGSM-based upper bound proven in Proposition 3.3.1 and compare it to the vectorial total Sobol' indices. However, in chapter 4 we present a variety of detailed numerical illustrations of the DGSM-based upper bound for function-valued QoIs. Therefore, to avoid repetition we omit this type of study in the present chapter.

3.6 Conclusions

We have presented two different GSA approaches for vectorial QoIs. In section 3.2, we gave definitions for both the vectorial first order and total Sobol' indices, as well as demonstrat-

ing their connection with the classic Sobol' indices for scalar QoIs. We presented vectorial DGSMs in section 3.3. Their connection to active subspaces and activity scores was discussed, based on a convenient spectral representation [Proposition 3.4.1]. We proposed using vectorial DGSMs as a method for input parameter screening, and justified this claim by proving a vectorial analog of the DGSM-based bound from section 2.2. We computed the vectorial Sobol' indices in section 3.5 for a biology-based application problem modeling a genetic positive feedback loop. The findings of this chapter indicate the presented generalization of classical GSA techniques are both natural and necessary.

DERIVATIVE-BASED GLOBAL SENSITIVITY ANALYSIS FOR MODELS WITH HIGH-DIMENSIONAL INPUTS AND FUNCTIONAL OUTPUTS

The contents of this chapter is related to the work published in [25]. The author of the present thesis is also lead author on this paper. We would like to give special thanks to our collaborators Meilin Yu, Ralph Smith, and Hayley Guy for their contributions.

4.1 Introduction

In this chapter, we consider mathematical models of the form

$$y = f(s, \boldsymbol{\theta}), \tag{4.1}$$

where s belongs to a compact set $\mathcal{X} \subset \mathbb{R}^d$ with $d = 1, 2$, or 3 , and $\boldsymbol{\theta}$ is an element of an uncertain parameter space $\Theta \subseteq \mathbb{R}^{N_p}$. We present a mathematical framework for derivative-based global sensitivity analysis (GSA) for *functional* quantities of interest (QoIs) of the form (4.1) and present a scalable computational framework for computing the corresponding derivative-based GSA measures. We focus on models with independent random input parameters. Moreover, in our target applications, $f(s, \boldsymbol{\theta})$ is defined in terms of the solution of a system of differential equations.

We begin our developments by defining a suitable derivative-based global sensitivity measure (DGSM) for functional QoIs, in section 4.3, and prove that it provides a computable bound for the generalized total Sobol' indices for functional QoIs as defined in [6, 41]; see Theorem 4.3.1. Next, we present a framework for efficient computation of the functional DGSMs that uses low-rank representation of the functional QoIs via truncated Karhunen–Loève expansions (KLEs) [63]. Expressions for DGSMs, and DGSM-based bounds on functional total

Sobol' indices for a truncated KLE are established in Theorem 4.3.2 (an introduction to KLEs is also included in section 2.3 of this thesis). The DGSMs of the approximate models, given by truncated KLEs, are then computed using adjoint-based gradient computation. This approach is elaborated for models governed by linear elliptic PDEs in section 4.4.

Additionally, we present a comprehensive set of numerical results that illustrate various aspects of the proposed approach and demonstrate its effectiveness. We consider three application problems: (i) a nonlinear system of ODEs modeling the spread of cholera [51], where we perform GSA for the infected population as a function of time (section 4.5.1); (ii) a problem motivated by porous medium flow applications, with permeability data adapted from [1], where we assess parametric sensitivities of the pressure field on a domain boundary (section 4.5.2); and (iii) an application problem involving biotransport in tumors [5], where we consider the pressure distribution in certain subdomains of a tumor model (section 4.5.3).

Chapter overview. This chapter is structured as follows. In section 4.2, we set up the notation used throughout the chapter, and collect the assumptions on the functional QoIs under study. We also provide findings for variance-based GSA for functional QoIs, following the developments in [6, 41], in section 4.2. In section 4.3 we present a mathematical framework for derivative-based GSA of functional QoIs. We elaborate our proposed adjoint-based framework for models governed by linear elliptic PDEs in section 4.4. This is followed by our computational experiments that are detailed in section 4.5. Finally, we provide some concluding remarks in section 4.6.

4.2 Preliminaries

4.2.1 The basic setup

We recall the probability space $(\Theta, \mathcal{B}, \mu)$ as it is defined in 2.1. Next, let $\mathcal{X} \subset \mathbb{R}^d$, with $d = 1, 2$, or 3 be a compact set. With this setup, we consider a process, $f : \mathcal{X} \times \Theta \rightarrow \mathbb{R}$, satisfying the following assumptions.

Assumption 4.2.1. *We assume*

1. $f \in L^2(\mathcal{X} \times \Theta)$ and f is mean square continuous; that is, for any sequence $\{s_n\}$ in \mathcal{X} converging to $s \in \mathcal{X}$ we have that $\lim_{n \rightarrow \infty} \mathbb{E} \{ [f(s_n, \boldsymbol{\theta}) - f(s, \boldsymbol{\theta})]^2 \} = 0$,
2. $\frac{\partial f}{\partial \theta_j}(s, \boldsymbol{\theta})$ is defined for all $s \in \mathcal{X}$ and $\boldsymbol{\theta} \in \Theta$, $j = 1, \dots, N_p$,
3. $\frac{\partial f}{\partial \theta_j}(s, \boldsymbol{\theta}) \in L^2(\mathcal{X} \times \Theta)$, $j = 1, \dots, N_p$,
4. and $\{\theta_j\}_{j=1}^{N_p}$ are real-valued independent random variables, and have distribution laws that are absolutely continuous with respect to the Lebesgue measure.

We remark that (a) is a fundamental assumption on the process f . From this, we can conclude continuity of the mean and covariance function of the process; see, e.g., Theorem

7.3.2 in [52] and Theorem 2.2.1 in [2]. This in turn facilitates application of Mercer's Theorem [62, 71] (needed below) and implies that f admits a KLE [66]. The assumptions (b) and (c) are needed in the context of derivative-based global sensitivity analysis. Note that, Assumption 4.2.1(b) can be relaxed by requiring $\frac{\partial f}{\partial \theta_j}(s, \boldsymbol{\theta})$ be defined almost everywhere in $\mathcal{X} \times \Theta$.

4.2.2 Variance-based sensitivity analysis for functional outputs

We first recall the classical Sobol' indices and Analysis of Variance (ANOVA) decomposition discussed in section 2.1, which can be defined pointwise in \mathcal{X} . We again let $K = \{1, 2, \dots, N_p\}$ be an index set, let $U = \{j_1, j_2, \dots, j_m\}$ be a subset of K , and let U^c be the complement of U in K , $U^c = K \setminus U$. We denote $\boldsymbol{\theta}_U = \{\theta_{j_1}, \theta_{j_2}, \dots, \theta_{j_m}\}$. For each $s \in \mathcal{X}$, we have the ANOVA decomposition [102]

$$f(s, \boldsymbol{\theta}) = f_0(s) + f_1(s, \boldsymbol{\theta}_U) + f_2(s, \boldsymbol{\theta}_{U^c}) + f_{12}(s, \boldsymbol{\theta}), \quad (4.2)$$

where f_0 is the mean of the process, and

$$f_1(s, \boldsymbol{\theta}_U) = E\{f(s, \cdot) | \boldsymbol{\theta}_U\} - f_0(s), \quad f_2(s, \boldsymbol{\theta}_{U^c}) = E\{f(s, \cdot) | \boldsymbol{\theta}_{U^c}\} - f_0(s),$$

and $f_{12}(s, \boldsymbol{\theta}) = f(s, \boldsymbol{\theta}) - f_0(s) - f_1(s, \boldsymbol{\theta}_U) - f_2(s, \boldsymbol{\theta}_{U^c})$. This enables decomposing the total variance $D(f; s) = \text{Var}\{f(s, \cdot)\}$ of $f(s, \cdot)$ according to

$$D(f; s) = D_U(f; s) + D_{U^c}(f; s) + D_{U, U^c}(f; s),$$

where $D_U(f; s) = E_{\boldsymbol{\theta}_U}\{f_1(s, \boldsymbol{\theta}_U)^2\}$, $D_{U^c}(f; s) = E_{\boldsymbol{\theta}_{U^c}}\{f_2(s, \boldsymbol{\theta}_{U^c})^2\}$, and $D_{U, U^c}(f; s)$ is the remainder. (Here $E_{\boldsymbol{\theta}_U}\{\cdot\}$ indicates expectation with respect to $\boldsymbol{\theta}_U$.) Then, we can define the first and total Sobol' indices as follows:

$$S_U(f; s) = \frac{D_U(f; s)}{D(f; s)} \quad \text{and} \quad S_U^{\text{tot}}(f; s) = \frac{D_U^{\text{tot}}(f; s)}{D(f; s)},$$

where $D_U^{\text{tot}}(f; s) = D_U(f; s) + D_{U, U^c}(f; s)$. Note that,

$$S_U^{\text{tot}}(f; s) = \frac{D(f; s) - D_{U^c}(f; s)}{D(f; s)} = 1 - \frac{D_{U^c}(f; s)}{D(f; s)} = 1 - S_{U^c}(f; s).$$

When the index set U is a singleton, $U = \{j\}$, $j \in \{1, \dots, N_p\}$, we denote the corresponding first and total Sobol' indices by $S_j(f; s)$ and $S_j^{\text{tot}}(f; s)$, respectively.

Here we assume that $D(f; s) > 0$ almost everywhere in \mathcal{X} . If $D(f; s) = 0$ for some $s \in \mathcal{X}$, we use the convention $S_U(f; s) = 0$.

4.2.3 Functional Sobol' indices

Following [6, 41], we define the functional first order Sobol' index as

$$\mathfrak{S}_U(f; \mathcal{X}) = \frac{\int_{\mathcal{X}} D_U(f; s) ds}{\int_{\mathcal{X}} D(f; s) ds}.$$

The following lemma provides a simple representation for the functional Sobol' index in terms of the pointwise classical Sobol' indices:

Lemma 4.2.1. *We have $\mathfrak{S}_U(f; \mathcal{X}) = \int_{\mathcal{X}} S_U(f; s) w(s) ds$, with $w(s) = \frac{D(f; s)}{\int_{\mathcal{X}} D(f; y) dy}$.*

Proof. The result follows by a straightforward calculation. ■

We can also define the functional total Sobol' indices

$$\mathfrak{S}_U^{\text{tot}}(f; \mathcal{X}) = \frac{\int_{\mathcal{X}} D_U^{\text{tot}}(f; s) ds}{\int_{\mathcal{X}} D(f; s) ds} = 1 - \mathfrak{S}_{U^c}(f; \mathcal{X}).$$

Using Lemma 4.2.1, we note

$$\mathfrak{S}_U^{\text{tot}}(f; \mathcal{X}) = 1 - \mathfrak{S}_{U^c}(f; \mathcal{X}) = \int_{\mathcal{X}} (1 - S_{U^c}(f; s)) w(s) ds = \int_{\mathcal{X}} S_U^{\text{tot}}(f; s) w(s) ds. \quad (4.3)$$

Error estimates for functional Sobol indices. Recall, we can use the total Sobol' index of a parameter to rank its importance. In particular, parameters with small Sobol' indices can be deemed unimportant. In this section, we briefly discuss the impact of fixing these unimportant parameters in terms of approximation errors. Let $U = \{j_1, j_2, \dots, j_m\} \subset \{1, \dots, N_p\}$ index the set of important parameters, and suppose we set θ_{U^c} to a nominal vector $\boldsymbol{\eta}$. Consider the “reduced” model:

$$f^{(\boldsymbol{\eta})}(s, \boldsymbol{\theta}_U) = f(s, \boldsymbol{\theta}_U, \boldsymbol{\eta}),$$

where the right hand side function is understood to be $f(s, \boldsymbol{\theta})$, with entries of $\boldsymbol{\theta}_{U^c}$ fixed at $\boldsymbol{\eta}$.

For $U = \{j_1, j_2, \dots, j_m\}$ we define $\Theta_U = \Theta_{j_1} \times \dots \times \Theta_{j_m}$. Integration on Θ_U will be with respect to $\mu(d\boldsymbol{\theta}_U) = \prod_{k=1}^m \pi_{j_k}(\theta_{j_k}) d\theta_{j_k}$.

For $\boldsymbol{\eta} \in \Theta_{U^c}$ we define the mean-square error

$$\varepsilon(f; s; \boldsymbol{\eta}) = \int_{\Theta} (f(s, \boldsymbol{\theta}) - f^{(\boldsymbol{\eta})}(s, \boldsymbol{\theta}_U))^2 \mu(d\boldsymbol{\theta}).$$

We consider the relative mean square error

$$\mathcal{E}(f; \boldsymbol{\eta}) = \frac{\int_{\mathcal{X}} \int_{\Theta} (f(s, \boldsymbol{\theta}) - f^{(\boldsymbol{\eta})}(s, \boldsymbol{\theta}_U))^2 \mu(d\boldsymbol{\theta}) ds}{\int_{\mathcal{X}} \int_{\Theta} f(s, \boldsymbol{\theta})^2 \mu(d\boldsymbol{\theta}) ds}. \quad (4.4)$$

This provides a measure of the error that occurs when fixing the values of $\boldsymbol{\theta}_{U^c}$. Next, consider the following key lemma, which is based on the arguments in [102].

Lemma 4.2.2. *For every $s \in \mathcal{X}$, $\int_{\Theta_{U^c}} \varepsilon(f; s; \boldsymbol{\eta}) \mu(d\boldsymbol{\eta}) = 2D_{U^c}^{\text{tot}}(f; s)$.*

Proof. Let $s \in \mathcal{X}$ be fixed. Consider the ANOVA decomposition of $f(s, \boldsymbol{\theta})$, as defined in (4.2):

$$f(s, \boldsymbol{\theta}) = f_0(s) + f_1(s, \boldsymbol{\theta}_U) + f_2(s, \boldsymbol{\theta}_{U^c}) + f_{12}(s, \boldsymbol{\theta}_U, \boldsymbol{\theta}_{U^c}).$$

By substituting this into the expression for $\varepsilon(f; s; \boldsymbol{\eta})$ and simplifying we have

$$\varepsilon(f; s; \boldsymbol{\eta}) = \int_{\Theta} [f_2(s, \boldsymbol{\theta}_{U^c}) + f_{12}(s, \boldsymbol{\theta}_U, \boldsymbol{\theta}_{U^c}) - f_2(s, \boldsymbol{\eta}) - f_{12}(s, \boldsymbol{\theta}_U, \boldsymbol{\eta})]^2 \mu(d\boldsymbol{\theta}). \quad (4.5)$$

Using the properties of ANOVA [100, 102],

$$\int_{\Theta_{U^c}} f_2(s, \boldsymbol{\theta}_{U^c}) \mu(d\boldsymbol{\theta}_{U^c}) = \int_{\Theta_{U^c}} f_{12}(s, \boldsymbol{\theta}_U, \boldsymbol{\theta}_{U^c}) \mu(d\boldsymbol{\theta}_{U^c}) = \int_{\Theta_U} f_{12}(s, \boldsymbol{\theta}_U, \boldsymbol{\theta}_{U^c}) \mu(d\boldsymbol{\theta}_U) = 0,$$

we can simplify (4.5) to get, for a fixed $\boldsymbol{\eta} \in \Theta_{U^c}$,

$$\begin{aligned} \varepsilon(f; s; \boldsymbol{\eta}) &= \int_{\Theta} [f_2^2(s, \boldsymbol{\theta}_{U^c}) + f_{12}^2(s, \boldsymbol{\theta}_U, \boldsymbol{\theta}_{U^c}) + f_2^2(s, \boldsymbol{\eta}) + f_{12}^2(s, \boldsymbol{\theta}_U, \boldsymbol{\eta})] \mu(d\boldsymbol{\theta}) \\ &=_{U^c} (f; s) + D_{U^c, U}(f; s) + f_2^2(s, \boldsymbol{\eta}) + \int_{\Theta_U} f_{12}^2(s, \boldsymbol{\theta}_U, \boldsymbol{\eta}) \mu(d\boldsymbol{\theta}_U). \end{aligned}$$

Integrating the above expression over Θ_{U^c} gives the desired result. ■

The following proposition quantifies the error in (4.4) in terms of the functional total Sobol' indices. This result is a straightforward modification of the error estimate presented in [6]; we provide a proof for completeness.

Proposition 4.2.1. $\int_{\Theta_{U^c}} \mathcal{E}(f; \boldsymbol{\eta}) \mu(d\boldsymbol{\eta}) \leq 2\mathfrak{S}_{\boldsymbol{\theta}_{U^c}}^{\text{tot}}(f, \mathcal{X})$.

Proof. First note that the denominator is a constant and

$$\int_{\mathcal{X}} \int_{\Theta} f(s, \boldsymbol{\theta})^2 \mu(d\boldsymbol{\theta}) ds = \int_{\mathcal{X}} \left[D(f; s) + \left(\int_{\Theta} f(s, \boldsymbol{\theta}) \mu(d\boldsymbol{\theta}) \right)^2 \right] ds \geq \int_{\mathcal{X}} D(f; s) ds. \quad (4.6)$$

Next, consider the expectation of the numerator in (4.4):

$$\begin{aligned} \int_{\Theta_{U^c}} \int_{\mathcal{X}} \int_{\Theta} (f(s, \boldsymbol{\theta}) - f^{(\boldsymbol{\eta})}(s, \boldsymbol{\theta}_U))^2 \mu(d\boldsymbol{\theta}) ds \mu(d\boldsymbol{\eta}) &= \int_{\Theta_{U^c}} \int_{\mathcal{X}} \varepsilon(f; s; \boldsymbol{\eta}) ds \mu(d\boldsymbol{\eta}) \\ &= \int_{\mathcal{X}} \int_{\Theta_{U^c}} \varepsilon(f; s; \boldsymbol{\eta}) \mu(d\boldsymbol{\eta}) ds = 2 \int_{\mathcal{X}} D_{U^c}^{\text{tot}}(f; s) ds, \end{aligned} \quad (4.7)$$

where changing the order of integration is justified by Tonell's theorem, and the last equality follows from Lemma 4.2.2. The desired result follows from (4.7) and (4.6). ■

The estimate in Proposition 4.2.1 says that when fixing $\boldsymbol{\theta}_{U^c}$ to a nominal parameter $\boldsymbol{\eta} \in \Theta_{U^c}$, in average, the relative error $\mathcal{E}(f; \boldsymbol{\eta})$ is bounded by $2\mathfrak{E}_{\boldsymbol{\theta}_{U^c}}^{\text{tot}}(f, \mathcal{X})$.

4.3 Derivative-based GSA for functional QoIs

Let us first consider a scalar-valued random variable $g : \Theta \rightarrow \mathbb{R}$. Here g and its partial derivatives are assumed to be square integrable. We recall from section 2.2 the following commonly used DGSM:

$$v_j(g) = \int_{\Theta} \left(\frac{\partial g}{\partial \theta_j} \right)^2 \mu(d\boldsymbol{\theta}).$$

DGSMs can be used to screen for unimportant variables. This is justified by the relation between DGSMs and total Sobol' indices, which was first addressed in [101] for scalar-valued random variables. While the estimation of v_j requires a Monte Carlo (MC) sampling procedure, it has been observed that in practice the number of samples required for estimation of v_j 's does not need to be very large to provide sufficient accuracy in identifying unimportant variables [57]. We present the following result which partially explains this phenomenon.

Proposition 4.3.1. *Assume that*

$$a_j \leq \left(\frac{\partial g}{\partial \theta_j}(\boldsymbol{\theta}) \right)^2 \leq b_j, \quad j = 1, \dots, N_p, \quad \text{for all } \boldsymbol{\theta} \in \Theta.$$

Consider the MC estimator

$$v_j^{(N_{MC})}(g) := \frac{1}{N_{MC}} \sum_{k=1}^{N_{MC}} \left(\frac{\partial g}{\partial \theta_j}(\boldsymbol{\theta}^k) \right)^2,$$

with $\boldsymbol{\theta}^k$ independent and identically distributed according to the law of $\boldsymbol{\theta}$. Then,

$$\text{Var} \left\{ v_j^{(N_{MC})}(g) \right\} \leq \frac{1}{N_{MC}} (b_j - v_j(g)) (v_j(g) - a_j) \leq \frac{1}{4N_{MC}} (b_j - a_j)^2, \quad (4.8)$$

for $j = 1, \dots, N_p$.

Proof. We recall the following result: if a random variable X satisfies $a \leq X \leq b$ and $\mathbb{E}\{X\} = m$, then

$$\text{Var}\{X\} \leq (b - m)(m - a) \leq (b - a)^2/4. \quad (4.9)$$

The first inequality is known as the Bhatia–Davis inequality [14]. The second inequality gives a corollary of the Bhatia–Davis inequality, known as Popoviciu's inequality, that says $\text{Var}\{X\} \leq (b - a)^2/4$, for a random variable satisfying $a \leq X \leq b$. Note that clearly $a_j \leq v_j(g) \leq b_j$, for $j = 1, \dots, N_p$. Applying the inequality (4.9) with $X = \left(\frac{\partial g}{\partial \theta_j} \right)^2$ and $(b, m, a) = (b_j, v_j(g), a_j)$, $j = 1, \dots, N_p$, we obtain $\text{Var} \left\{ \left(\frac{\partial g}{\partial \theta_j} \right)^2 \right\} \leq (b_j - v_j(g)) (v_j(g) - a_j) \leq \frac{1}{4} (b_j - a_j)^2$. Therefore, for

$j = 1, \dots, N_p,$

$$\text{Var} \left\{ v_j^{(N_s)}(g) \right\} = \frac{1}{N_s} \text{Var} \left\{ \left(\frac{\partial g}{\partial \theta_j} \right)^2 \right\} \leq \frac{1}{N_s} (b_j - v_j(g)) (v_j(g) - a_j) \leq \frac{1}{4N_s} (b_j - a_j)^2.$$

■

This proposition says that if the partial derivatives do not vary 'too much' (i.e., a_j and b_j are not too far from one another), indicating a desirable regularity property of the parameter-to-QoI mapping, then the MC estimator $v_j^{(N_{MC})}(g)$ will have a small variance for a modest choice of N_{MC} . In such cases the MC sample size for estimating $v_j(g)$ does not need to be very large.

Functional DGSMs. Next, we turn to DGSMs for functional QoIs. We propose the following definition for a functional DGSM

$$\mathfrak{N}_j(f; \mathcal{X}) = \int_{\mathcal{X}} \int_{\Theta} \left(\frac{\partial f}{\partial \theta_j}(s, \boldsymbol{\theta}) \right)^2 \mu(d\boldsymbol{\theta}) ds = \int_{\mathcal{X}} v_j(f(s, \cdot)) ds, \quad (4.10)$$

which is a natural choice. These indices can be normalized in different ways to make their comparison easier. For instance, we may consider the normalized indices

$$\frac{\mathfrak{N}_j(f; \mathcal{X})}{\sum_{k=1}^{N_p} \mathfrak{N}_k(f; \mathcal{X})}, \quad j = 1, \dots, N_p.$$

We can relate $\mathfrak{N}_j(f; \mathcal{X})$ to the corresponding functional total Sobol' indices $\mathfrak{S}_j^{\text{tot}}(f; \mathcal{X})$, $j = 1, \dots, N_p$, analogously to the scalar case. Specifically, we present the following result that shows functional total Sobol' indices can be bounded in terms of the proposed functional DGSMs.

Theorem 4.3.1. *Let $f(s, \boldsymbol{\theta})$ be a random process satisfying Assumption 4.2.1. Suppose θ_j are independent and distributed according to uniform or normal distribution, for $i = 1, \dots, N_p$. Then,*

$$\mathfrak{S}_j^{\text{tot}}(f; \mathcal{X}) \leq c_j^p \frac{\mathfrak{N}_j(f; \mathcal{X})}{\text{Tr}(\mathcal{C}_{qoi})}, \quad j = 1, \dots, N_p, \quad (4.11)$$

where \mathcal{C}_{qoi} is the covariance operator of the random function $f(s, \boldsymbol{\theta})$, and

$$c_j^p = \begin{cases} (b - a)^2 / \pi^2, & \text{if } \theta_j \sim U(a, b), \\ \sigma_j^2, & \text{if } \theta_j \sim \mathcal{N}(0, \sigma_j^2). \end{cases}$$

Proof. For a fixed $s \in \mathcal{X}$, by the results in [59],

$$S_j^{\text{tot}}(f; s) \leq \frac{c_j^p}{D(f; s)} v_j(f; s). \quad (4.12)$$

Then, using (4.3),

$$\begin{aligned}\mathfrak{S}_j^{\text{tot}}(f; \mathcal{X}) &= \int_{\mathcal{X}} S_j^{\text{tot}}(f; s) w(s) ds \\ &\leq \int_{\mathcal{X}} \frac{c_j^p}{D(f; s)} v_j(f; s) w(s) ds = c_j^p \frac{\mathfrak{N}_j(f; \mathcal{X})}{\int_{\mathcal{X}} D(f; s) ds}.\end{aligned}\tag{4.13}$$

Now, let \mathcal{C}_{qoi} be the covariance operator of the random process $f(s, \boldsymbol{\theta})$, and let $c(s, t)$ be its covariance function. As a consequence of Mercer's Theorem [62, 71], we have

$$\int_{\mathcal{X}} D(f; s) ds = \int_{\mathcal{X}} \text{Var}\{f(s, \cdot)\} ds = \int_{\mathcal{X}} c(s, s) ds = \text{Tr}(\mathcal{C}_{\text{qoi}}).$$

Combining this with (4.13) we obtain the desired result. \blacksquare

The DGSM-based upper bounds on the functional total Sobol' indices provided by Theorem 4.3.1 enable identifying inputs with small total Sobol' indices, hence providing an efficient way of identifying unimportant parameters. Note that the theorem is stated for θ_j that are distributed uniformly or normally, because these distributions are commonly used in modeling under uncertainty. However, the result holds for other families of distributions. Specifically, in [60], it is shown that (4.12) holds for the Boltzmann family of distributions with appropriate choices of the constants c_j^p , $j = 1, \dots, N_p$, which provides immediate extension of Theorem 4.3.1 to Boltzmann family of distributions. We mention that an important class of Boltzmann distributions is the family of log-concave distributions that includes Normal, Exponential, Beta, Gamma, Gumbel, and Weibull distributions [60].

Similar to the case of scalar QoIs, estimating functional DGSM often requires fewer samples than are required for direct calculation of the Sobol' indices via MC Sampling. The following result, which is similar to Proposition 4.3.1, provides a bound on the variance of the corresponding MC estimator, given appropriate boundedness assumptions on the partial derivatives of the functional QoI.

Proposition 4.3.2. *Assume that there exist non-negative integrable functions a_j and b_j , defined on \mathcal{X} such that for each $s \in \mathcal{X}$,*

$$a_j(s) \leq \left(\frac{\partial f(s, \boldsymbol{\theta})}{\partial \theta_j} \right)^2 \leq b_j(s), \quad j = 1, \dots, N_p, \quad \text{for all } \boldsymbol{\theta} \in \Theta.$$

Consider the MC estimator

$$\mathfrak{N}_j^{(N_{\text{MC}})}(f; \mathcal{X}) := \frac{1}{N_{\text{MC}}} \sum_{k=1}^{N_{\text{MC}}} \int_{\mathcal{X}} \left(\frac{\partial f}{\partial \theta_j}(s, \boldsymbol{\theta}^k) \right)^2 ds,$$

with $\boldsymbol{\theta}^k$ independent and identically distributed according to the law of $\boldsymbol{\theta}$. Then,

$$\text{Var} \left\{ \mathfrak{N}_j^{(N_{MC})}(f; \mathcal{X}) \right\} \leq \frac{1}{4N_{MC}} \|b_j - a_j\|_{L^1(\mathcal{X})}^2, \quad j = 1, \dots, N_p.$$

Proof. First note that $\mathfrak{N}_j^{(N_s)}(f; \mathcal{X})$ is indeed an estimator for $\mathfrak{N}_j(f; \mathcal{X})$. This is seen by noting that, using Tonelli's Theorem,

$$\mathfrak{N}_j(f; \mathcal{X}) = \int_{\mathcal{X}} v_j(f; s) ds = \int_{\mathcal{X}} \int_{\Theta} \left(\frac{\partial f}{\partial \theta_j}(s, \boldsymbol{\theta}) \right)^2 \mu(d\boldsymbol{\theta}) ds = \int_{\Theta} \int_{\mathcal{X}} \left(\frac{\partial f}{\partial \theta_j}(s, \boldsymbol{\theta}) \right)^2 ds \mu(d\boldsymbol{\theta}).$$

Then, applying Popoviciu's inequality to the random variable $G_j(\boldsymbol{\theta}) = \int_{\mathcal{X}} \left(\frac{\partial f}{\partial \theta_j}(s, \boldsymbol{\theta}) \right)^2 ds$, which satisfies $\|a_j\|_{L^1(\mathcal{X})} \leq G_j \leq \|b_j\|_{L^1(\mathcal{X})}$, gives:

$$\text{Var} \{G_j\} \leq \frac{1}{4} \left(\|b_j\|_{L^1(\mathcal{X})} - \|a_j\|_{L^1(\mathcal{X})} \right)^2 \leq \frac{1}{4} \|b_j - a_j\|_{L^1(\mathcal{X})}^2, \quad j = 1, \dots, N_p,$$

where we also used the reverse triangle inequality. This completes the proof. \blacksquare

The indices \mathfrak{N}_j can be computed by sampling the partial derivatives. Gradient computation can be performed using various techniques. The simplest approach is to use the finite difference method. However, this approach becomes prohibitive for computationally intensive models with a large number of input parameters. For models governed by differential equations, one can use the so called *sensitivity equations* for computing derivatives. We demonstrate this in one of our numerical examples in 4.5. Unfortunately, this approach also suffers from the curse of dimensionality, and becomes cumbersome for complex systems. Another approach, not explored in the present work, is that of automatic differentiation. The challenges of gradient computation are compounded for models governed by expensive-to-solve PDEs with high-dimensional input parameters. For such models, we propose an approach that combines low-rank KLEs and adjoint-based gradient computation.

With the strategy of using low-rank KLEs for the purposes of computing DGSMs in mind, we examine functional QoIs of the form

$$f(s, \boldsymbol{\theta}) = \sum_{i=1}^{N_{qoi}} \gamma_i f_i(\boldsymbol{\theta}) \phi_i(s), \quad (4.14)$$

where ϕ_i are orthonormal with respect to $L^2(\mathcal{X})$ inner product, $\{\gamma_i\}$ are non-negative and sorted in descending order, $E\{f_i\} = 0$, $i = 1, \dots, N_{qoi}$, and $E\{f_i f_j\} = \delta_{ij}$. Suppose also that f_i have square integrable partial derivatives.

Theorem 4.3.2. *Let f be a random process of the form (4.14). Suppose θ_j are independent and distributed according to uniform or normal distribution for $j = 1, \dots, N_p$. Then the following hold:*

1. $\mathfrak{N}_j(f; \mathcal{X}) = \sum_{i=1}^{N_{qoi}} \gamma_i^2 v_j(f_i)$, $j = 1, \dots, N_p$.

2. We have the bound

$$\mathfrak{S}_j^{\text{tot}}(f; \mathcal{X}) \leq c_j^p \frac{\mathfrak{N}_j(f; \mathcal{X})}{\sum_{i=1}^{N_{\text{qoi}}} \gamma_i^2} = c_j^p \frac{\sum_{i=1}^{N_{\text{qoi}}} \gamma_i^2 \nu_j(f_i)}{\sum_{i=1}^{N_{\text{qoi}}} \gamma_i^2}, \quad j = 1, \dots, N_p,$$

where,

$$c_j^p = \begin{cases} (b-a)^2/\pi^2, & \text{if } \theta_j \sim U(a, b), \\ \sigma_j^2, & \text{if } \theta_j \sim \mathcal{N}(0, \sigma_j^2). \end{cases}$$

Proof. First, we note

$$\begin{aligned} \nu_j(f(s, \cdot)) &= \int_{\Theta} \left(\frac{\partial}{\partial \theta_j} \sum_{i=1}^{N_{\text{qoi}}} \gamma_i f_i(\boldsymbol{\theta}) \phi_i(s) \right)^2 \mu(d\boldsymbol{\theta}) = \int_{\Theta} \left(\sum_{i=1}^{N_{\text{qoi}}} \gamma_i \frac{\partial f_i(\boldsymbol{\theta})}{\partial \theta_j} \phi_i(s) \right)^2 \mu(d\boldsymbol{\theta}) \\ &= \sum_{i,k=1}^{N_{\text{qoi}}} \gamma_i \gamma_k \left(\int_{\Theta} \frac{\partial f_i(\boldsymbol{\theta})}{\partial \theta_j} \frac{\partial f_k(\boldsymbol{\theta})}{\partial \theta_j} \mu(d\boldsymbol{\theta}) \right) \phi_i(s) \phi_k(s). \end{aligned}$$

Therefore,

$$\begin{aligned} \mathfrak{N}_j(f; \mathcal{X}) &= \int_{\mathcal{X}} \nu_j(f(s, \cdot)) ds \\ &= \int_{\mathcal{X}} \left(\sum_{i,k=1}^{N_{\text{qoi}}} \gamma_i \gamma_k \int_{\Theta} \frac{\partial f_i(\boldsymbol{\theta})}{\partial \theta_j} \frac{\partial f_k(\boldsymbol{\theta})}{\partial \theta_j} \mu(d\boldsymbol{\theta}) \phi_i(s) \phi_k(s) \right) ds \\ &= \sum_{i,k=1}^{N_{\text{qoi}}} \gamma_i \gamma_k \left(\int_{\Theta} \frac{\partial f_i(\boldsymbol{\theta})}{\partial \theta_j} \frac{\partial f_k(\boldsymbol{\theta})}{\partial \theta_j} \mu(d\boldsymbol{\theta}) \right) \int_{\mathcal{X}} \phi_i(s) \phi_k(s) ds \\ &= \sum_{i=1}^{N_{\text{qoi}}} \gamma_i^2 \left[\int_{\Theta} \left(\frac{\partial f_i(\boldsymbol{\theta})}{\partial \theta_j} \right)^2 \mu(d\boldsymbol{\theta}) \right] = \sum_{i=1}^{N_{\text{qoi}}} \gamma_i^2 \nu_j(f_i). \end{aligned}$$

This establishes the first assertion of the theorem. Next, letting \mathcal{C}_{qoi} be the covariance operator of $f(s, \boldsymbol{\theta})$, it is straightforward to see that $\text{Tr}(\mathcal{C}_{\text{qoi}}) = \sum_{i=1}^{N_{\text{qoi}}} \gamma_i^2$. Thus, combining the first assertion of the theorem with Theorem 4.3.1, we have

$$\mathfrak{S}_j^{\text{tot}}(f; \mathcal{X}) \leq c_j^p \frac{\mathfrak{N}_j(f; \mathcal{X})}{\sum_{i=1}^{N_{\text{qoi}}} \gamma_i^2} = c_j^p \frac{\sum_{i=1}^{N_{\text{qoi}}} \gamma_i^2 \nu_j(f_i)}{\sum_{i=1}^{N_{\text{qoi}}} \gamma_i^2}, \quad j = 1, \dots, N_p.$$

■

Computing DGSMs for functional outputs. To enable efficient computation of functional DGSMs, we use a truncated KLE of f . Let $(\lambda_i(\mathcal{C}_{\text{qoi}}), \phi_i)$ be the eigenpairs of the covariance operator of f ; we consider the truncated KLE

$$f(s, \boldsymbol{\theta}) \approx \hat{f}(s, \boldsymbol{\theta}) := \bar{f}(s) + \sum_{i=1}^{N_{\text{qoi}}} \sigma_i f_i(\boldsymbol{\theta}) \phi_i(s), \quad \text{with } \sigma_i = \sqrt{\lambda_i(\mathcal{C}_{\text{qoi}})}, \quad (4.15)$$

where \bar{f} is the mean of the process and the KL modes f_i are given by

$$f_i(\boldsymbol{\theta}) = \frac{1}{\sigma_i} \int_{\mathcal{X}} (f(s, \boldsymbol{\theta}) - \bar{f}(s)) \phi_i(s) ds, \quad i = 1, \dots, N_{\text{qoi}}. \quad (4.16)$$

In many applications of interest, where the process f is defined in terms of the solution of a differential equation, the eigenvalues $\lambda_i(\mathcal{C}_{\text{qoi}})$ decay rapidly, and thus a small N_{qoi} can be afforded. Such processes, which we refer to as low-rank, are common in physical and biological applications. Computing the KLE numerically can be accomplished e.g., using Nyström's method, which is the approach taken in the numerical experiments in the present work. We refer to [7], for a convenient reference for numerical computation of KLEs using Nyström's method. We point out that this process requires approximating the covariance function of f , through sampling, when solving the eigenvalue problem for $\{\lambda_i(\mathcal{C}_{\text{qoi}})\}_{i \geq 1}$ and the corresponding eigenvectors $\{\phi_i\}_{i \geq 1}$. This computation requires an ensemble of model evaluations $\{f(\cdot, \boldsymbol{\theta}^k)\}_{k=1}^{N_{\text{MC}}}$. Typically a modest sample size N_{MC} is sufficient for computing the dominant eigenpairs of \mathcal{C}_{qoi} . This is demonstrated in our numerical results in 4.5.

The approximate model \hat{f} can then be used as a surrogate for f for the purposes of sensitivity analysis. Specifically we compute the functional DGSMs of \hat{f} as a proxy for those of f . The computation of functional DGSMs for \hat{f} and the DGSM-based bound on functional Sobol' indices is facilitated by Theorem 4.3.2.

The expression for the functional DGSM given in 4.3.2 requires computing DGSMs for the KL modes f_i , $i = 1, \dots, N_{\text{qoi}}$, which are scalar-valued random variables. Differentiability of f_i can be established by requiring certain boundedness assumptions on the partial derivatives. We consider a generic KL mode, which we denote by

$$F(\boldsymbol{\theta}) := \int_{\mathcal{X}} (f(s, \boldsymbol{\theta}) - \bar{f}(s)) v(s) ds, \quad (4.17)$$

where we use a generic $v \in L^2(\mathcal{X})$ in the place of the eigenvectors.

Proposition 4.3.3. *Let f be a process satisfying 4.2.1, and moreover assume partial derivatives of f with respect to θ_j , $j = 1, \dots, N_p$ satisfy*

$$\left| \frac{\partial f}{\partial \theta_j}(s, \boldsymbol{\theta}) \right| \leq z_j(s), \quad \text{for all } (s, \boldsymbol{\theta}) \in \mathcal{X} \times \Theta, \quad (4.18)$$

where $z_j \in L^2(\mathcal{X})$, $j = 1, \dots, N_p$. Let F be as in (4.17). Then, for $j = 1, \dots, N_p$,

1. $\frac{\partial F}{\partial \theta_j}(\boldsymbol{\theta}) = \int_{\mathcal{X}} \frac{\partial f}{\partial \theta_j}(s, \boldsymbol{\theta}) v(s) ds,$
2. and $\frac{\partial F}{\partial \theta_j} \in L^2(\Theta).$

Proof. Showing (a) amounts to establishing the standard requirements for differentiating under the integral sign; see e.g. see Theorem 2.27 in [39]. Without loss of generality, we assume

$\bar{f} \equiv 0$. First, we note that for each $\boldsymbol{\theta} \in \Theta$,

$$\int_{\mathcal{X}} \left| \frac{\partial f}{\partial \theta_j}(s, \boldsymbol{\theta}) v(s) \right| ds \leq \left[\int_{\mathcal{X}} \left(\frac{\partial f}{\partial \theta_j}(s, \boldsymbol{\theta}) \right)^2 ds \right]^{1/2} \left[\int_{\mathcal{X}} v(s)^2 ds \right]^{1/2} < \infty, \quad j = 1, \dots, N_p,$$

where we used the Cauchy–Schwarz inequality and 4.2.1(b),(c). Next, we note that $|\frac{\partial f}{\partial \theta_j}(s, \cdot) v(\cdot)| \leq z_j |v|$ and applying the Cauchy–Schwarz inequality, we get that $\int_{\mathcal{X}} |z_j(s) v(s)| ds < \infty$. Thus, assertion (a) follows from Theorem 2.27 in [39]. The assertion (b) of the proposition follows from, 4.2.1(c) and

$$\begin{aligned} \int_{\Theta} \left(\frac{\partial F}{\partial \theta_j}(\boldsymbol{\theta}) \right)^2 \mu(d\boldsymbol{\theta}) &= \int_{\Theta} \left(\int_{\mathcal{X}} \frac{\partial f}{\partial \theta_j}(s, \boldsymbol{\theta}) v(s) ds \right)^2 \mu(d\boldsymbol{\theta}) \\ &\leq \int_{\Theta} \left[\int_{\mathcal{X}} \left(\frac{\partial f}{\partial \theta_j}(s, \boldsymbol{\theta}) \right)^2 ds \right] \left[\int_{\mathcal{X}} v(s)^2 ds \right] \mu(d\boldsymbol{\theta}) = \|v\|_{L^2(\mathcal{X})}^2 \left\| \frac{\partial f}{\partial \theta_j} \right\|_{L^2(\mathcal{X} \times \Theta)}^2 < \infty \end{aligned}$$

■

Note that the assumption (4.18) can in fact be used to conclude $\frac{\partial F}{\partial \theta_j} \in L^\infty(\Theta)$; we showed square integrability of these partial derivatives for clarity as this is the result needed for the purposes of derivative-based GSA. Note also that the assumption (4.18) can be relaxed in the statement of the proposition by requiring local (in Θ) boundedness of the partial derivatives by square integrable (in \mathcal{X}) functions.

The above framework, based on low-rank KLEs, is useful as it provides a natural setting for deploying an adjoint-based approach for computing the derivatives of the KL modes, in models governed by PDEs (or ODEs). The computational advantage of adjoint-based approach is immense: the cost of computing the gradient of f_i 's does not scale with the dimension of the input parameter $\boldsymbol{\theta}$. This leads to a computationally efficient and scalable framework for computing DGSMs. We detail this approach in the next section for models governed by elliptic PDEs and demonstrate its effectiveness in numerical examples in 4.5.

4.4 Adjoint-based GSA for models governed by elliptic PDEs

We consider a linear elliptic PDE with a random coefficient function:

$$\begin{aligned} -\nabla \cdot (\kappa \nabla p) &= b \quad \text{in } \mathcal{D}, \\ p &= g \quad \text{on } \Gamma_D, \\ \kappa \nabla p \cdot n &= h \quad \text{on } \Gamma_N. \end{aligned} \tag{4.19}$$

The coefficient field κ is modeled as a log-Gaussian random field whose covariance operator is given by \mathcal{C}_{par} . As is common practice in the uncertainty quantification community, we

represent the random field coefficient κ using a truncated KLE. Namely, let

$$\hat{a}(x, \boldsymbol{\theta}) = \bar{a}(x) + \sum_{j=1}^{N_p} \sqrt{\lambda_j(\mathcal{C}_{\text{par}})} \theta_j e_j(x)$$

be a truncated KLE of the log-permeability field, $a(x, \boldsymbol{\theta}) = \log \kappa(x, \boldsymbol{\theta})$. We consider the weak form of the PDE. The associated trial and test function spaces are, respectively,

$$\mathcal{V}_g = \{v \in H^1(\mathcal{D}) : v|_{\Gamma_D} = g\}, \quad \mathcal{V}_0 = \{v \in H^1(\mathcal{D}) : v|_{\Gamma_D} = 0\}.$$

The weak form of (4.19) is as follows: find $p \in \mathcal{V}_g$ such that

$$\langle e^{\hat{a}(x, \boldsymbol{\theta})} \nabla p, \nabla \tilde{p} \rangle = \langle b, \tilde{p} \rangle + \langle h, \tilde{p} \rangle_{\Gamma_N}, \quad \text{for all } \tilde{p} \in \mathcal{V}_0, \quad (4.20)$$

where $\langle \cdot, \cdot \rangle$ is the $L^2(\mathcal{D})$ inner product, and $\langle \cdot, \cdot \rangle_{\Gamma_N}$ is $L^2(\Gamma_N)$ inner product. Let \mathcal{X} a closed subset of \mathcal{D} , and let $\mathcal{Q} : L^2(\mathcal{D}) \rightarrow L^2(\mathcal{X})$ be the restriction operator

$$\mathcal{Q}u = u|_{\mathcal{X}}.$$

Below we also need the adjoint \mathcal{Q}^* of \mathcal{Q} : it is straightforward to see that $\mathcal{Q}^* : L^2(\mathcal{X}) \rightarrow L^2(\mathcal{D})$ is given by

$$(\mathcal{Q}^*u)(x) = \begin{cases} u(x), & x \in \mathcal{X} \\ 0, & x \notin \mathcal{X}. \end{cases}$$

We consider the QoI,

$$f(x, \boldsymbol{\theta}) = \mathcal{Q}p(x, \boldsymbol{\theta}),$$

and consider its truncated KLE

$$f(x, \boldsymbol{\theta}) \approx \hat{f}(x, \boldsymbol{\theta}) := \bar{f}(x) + \sum_{i=1}^{N_{\text{qoi}}} \sigma_i f_i(\boldsymbol{\theta}) \phi_i(x), \quad \text{with } \sigma_i = \sqrt{\lambda_i(\mathcal{C}_{\text{qoi}})}. \quad (4.21)$$

where

$$f_i(\boldsymbol{\theta}) = \frac{1}{\sigma_i} \int_{\mathcal{X}} (f(x, \boldsymbol{\theta}) - \bar{f}(x)) \phi_i(x) dx = \frac{1}{\sigma_i} \int_{\mathcal{X}} (\mathcal{Q}p(x, \boldsymbol{\theta}) - \bar{f}(x)) \phi_i(x) dx,$$

where p is the solution of (4.20). We consider adjoint-based computation of $\frac{\partial f_i}{\partial \theta_j}$ for $i, j \in \{1, \dots, N_{\text{qoi}}\} \times \{1, \dots, N_p\}$.

Computing gradient of f_i 's. To compute the gradient we follow a formal Lagrange approach. We consider the Lagrangian

$$\mathcal{L}(p, \boldsymbol{\theta}, q) = \frac{1}{\sigma_i} \int_{\mathcal{X}} (\mathcal{Q}p - \bar{f}) \phi_i dx + \langle e^{\hat{a}(x, \boldsymbol{\theta})} \nabla p, \nabla q \rangle - \langle b, q \rangle - \langle h, q \rangle_{\Gamma_N}.$$

Here q is a Lagrange multiplier, which in the present context is referred to as the adjoint variable. Taking variational derivatives of \mathcal{L} with respect to q , and p , give the state and the adjoint equations, respectively. In particular, the adjoint equation is found by considering

$$\frac{d}{d\epsilon} \mathcal{L}(p + \epsilon \tilde{p}, \boldsymbol{\theta}, q) |_{\epsilon=0} = 0, \quad \text{for all } \tilde{p} \in \mathcal{V}_0.$$

This gives,

$$\frac{1}{\sigma_i} \langle \mathcal{Q} \tilde{p}, \phi_i \rangle_{\mathcal{X}} + \langle e^{\hat{a}(x, \boldsymbol{\theta})} \nabla \tilde{p}, \nabla q \rangle = 0, \quad \text{for all } \tilde{p} \in \mathcal{V}_0.$$

The weak form of the adjoint equation can be stated as: find $q \in \mathcal{V}_0$ such that

$$\langle e^{\hat{a}(x, \boldsymbol{\theta})} \nabla q, \nabla \tilde{p} \rangle = -\frac{1}{\sigma_i} \langle \mathcal{Q}^* \phi_i, \tilde{p} \rangle, \quad \text{for all } \tilde{p} \in \mathcal{V}_0.$$

The strong form of the adjoint equation is

$$\begin{aligned} -\nabla \cdot (\kappa \nabla q) &= -\frac{1}{\sigma_i} \mathcal{Q}^* \phi_i \quad \text{in } \mathcal{D}, \\ q &= 0 \quad \text{on } \Gamma_D, \\ \kappa \nabla q \cdot n &= 0 \quad \text{on } \Gamma_N. \end{aligned} \tag{4.22}$$

Letting p and q be the solutions of the state and adjoint equations respectively,

$$(\nabla_{\boldsymbol{\theta}} f_i)^T \tilde{\boldsymbol{\theta}} = \frac{d}{d\epsilon} \mathcal{L}(p, \boldsymbol{\theta} + \epsilon \tilde{\boldsymbol{\theta}}, q) |_{\epsilon=0} = \langle (\hat{a}(x, \tilde{\boldsymbol{\theta}}) - \bar{a}(x)) e^{\hat{a}(x, \boldsymbol{\theta})} \nabla p, \nabla q \rangle, \quad \tilde{\boldsymbol{\theta}} \in \mathbb{R}^{N_p}. \tag{4.23}$$

In particular, letting $\tilde{\boldsymbol{\theta}}$ be the j th coordinate direction in \mathbb{R}^{N_p} , we get

$$\frac{\partial f_i}{\partial \theta_j} = \sqrt{\lambda_j(C_{\text{par}})} \langle e_j e^{\hat{a}(x, \boldsymbol{\theta})} \nabla p, \nabla q \rangle.$$

We can also consider a QoI of the form

$$f(\cdot, \boldsymbol{\theta}) = p(\cdot, \boldsymbol{\theta})|_{\Gamma_N},$$

as done in one of our numerical examples in section 4.5. Computing the gradient for this QoI can be done in a similar way as above, except, in this case the adjoint equation takes the form:

$$\begin{aligned} -\nabla \cdot (\kappa \nabla q) &= 0 \quad \text{in } \mathcal{D}, \\ q &= 0 \quad \text{on } \Gamma_D, \\ \kappa \nabla q \cdot n &= -\frac{1}{\sigma_i} \phi_i \quad \text{on } \Gamma_N. \end{aligned} \tag{4.24}$$

Notice that evaluating the adjoint-based expression for the gradient of f_i , requires two PDE solves: we need to solve the state (forward) equation (4.19) and the adjoint equation (4.22)

Moreover the forward solves can be reused across the KL modes, and thus, computing the gradient of \hat{f} in (4.21) requires $1 + N_{\text{qoi}}$ PDE solves, independently of the dimension N_p of the uncertain parameter $\boldsymbol{\theta}$. As shown in our numerical examples, a small N_{qoi} often results in suitable representations of the QoI f , due to the, often observed, rapid decay of the eigenvalues $\lambda_i(\mathcal{C}_{\text{qoi}})$.

DGSM computation. In practice, the KLE should be computed numerically. As mentioned before, this can be accomplished using Nyström's method, which is the approach taken in the present work, and requires an ensemble of model evaluations $\{f(\cdot, \boldsymbol{\theta}^k)\}_{k=1}^{N_{\text{MC}}}$, typically with a modest sample size N_{MC} . The model evaluations can be used to compute the approximate KLE following Algorithm 1 in [7]. This same set of samples can be used for computing the DGSMs, $v_j(f_i)$, $j = 1, \dots, N_p$, $i = 1, \dots, N_{\text{qoi}}$. These require an additional adjoint solve per KL mode, and for each sample point $\boldsymbol{\theta}^k$, $k = 1, \dots, N_{\text{MC}}$. Thus, the overall computational cost is $N_{\text{MC}}(1 + N_{\text{qoi}})$ PDE solves. Note that the computational cost, in terms of PDE solves, is independent of the dimension N_p of the uncertain parameter vector. To compute the DGSM-based bound on functional Sobol' indices we also need to compute $\text{Tr}(\mathcal{C}_{\text{qoi}})$; this can be approximated accurately by summing the dominant eigenvalues of \mathcal{C}_{qoi} , available from computing the KLE of f . The steps for DGSM computation using the present strategy are outlined in Algorithm 2. In step 5 of Algorithm 2, **getKLE** indicates a procedure that given

Algorithm 2 Algorithm for computing $\mathfrak{B}_j := \mathfrak{N}_j(f; \mathcal{X}) / \text{Tr}(\mathcal{C}_{\text{qoi}})$, $j = 1, \dots, N_p$.

Input: Parameter samples $\{\boldsymbol{\theta}^k\}_{k=1}^{N_{\text{MC}}}$

Output: Approximate DGSM-based bounds $\hat{\mathfrak{B}}_j$, $j = 1, \dots, N_p$

```

1: for  $k = 1, \dots, N_{\text{MC}}$  do
2:   solve forward model (4.19) with  $\kappa = \exp \hat{a}(\cdot, \boldsymbol{\theta}^k)$ 
3:   compute QoI  $f(\cdot, \boldsymbol{\theta}^k)$ 
4: end for
5:  $[\{\lambda_i\}_{i=1}^{N_{\text{qoi}}}, \{\phi_i\}_{i=1}^{N_{\text{qoi}}}] = \text{getKLE}(\{f(\cdot, \boldsymbol{\theta}^k)\}_{k=1}^{N_{\text{MC}}})$ 
6: for  $k = 1, \dots, N_{\text{MC}}$  do
7:   for  $i = 1, \dots, N_{\text{qoi}}$  do
8:     solve adjoint problem (4.22) with  $\kappa = \exp \hat{a}(\cdot, \boldsymbol{\theta}^k)$ 
9:     compute  $\frac{\partial f_i(\boldsymbol{\theta}^k)}{\partial \theta_j}$ ,  $j = 1, \dots, N_p$  using ((4.23))
10:   end for
11: end for
12: compute  $\hat{v}_j(f_i) = \frac{1}{N_{\text{MC}}} \sum_{k=1}^{N_{\text{MC}}} \left[ \frac{\partial f_i(\boldsymbol{\theta}^k)}{\partial \theta_j} \right]^2$ 
13: compute  $T = \sum_{i=1}^{N_{\text{qoi}}} \lambda_i$ 
14: compute  $\hat{\mathfrak{B}}_j = \sum_{i=1}^{N_{\text{qoi}}} \lambda_i \hat{v}_j(f_i) / T$ ,  $j = 1, \dots, N_p$ 

```

sample realizations of the process f , computes its KLE numerically. As mentioned before,

this can be done, e.g., using Nyström's method; see e.g., Algorithm 1 in [7] or section 2.3 in chapter 2.

4.5 Numerical examples

In this section, we present three numerical examples. In section 4.5.1, we consider an example involving a nonlinear ODE system with a time-dependent QoI, which is used to illustrate functional DGSMs and the DGSM-based bound derived in Theorem 4.3.1. sections 4.5.2 and 4.5.3 concern models governed by elliptic PDEs that have spatially distributed QoIs in one and two space dimensions, respectively. For the PDE-based examples we implement the adjoint-based GSA framework described in section 4.4 and illustrate its effectiveness.

4.5.1 Sensitivity analysis for a model of cholera epidemics

Consider the cholera model developed in [51]. We analyze the sensitivity of the infected population as a function of time to uncertainties in model parameters. This problem was also studied in [6] within the context of variance-based GSA for time-dependent processes.

4.5.1.1 Model description

A population of N_{pop} individuals is split into susceptible, infectious, and recovered individuals, which are denoted by S , I , and R , respectively. The concentrations of highly-infectious bacteria, B_H and lowly-infectious bacteria, B_L are also considered. These concentrations are measured in cells per milliliter. According to the model developed in [51], the time-evolution of the state variables is governed by the following system of ODEs.

$$\begin{aligned}
\frac{dS}{dt} &= bN_{\text{pop}} - \beta_L S \frac{B_L}{\kappa_L + B_L} - \beta_H S \frac{B_H}{\kappa_H + B_H} - bS \\
\frac{dI}{dt} &= \beta_L S \frac{B_L}{\kappa_L + B_L} + \beta_H S \frac{B_H}{\kappa_H + B_H} - (\gamma + b)I \\
\frac{dR}{dt} &= \gamma I - bR \\
\frac{dB_H}{dt} &= \xi I - \chi B_H \\
\frac{dB_L}{dt} &= \chi B_H - \delta B_L
\end{aligned} \tag{4.25}$$

with initial conditions $(S(0), I(0), R(0), B_H(0), B_L(0)) = (S_0, I_0, R_0, B_{H_0}, B_{L_0})$. The parameter units and nominal values from [51] are compiled in Table 4.1. We consider a total population of $N_{\text{pop}} = 10,000$ and let the initial states be as follows: $S_0 = N_{\text{pop}} - 1$, $I_0 = 1$, $R_0 = 0$, and $B_{H_0} = B_{L_0} = 0$. We solve the problem up to time $T = 150$ using the `ode45` solver provided in MATLAB [70].

Table 4.1 Cholera model parameters from [6, 51].

Model Parameter	Symbol	Units	Values
Rate of drinking B_L cholera	β_L	$\frac{1}{\text{week}}$	1.5
Rate of drinking B_H cholera	β_H	$\frac{1}{\text{week}}$	7.5
B_L cholera carrying capacity	κ_L	$\frac{\# \text{ bacteria}}{\text{ml}}$	10^6
B_H cholera carrying capacity	κ_H	$\frac{\# \text{ bacteria}}{\text{ml}}$	$\frac{\kappa_L}{700}$
Human birth and death rate	b	$\frac{1}{\text{week}}$	$\frac{1}{1560}$
Rate of decay from B_H to B_L	χ	$\frac{1}{\text{week}}$	$\frac{168}{5}$
Rate at which infectious individuals spread B_H bacteria to water	ζ	$\frac{\# \text{ bacteria}}{\# \text{ individuals} \cdot \text{ml} \cdot \text{week}}$	70
Death rate of B_L cholera	δ	$\frac{1}{\text{week}}$	$\frac{7}{30}$
Rate of recovery from cholera	γ	$\frac{1}{\text{week}}$	$\frac{7}{5}$

To simplify the notation we use a generic vector $y \in \mathbb{R}^5$ to denote the state vector $y = (y_1, y_2, y_3, y_4, y_5)^\top = (S, I, R, B_H, B_L)^\top$ and denote the right hand side of the ODE system by $g(y; c)$, where $c = (\beta_L, \beta_H, \kappa_L, b, \chi, \zeta, \delta, \gamma)$ is the vector of uncertain model parameters. The uncertainties in ic are parameterized by a random vector $\theta \in \mathbb{R}^8$ with iid $U(-1, 1)$ entries as follows:

$$c_i(\theta_i) = \frac{1}{2}(a_i + b_i) + \frac{1}{2}(b_i - a_i)\theta_i, \quad i = 1, \dots, 8,$$

with $[a_i, b_i]$ the physical parameter ranges for c_i , adapted from [6]. The solution of the system is a random process, $y = y(t; \theta)$. We focus on the infected population $I(t, \theta) = y_2(t; \theta)$, for $t \in [0, 150]$. In Figure 4.1, we depict the time evolution of $I(t, \theta)$ at the nominal parameter vector given by $\theta = (0, 0, \dots, 0)^\top \in \mathbb{R}^8$.

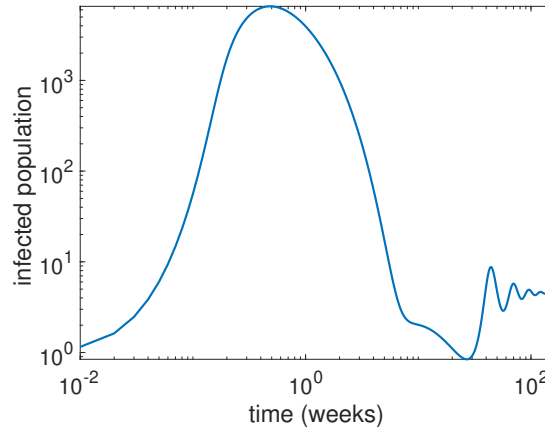


Figure 4.1 The infected population $I(t; \theta)$ with $\theta = 0$.

4.5.1.2 Derivative-based GSA

To compute the partial derivatives $\mathbf{s}_j(t; \boldsymbol{\theta}) = \frac{\partial \mathbf{y}(t; \boldsymbol{\theta})}{\partial \theta_j}$, $j = 1, \dots, 8$, needed for DGSM computation, we rely on the so called direct approach; this involves integrating the sensitivity equations [68, 93] along with the ODEs describing the system state. Specifically, we need to integrate the system

$$\begin{aligned} \mathbf{y}' &= \mathbf{g}(\mathbf{y}; \mathbf{c}(\boldsymbol{\theta})), \quad \mathbf{y}(0) = \mathbf{y}_0, \\ \mathbf{s}'_i &= \mathbf{J} \mathbf{s}_i + \frac{\partial \mathbf{g}}{\partial \theta_i}, \quad \mathbf{s}_i(0) = \mathbf{0}, \quad i = 1, \dots, N_p. \end{aligned}$$

Here \mathbf{J} is the Jacobian $J_{ij} = \frac{\partial g_i}{\partial \theta_j} = \frac{\partial g_i}{\partial c_j} \frac{\partial c_j}{\partial \theta_j}$, $i, j = 1, \dots, N_p$. In the present example this results in an “augmented state vector” $[\mathbf{y}^T \mathbf{s}_1^T \dots \mathbf{s}_8^T]^T \in \mathbb{R}^{45}$.

First, we consider the pointwise-in-time DGSMs, $v_j(f(t, \cdot))$, $j = 1, \dots, 8$, for $t \in [0, 150]$ in Figure 4.2 (left). To ensure an accurate estimate of the DGSMs, we approximate the integral over the parameters with a Monte Carlo sample of size 10^5 . As seen in Figure 4.2 (left), these pointwise-in-time DGSMs are not straightforward to interpret. A clearer picture is obtained by considering

$$\Re_j(I; [0, t]) := \int_0^t v_j(I(s, \cdot)) ds, \quad t \in [0, 150],$$

which amounts to computing the functional DGSMs over successively larger time intervals; the results are reported in Figure 4.2 (right).

Finally, to get an overall picture, we compute the DGSM-based upper bounds on the functional Sobol’ indices, as given by Theorem 4.3.1, with $\mathcal{X} = [0, 150]$; see Figure 4.3, where we report the functional total Sobol’ indices along with the DGSM-based bounds which are computed with Monte Carlo (MC) sample sizes of 10^5 and 100. Note that a small MC sample is very effective in detecting the unimportant parameters.

By Theorem 4.3.1, we know that a small DGSM-based bound for a given parameter implies the corresponding total Sobol’ index is small, indicating the parameter is unimportant. In the present experiment, we set an *importance tolerance* of 0.05. A parameter whose DGSM-based bound is smaller than this importance tolerance will be considered unimportant. The results reported in Figure 4.3 indicate that unimportant parameters are given by θ_j with $j \in \{1, 4, 5, 7\}$. This is consistent with results reported in [6], where the statistical accuracy of the reduced model, obtained by fixing these unimportant parameters was demonstrated numerically. Both panels of Figure 4.3 show the same information; however, in the right panel we use a logarithmic scale in the vertical axis to clearly illustrate the bound derived in Theorem 4.3.1, for the small functional Sobol’ indices.

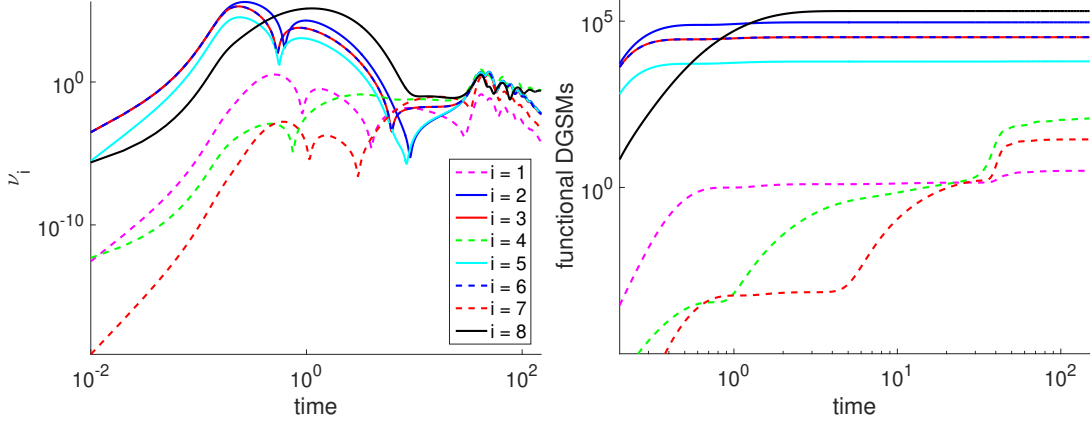


Figure 4.2 Pointwise-in-time DGSMs $v_j(I(t, \cdot))$ (left) and functional DGSMs $\mathfrak{R}_j(I; [0, t])$ (right) for $t \in [0, 150]$.

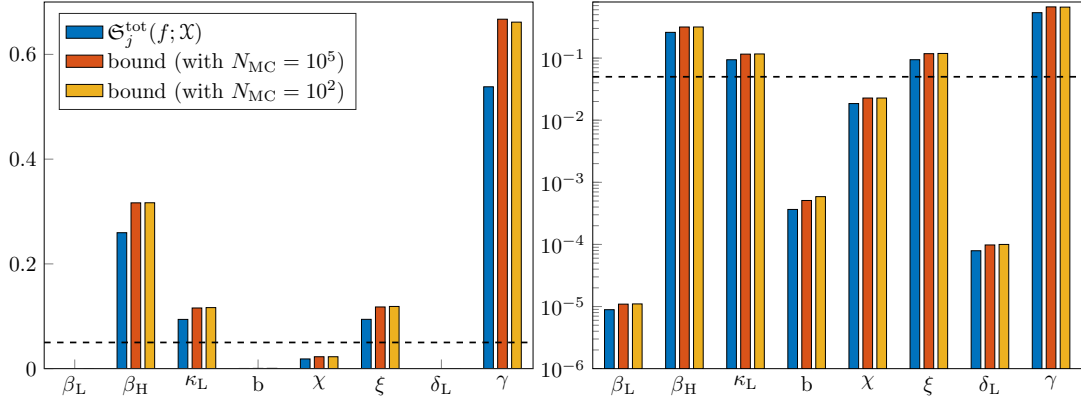


Figure 4.3 Left: The functional Sobol indices and the corresponding bounds proven in Theorem 4.3.1 for the cholera model; right: the same information as in the left plot, except we use log-scale on y -axis to clearly show $\mathfrak{S}_j^{\text{tot}}(I; \mathcal{X})$ and the corresponding bound, for small indices; the dashed black line indicates $y = 0.05$ that could be a reasonable tolerance to decide which random input is unimportant.

4.5.2 Sensitivity analysis in a subsurface flow problem

In this section, we elaborate our proposed approach for sensitivity analysis and dimension reduction on a model problem motivated by subsurface flow applications.

4.5.2.1 Model description

We consider the following equation modeling the fluid pressure in a single phase flow problem:

$$\begin{aligned}
 -\nabla \cdot \left(\frac{\kappa}{\eta} \nabla p \right) &= b, & \text{in } \mathcal{D} \\
 p &= 0 & \text{on } \Gamma_D, \\
 \frac{\kappa}{\eta} \nabla p \cdot n &= 0, & \text{on } \Gamma_N
 \end{aligned} \tag{4.26}$$

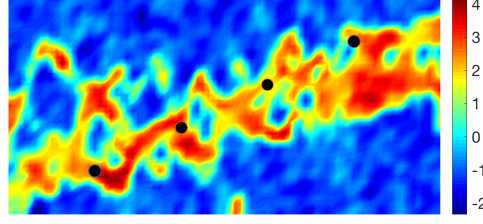


Figure 4.4 Mean log-permeability field. The black dots indicate point source locations.

The domain is $\mathcal{D} = (-1,1) \times (0,1)$, Γ_D is the union of the left, bottom, right parts of the boundary, and Γ_N is the top boundary. The right hand side function $b(x)$ is defined as a sum of mollified point sources, $b(x) = \sum_{i=1}^4 \alpha_i \delta_{x_i}(x)$, where

$$\delta_{x_i}(x) = \frac{1}{2\pi L} \left\{ -\frac{1}{2L} \|x - x_i\|_2^2 \right\},$$

with $x_1 = (-0.6, 0.2)$, $x_2 = (-0.2, 0.4)$, and $x_3 = (0.2, .6)$, and $x_4 = (0.6, 0.8)$. We chose $(\alpha_1, \alpha_2, \alpha_3, \alpha_4) = (2, 5, 5, 2)$. In this problem, we assume viscosity is $\eta = 1$ and consider uncertainties in the permeability field κ , which is modeled as a log-Gaussian process:

$$\log \kappa(x, \omega) =: a(x, \omega) = \bar{a}(x) + \sigma_a z(x, \omega), \quad x \in \mathcal{D}, \omega \in \Omega, \quad (4.27)$$

where Ω is an appropriate sample space, and $z(x, \omega)$ is a Gaussian process with mean zero and covariance function given by

$$c_z(x, y) = \exp \left\{ -\frac{|x_1 - y_1|}{\ell_x} - \frac{|x_2 - y_2|}{\ell_y} \right\}, \quad x, y \in \mathcal{D}.$$

In the present example, we use $\ell_x = 1/2$ and $\ell_y = 1/4$, implying stronger correlations in the horizontal direction. The covariance operator \mathcal{C}_{par} is defined by $\mathcal{C}_{\text{par}} u = \int_{\mathcal{D}} c_z(\cdot, y) u(y) dy$. The mean of the process $\bar{a}(x)$ is adapted from the simulated permeability data from the Society for Petroleum Engineers (SPE) 2001 Comparative Solutions Project [1]; see Figure 4.4. For this problem we use $\sigma_a = 1.6$. We use a truncated KLE to represent the log-permeability field:

$$a(x, \omega) \approx \bar{a}(x) + \sum_{k=1}^{N_p} \sqrt{\lambda_k(\mathcal{C}_{\text{par}})} \theta_k(\omega) e_k(x), \quad (4.28)$$

where θ_k , $k = 1, 2, \dots, N_p$ are independent standard normal random variables, and $\lambda_k(\mathcal{C}_{\text{par}})$ and $e_k(x)$ are the eigenpairs of the covariance operator \mathcal{C}_{par} of $a(x, \omega)$ (which is defined in terms of the correlation function c_z as before). Note that when using the truncated KLE, the uncertainty in the log permeability field is characterized by the random vector $\boldsymbol{\theta} =$

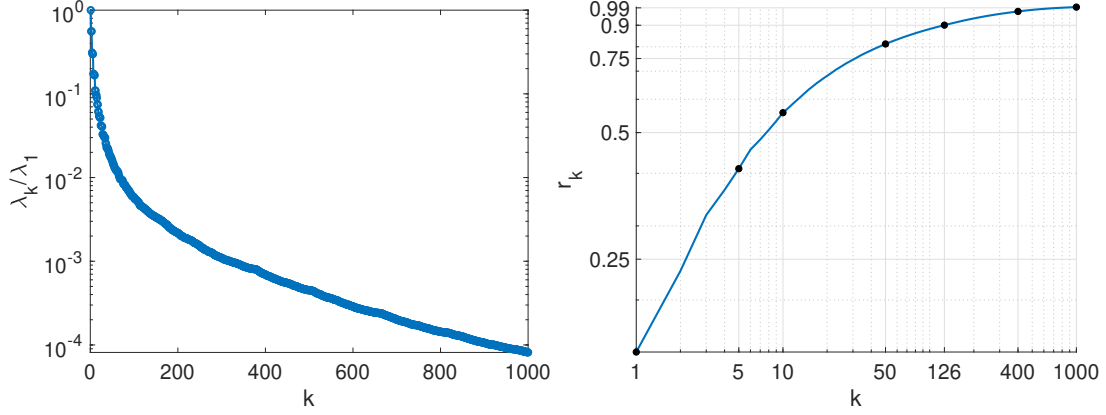


Figure 4.5 Left: the normalized eigenvalues of the log-permeability field covariance operator; right: the ratios r_k , for $k = 1, \dots, 1000$.

$$[\theta_1 \ \theta_2 \ \dots \ \theta_{N_p}]^T \in \mathbb{R}^{N_p}.$$

To establish the truncation level, we consider the ratio

$$r_k = \frac{\sum_{i=1}^k \lambda_i}{\sum_{i=1}^{\infty} \lambda_i}, \quad k = 1, 2, 3, \dots,$$

where λ_i 's are the eigenvalues of the covariance operator \mathcal{C}_{par} . We depict the normalized eigenvalues, λ_k/λ_1 in Figure 4.5 (left) and plot the ratios r_k , for $k = 1, \dots, 1000$. We find that $r_k > 0.9$, for $k = 126$; thus, we retain $N_p = 126$ in the KLE of the log-permeability field. We will see shortly (see section 4.5.2.3) that this is an unnecessarily large parameter dimension for the quantity of interest under study.

As an illustration, in Figure 4.6, we show two realizations of the resulting log-permeability field (left) along with the corresponding pressure fields (right) obtained by solving (4.26).

4.5.2.2 The quantity of interest and its spectral representation

We consider the following quantity of interest:

$$f(x, \boldsymbol{\theta}) := p(x, \boldsymbol{\theta})|_{\Gamma_N}.$$

A few realizations of $f(x, \boldsymbol{\theta})$ are plotted in (4.7) (left). To compute the KLE of f , we use a sample average approximation of its covariance function, which is then used to solve the discretized generalized eigenvalue problem for its KL modes. The first 30 normalized eigenvalues of the covariance operator of f , which we denote by \mathcal{C}_{qoi} , are plotted in Figure 4.7 (middle, red color); these correspond to computing the KLE of the QoI using sampling with a Monte Carlo (MC) sample of size $N_{\text{MC}} = 1000$. We also plot the eigenvalues of the log-permeability field covariance operator \mathcal{C}_{par} , in the same plot (blue color); note that the eigenvalues of \mathcal{C}_{qoi} decay significantly faster than those of \mathcal{C}_{par} , as expected. To assess the impact of the MC

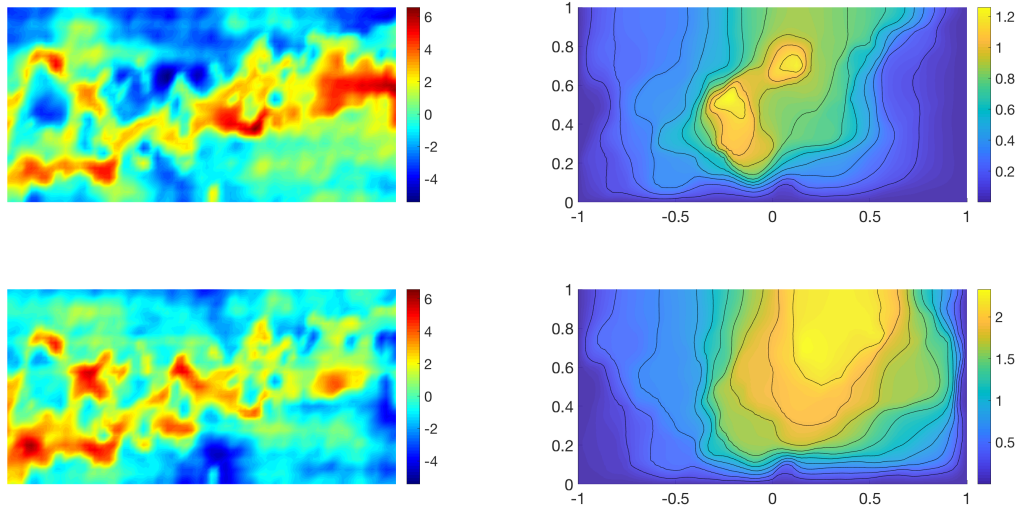


Figure 4.6 Realizations of the log-permeability field (left), and the corresponding pressure fields (right).

sample size on computation of the dominant eigenvalues of \mathcal{C}_{qoi} , we report the normalized eigenvalues of \mathcal{C}_{qoi} computed using successively larger sample sizes, in Figure 4.7 (right). We observe that a sample of size $\mathcal{O}(100)$ can be used for computing the dominant eigenvalues reliably.

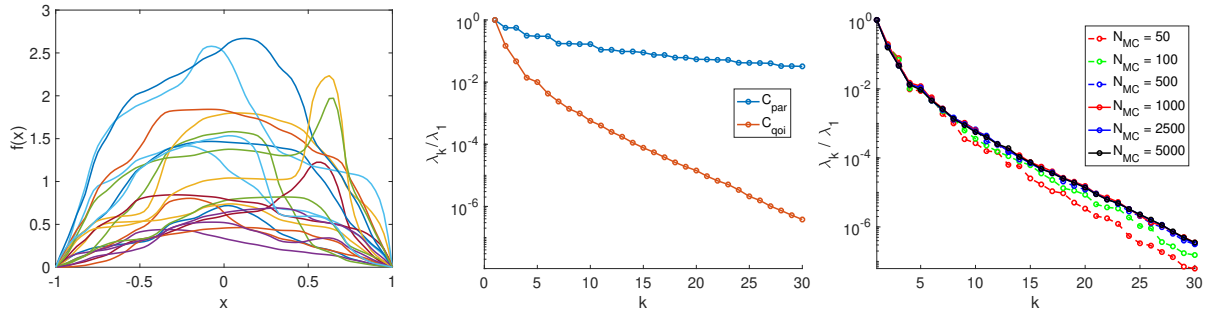


Figure 4.7 A few realizations of the QoI (left), eigenvalues of the output covariance operator versus those of the log-permeability field (middle). Eigenvalues of the output covariance, with successively larger MC samples sizes for computing the output KLE (right).

The fast decay of eigenvalues of \mathcal{C}_{qoi} indicates the potential for output dimension reduction. We note four orders of magnitude reduction in the size of the eigenvalues of \mathcal{C}_{qoi} with

only 15 modes in Figure 4.7 (right). Hence, we consider a low-rank approximation of f ,

$$f(x, \boldsymbol{\theta}) \approx \hat{f}(x, \boldsymbol{\theta}) = \bar{f}(x) + \sum_{i=1}^{N_{\text{qoi}}} \sqrt{\lambda_i(C_{\text{qoi}})} f_i(\boldsymbol{\theta}) \phi_i(x) \quad (4.29)$$

with $N_{\text{qoi}} = 15$. While this provides a low-rank approximation to f , the dimension of $\boldsymbol{\theta}$ is still high, and is determined by the truncation of the KLE of the log-permeability field at $N_p = 126$. Below, we use global sensitivity analysis to reduce the dimension of $\boldsymbol{\theta}$.

4.5.2.3 Derivative-based GSA

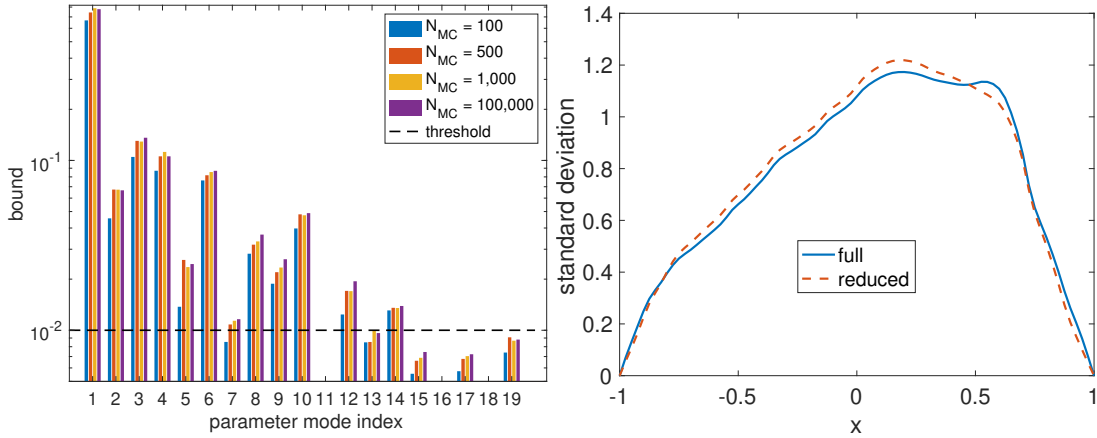


Figure 4.8 Left: DGSM-based bound in (Theorem 4.3.1) calculated for various sample sizes. Right: standard deviation fields for full model versus that of the reduced model.

We begin by calculating the DGSM-based bounds on functional Sobol' indices from (Theorem 4.3.1) for \hat{f} defined in (4.29). As seen before, this process requires sampling the QoI; we compute the DGSM-based bounds by using MC samples of size $N_{\text{MC}} = 100, 500, 1,000$, and 100,000. The resulting bounds for the first 19 parameters are reported in Figure 4.8 (left).

Note that Figure 4.8 (left) displays the bounds for only the first 19 modes, because the bounds for the remaining 107 modes were all well below the chosen importance tolerance of 0.01. We note that the results calculated with $N_{\text{MC}} = 500, 1,000$, and 100,000 provide a consistent classification of important and unimportant parameters. This indicates that in practice, a modest sample size is sufficient for obtaining informative estimates of the DGSM-based bounds from (Theorem 4.3.1).

The computed DGSM-based bounds indicate that the parameter KL modes θ_j , with $j \in \{1, 2, 3, 4, 5, 6, 7, 8, 9, 10, 12, 14\}$ were above the chosen importance tolerance of 0.01 and the remaining modes can be fixed at a nominal value of zero. This effectively reduces the parameter dimension from $N_p = 126$ to $N_p = 12$. We denote the resulting reduced model, now a function

of only 12 variables, by f^r . To test that f^r reliably captures the variability of the true model f , we sample both reduced and full models 10^5 times to compare their statistical properties. In Figure 4.8 (right), we compare the standard deviation of the full and reduced models over the spatial domain $\mathcal{X} = [-1, 1]$ of the QoI. In Figure 4.9 we report PDFs of $f(x, \cdot)$ and $f^r(x, \cdot)$, at $x = -0.75, -0.25, 0.25, 0.75$. We note that the reduced model captures the distribution of the QoI at the considered points closely.

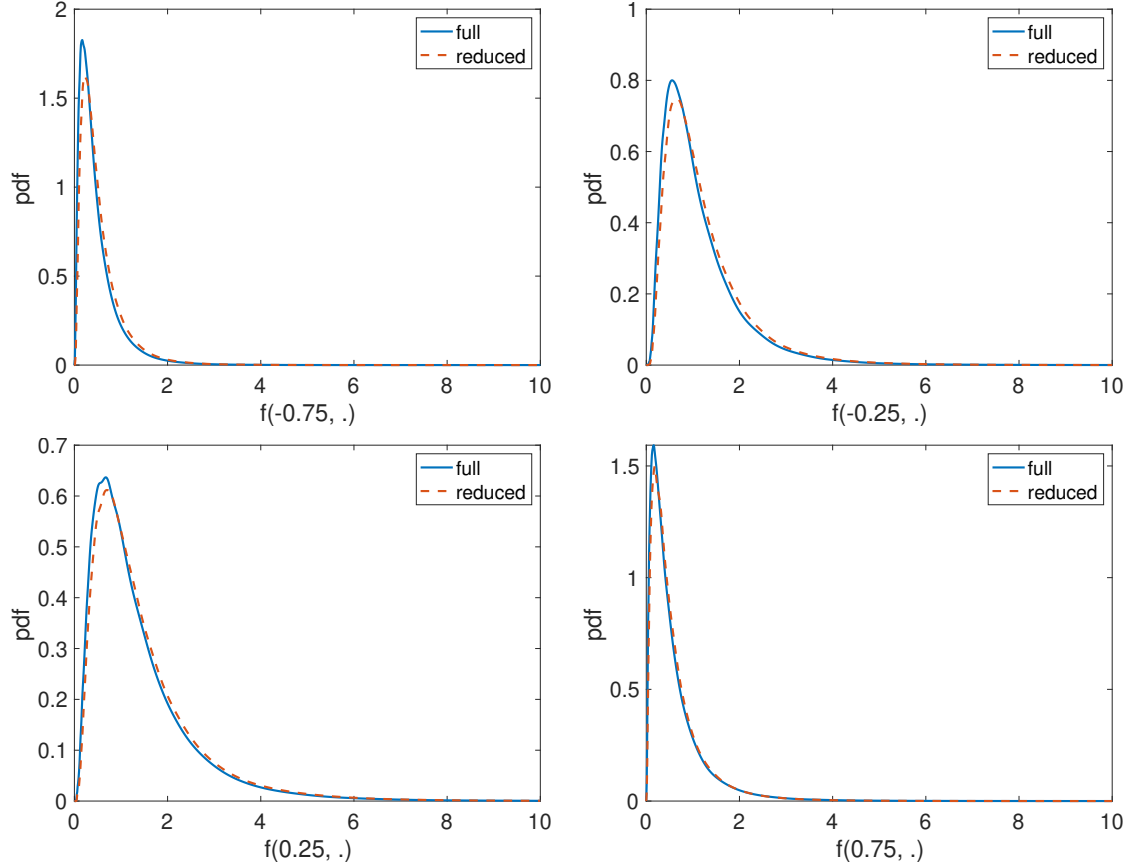


Figure 4.9 pdf estimate for equally spaced points, $[-1, 1]$.

4.5.3 Application to biotransport in tumors

In this section, we apply our derivative-based GSA methods to a biotransport problem. Specifically, we consider biotransport in cancerous tumors with uncertain material properties. We focus on the resulting uncertainties in the pressure field in a spherical tumor when a single needle injection occurs at the center of the tumor.

4.5.3.1 Model description

Restricting our attention to a 2D cross-section, we consider Darcy's law constrained by conservation of mass in a 2D physical domain $\mathcal{D} \subset \mathbb{R}^2$ given by a circle of radius $R_{\text{tumor}} = 5$ mm with an inner circle of radius $R_{\text{needle}} = 0.25$ mm, modeling the injection site, removed; see Figure 4.10. The inner and outer boundaries of the physical domain \mathcal{D} are denoted by Γ_N and Γ_D , respectively. The fluid pressure p is governed by the following elliptic PDE:

Table 4.2 Model parameters for the biotransport problem.

Parameter	Symbol	Nominal Value [unit]
Permeability	κ	0.5 [md]
Viscosity	η	8.9×10^{-4} [Pa · s]
Inflow rate	Q	1 [mm ² / min]

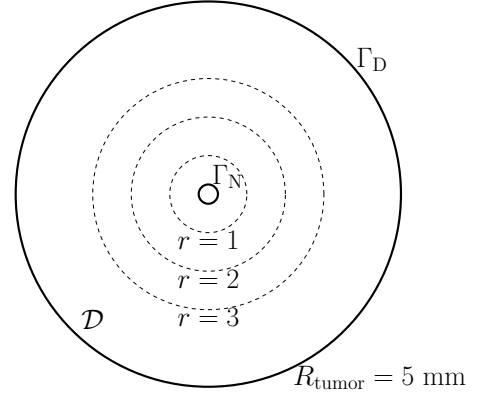


Figure 4.10 The domain \mathcal{D} . The inner and outer boundaries are equipped with Neumann and Dirichlet boundary conditions and are denoted by Γ_N and Γ_D , respectively.

$$\begin{aligned}
 -\nabla \cdot \left(\frac{\kappa}{\eta} \nabla p \right) &= 0 \quad \text{in } \mathcal{D}, \\
 p &= 0 \quad \text{on } \Gamma_D, \\
 \nabla p \cdot n &= \frac{Q\eta}{2\pi R_{\text{needle}}\kappa} \quad \text{on } \Gamma_N.
 \end{aligned} \tag{4.30}$$

Here κ is the absolute permeability field, η is the fluid dynamic viscosity, Q represents the volume flow rate per unit length, and n is the outward-pointing normal of the inner boundary Γ_N . The nominal values for the parameters in (4.30) are given in Table 4.2. These values are selected according to those used in previous experimental and numerical studies of fluid transport in tumors [24, 67, 87]. As has been discussed by many researchers, tumor structure can be highly complicated due to its invasive nature. In general, a tumor consists of loosely organized abnormal cells, fibers, vasculature, and lymphatics [23]. This results in randomly formed tumor tissues with structural heterogeneity.

In this subsection, the permeability field is modeled as a log-Gaussian random field as

follows. Let $z(x, \omega)$ be a centered Gaussian process with the following covariance function:

$$c_z(x, y) = \exp \left\{ -\frac{1}{\ell} \|x - y\|_1 \right\}, \quad x, y \in \mathcal{D}, \quad (4.31)$$

where $\ell > 0$ is the correlation length. Then, we define the log-permeability $a = \log \kappa$ as in (4.27), where the pointwise mean and variance of the process are given by $\bar{a} \equiv \ln(0.5) + \sigma_a^2$ and $\sigma_a^2 = 0.25$, respectively. Note that \bar{a} is selected to ensure that the mode of the κ distribution at each spatial point is 0.5 md , which is the nominal value for κ given in Table 4.2. We can represent $a(x, \omega)$ using a truncated KLE as in (4.28).

4.5.3.2 The quantity of interest and its spectral representation

We consider the following QoI:

$$f(x, \theta) = \mathcal{Q}p, \quad (4.32)$$

where, as in section 4.4, \mathcal{Q} is the restriction operator to a closed subset \mathcal{X} of \mathcal{D} . In this case, \mathcal{X} is an annulus with the inner boundary given by the inner boundary Γ_N of \mathcal{D} and with the outer boundary having a radius $R_{out} = 1 \text{ mm}, 2 \text{ mm}, \text{ or } 3 \text{ mm}$ (see Figure 4.10). The corresponding truncated KLE of f reads

$$\hat{f}(x, \theta) := \bar{f}(x) + \sum_{k=1}^{N_{\text{qoi}}} \sqrt{\lambda_k(\mathcal{C}_{\text{qoi}})} f_k(\theta) \phi_k(x), \quad (4.33)$$

where the KL modes f_i are defined as before, and $\lambda_k(\mathcal{C}_{\text{qoi}})$ and $\phi_k(x)$ are the eigenpairs of the QoI covariance operator \mathcal{C}_{qoi} .

4.5.3.3 Derivative-based GSA

As in section 4.5.2.3, we calculate the DGSM-based bounds on functional Sobol' indices from Theorem 4.3.1 for the QoI defined in (4.33) and follow the adjoint-based framework outlined in section 4.4. As mentioned previously, a small DGSM-based bound for a given parameter implies that the corresponding functional total Sobol' index is small and thus, the parameter is deemed unimportant. In the experiments in this section, we set an *importance tolerance* of 0.025. In Figure 4.11, we study the effects of the MC sampling size N_{MC} , the KLE dimension N_p of the input and N_{qoi} of the output, annulus size (i.e., size of \mathcal{X}), and correlation length ℓ on DGSM-based bounds. Note that Figure 4.11 displays the DGSM-based bounds for the first 37 modes, beyond which the DGSM-based bounds were all below the chosen importance tolerance. Below, we explain the numerical experiments reported in Figure 4.11, in detail.

In the first test, we examine the effect of the MC sample size N_{MC} as needed in our approach for computing DGSMs (see Algorithm 2). Similar to the observation in section 4.5.2.3, a modest sample size is sufficient for obtaining informative estimates of the DGSMs. Specifically, we present one set of test results in Figure 4.11 (top left). Here, the outer radius of the

annulus is 1 *mm*, the correlation length is 0.5 *mm*, and we consider an input dimension of $N_p = 150$, and an output dimension of $N_{qoi} = 50$. We observe that a sample size of $N_{MC} = 750$ is sufficient for obtaining a reliable estimation of DGSMs-based bounds. Therefore, the MC sample size in the following tests is fixed at $N_{MC} = 750$.

We then test the effects of the annulus size and correlation length on DGSMs. In these tests, the input and output dimensions are $N_p = 150$ and $N_{qoi} = 50$, respectively. From Figure 4.11 (top right and bottom left), we observe that when the annulus size increases or the correlation length decreases, the QoI is sensitive to more KL terms of the input. Interestingly, most of these sensitive parameters are from relatively high-order terms. For example, as shown in Figure 4.11 (bottom left), when the correlation length decreases from 2.0 *mm* to 0.5 *mm*, the importance of KL modes θ_j , with $j \in \{9, 10, 17, 22, 23\}$ gradually grow. Implication of such issues on reduced-order modeling (ROM) will be discussed in the next section. Next, we examine the impact of increasing N_p and N_{qoi} . As seen in Figure 4.11 (bottom right), increasing the input and output dimensions beyond the selected values of $N_p = 150$ and $N_{qoi} = 50$ does not result in noticeable changes in DGSM estimates.

4.5.3.4 Insights on ROM assisted by DGSMs

From the global sensitivity analysis, we find that the QoI is only sensitive to several selected KL terms of the input. This can be used to guide ROM based on DGSMs. In this section, we compare two ROM approaches: one is based on the GSA with DGSMs (termed as DGSM-based ROM) and the other is based on directly selecting the first k -terms of the KLE of the random input field (termed as KL-based ROM). Generally, the reduced-order model of the input can be written as follows:

$$\tilde{a}(x, \omega) = \bar{a}(x) + \sum_{k \in \mathcal{S}} \sqrt{\lambda_k(C_{\text{par}})} \theta_k(\omega) e_k(x), \quad (4.34)$$

where \mathcal{S} is the set which consists of the indices of the KL terms used in ROM. We evaluate the performance of the two ROM methods on recovering the PDFs of pressures at different locations in the flow field.

As shown in Figure 4.12, we select three points on the mesh with different distances from the center of the domain: the point P_1 is on the inner boundary with a large relative standard deviation (RSD) of the pressure ($RSD = 0.143$); the point P_2 is close to the inner boundary with a moderate RSD ($RSD = 0.105$); and the point P_3 is far from the inner boundary with a relatively small RSD ($RSD = 0.0845$). In the DGSM-based ROM, the first n KL terms which the QoI is most sensitive to are used to reconstruct the reduced-order model of the pressure field. In the KL-based ROM, the first n KL terms, corresponding to the n largest eigenvalues of the input covariance operator, are used to reconstruct the reduced-order model. An MC sampling approach is used to construct PDFs from the full model, which includes all the KL terms, and those from the reduced-order models with different fidelities. The case with a

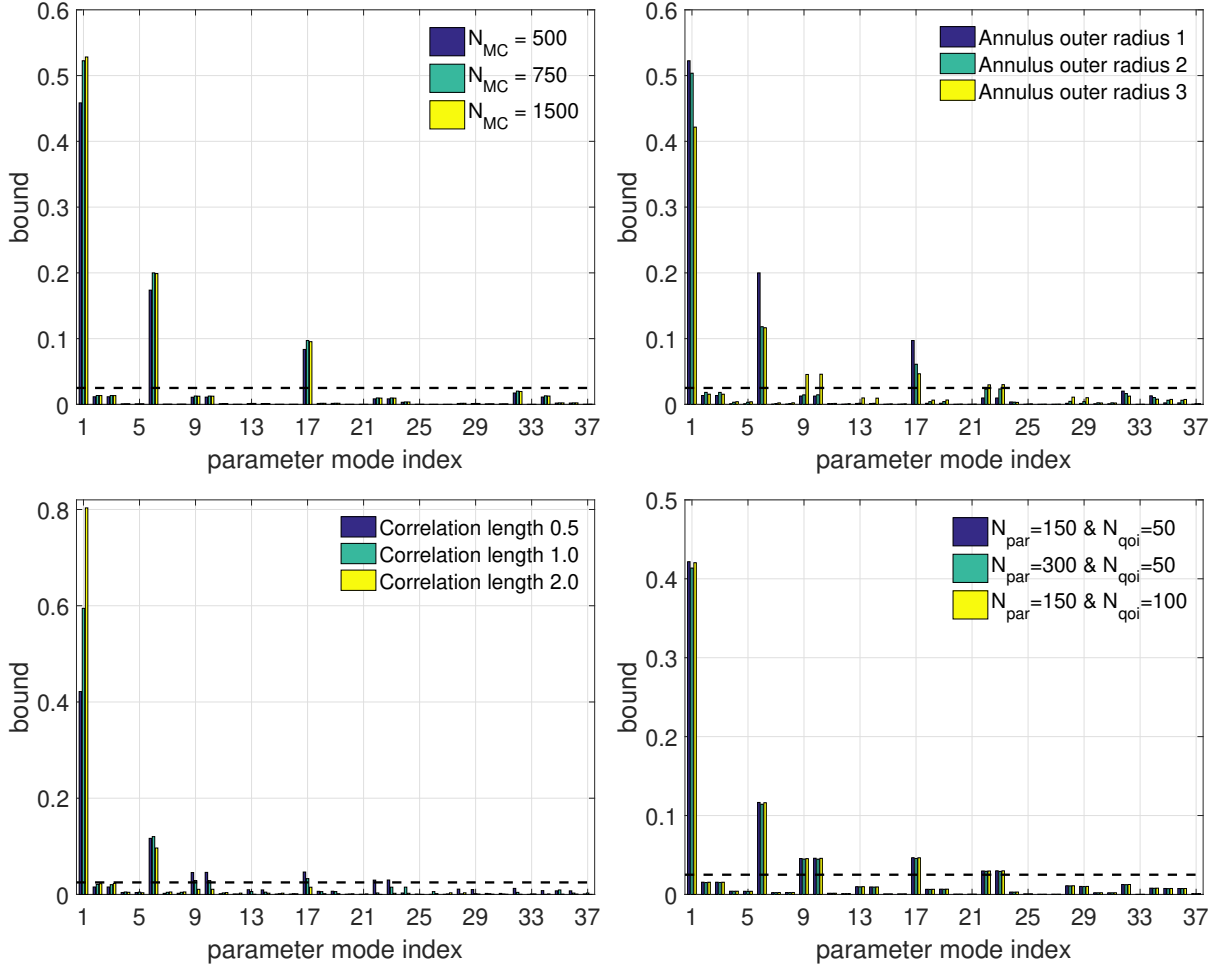


Figure 4.11 The functional DGSM-based bounds of pressure fields in a tumor with uncertain permeability. Top left: Convergence study with the MC sample size $N_{MC} = 500, 750$, and 1500 . Top right: Comparison of DGSM-based bounds for different annulus sizes, namely the annulus outer radii of 1 mm , 2 mm , and 3 mm . Bottom left: Comparison of DGSM-based bounds for different correlation lengths, namely 0.5 mm , 1 mm , and 2 mm . Bottom right: DGSM-based bounds calculated with different combinations of the KLE dimensions of the input and output.

small correlation length ($\ell = 0.5\text{ mm}$) and a large annulus size ($R_{out} = 3\text{ mm}$) is studied here. An MC sample of size 6000 was found sufficient for constructing the PDFs.

From Figure 4.13, we observe that at P_1 , where the pressure variance is large, the reduced-order model with only the first seven most sensitive KL terms can nearly recover the PDF of the full model. Its performance is comparable to that of the KL-based ROM with the first 30 KL terms. This is not a surprise, because, as seen from the last figure in Figure 4.11, the first seven most sensitive KL terms θ_j , with $j \in \{1, 6, 9, 10, 17, 22, 23\}$, are within the first 30 KL terms used in the KL-based ROM. Similar conclusions can be drawn at P_2 where a moderate pressure variance is observed. At P_3 , we find that the DGSM-based ROM with the first seven most sensitive KL terms does not recover the PDF well; however, the PDFs obtained using

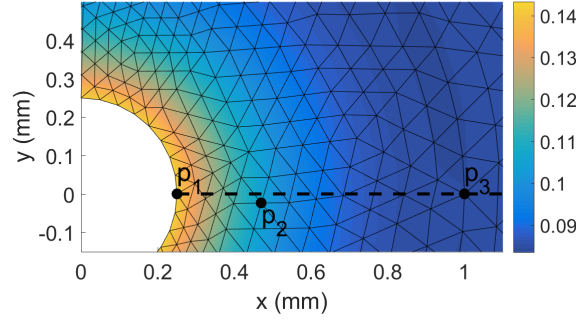


Figure 4.12 Distribution of the points where PDFs of pressures are extracted, and the corresponding RSD field (contour).

the DGSM-based ROMs with more KL terms, such as that with the first 15, 30 and 45 most sensitive KL terms, gradually approach the PDF of the full model. On the other hand, with the same number of KL terms, the KL-based ROM makes very slow progress towards the full model PDF. All these observations indicate that the DGSM-based ROM can be a much more efficient reduced-order modeling approach than the KL-based ROM that involves a priori truncation of

4.6 Conclusions

We have presented a mathematical framework for GSA of models with functional outputs, and have proposed an efficient computational method for identifying unimportant inputs that is suitable for models with high-dimensional parameters. The latter is done by combining the proposed functional DGSMs, “low-rank” KLEs of output QoIs, and adjoint-based gradient computation. In particular, the computational complexity of the proposed approach, in terms of the number of required model evaluations, does not scale with dimension of the parameter. The effectiveness of the proposed framework is illustrated numerically in applications from epidemiology, subsurface flow, and biotransport.

The proposed approach is effective in finding unimportant input parameters. This approach also paves the way for an efficient surrogate modeling approach: the low-rank KLE of the model output can be used to construct efficient-to-evaluate surrogate models by computing surrogate models for the KL modes, in the reduced parameter space, which is identified using the functional DGSMs. The latter can be done using various methods including orthogonal polynomial approximations [63, 98, 110], multivariate adaptive regression splines [40], or active subspace approaches [27]. We mention that active subspace methods have also been used directly for dimension reduction in models with vectorial outputs. Namely, [114]

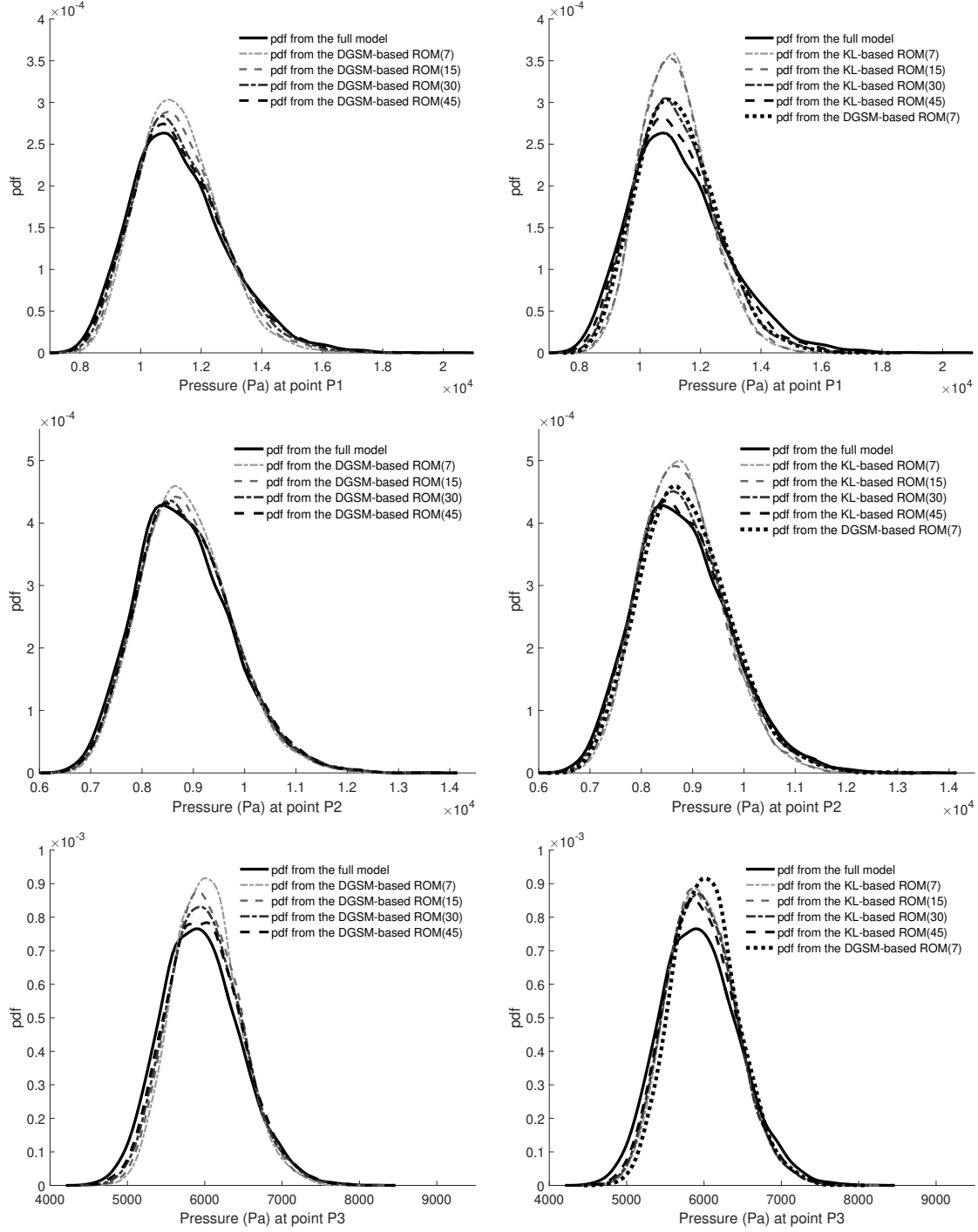


Figure 4.13 Comparison of PDFs constructed from the DGSM-based ROM (left column) and KL-based ROM (right column) with variable fidelity at points P_1 , P_2 and P_3 .

presents a gradient-based input dimension reduction method for such models. The method proposed in [114] finds a set of important *directions* in the input parameter space by considering ridge approximations of the model output and by minimizing an upper bound on the

approximation error. The approach in [114] is related to the present work when the goal of GSA is input dimension reduction.

In future work, we seek to investigate generalizations to cases of models with correlated inputs. While the proposed DGSMs can be computed for such models in the same way, the corresponding variance-based indices need to be generalized. We are also interested in applying the proposed method to more complex physical applications such as multiphase flow in geological formations.

GLOBAL SENSITIVITY DRIVEN INPUT DIMENSIONALITY REDUCTION FOR REAXFF PARAMETERIZATIONS OF SILICA-BASED GLASSES

The contents of this chapter is related to the work published in [85]. The author of the present thesis is also lead author on this publication. We would like to give special thanks to Mark Wilson and Sandia National Laboratories for the opportunity to pursue this work.

5.1 Introduction

Molecular dynamics (MD) simulations with reactive potentials provide the capability to gain chemically specific, atomic-scale insight into a broad range of material science applications with examples including dislocation dynamics, chemical kinetic processes, and crack propagation. Each of these examples represent a complex dynamic process where MD can expose the atomic-scale origins of the given phenomena, which can prove useful for designing preventative or predictive measures.

ReaxFF is a reactive interatomic potential [21, 106, 107] which can be utilized by the MD simulation package LAMMPS [82]. Given an accurate parameterization, LAMMPS paired with ReaxFF is capable of computing highly specific chemical data. Every unique material system and physics of interest requires a corresponding unique parameterization. There are 72 parameters involved in a reactive potential parameterization for a single element, and for compounds involving multiple distinct elements the parameter dimension is significantly larger. Due in part to the sheer amount parameters that need to be estimated, creating novel parameterizations is a challenging and time consuming task. To make ReaxFF more extensible for projects that require fast analysis of novel (multi-component) material systems, in the present work we use global sensitivity analysis (GSA) to identify non-influential parameters to the ReaxFF parameterization.

We focus our analysis on a well-utilized, existing parameterization for the elements silicon (Si) and oxygen (O) in the context of silica-based glasses [81]. We study a variety of quantities of interest (QoIs) corresponding to the energetic interactions between Si and O, and screen for non-influential parameters by computing derivative-based global sensitivity measures (DGSMs) [25, 57] for the associated input parameters. The studied QoIs include isolated (single) atom energy, radial bond energy, and angular bending energy.

This chapter is organized as follows: In section 5.2, we explain the uncertain parameter space and give a brief overview of the studied objectives. We provide a set of numerical results and explanations in section 5.3. Lastly, in section 5.4, we include possibilities for future work and closing remarks.

5.2 ReaxFF parameters and QoIs

We provide a brief overview of how ReaxFF works, the parameters associated with a given compound, and expand on the QoIs to be studied.

Parameters of ReaxFF. ReaxFF is a bond order-based interatomic potential, which means it treats bond order as a continuous function of interatomic distance. Due in part to this modeling approach, ReaxFF is able to compute atomic-scale chemical behavior. ReaxFF is known for its near-first principles accuracy. For brevity we do not include the precise analytical equations in the present work. A detailed breakdown of the analytical form of the involved potentials can be found in [106].

There are six different *parameter types* in the ReaxFF potentials: *atom-type*, *bond-type*, *off-diagonal-type*, *angle-type*, *torsion-type*, and *hydrogen bond-type*. Furthermore, depending on the compound being considered and the QoI being studied, different sub-groupings of elements have their own subset of parameters. In the present work, we study compounds containing O and Si, arranged in varying combinations, and involving up to four total atoms. We use the subscripts 1 and 2 to indicate O and Si, respectively. Therefore, we denote the parameter type subsets as θ_i^a , θ_{ij}^b , θ_{ij}^{od} , θ_{ijk}^{ag} , θ_{ijkl}^t for types atom-type i , bond-type i - j , off-diagonal-type i - j , angle-type i - j - k and torsion-type i - j - k - l , respectively, for $i, j, k, l \in \{1, 2\}$. Note that we do not have a notation for hydrogen bond parameters because the simulations in the present work do not involve the element hydrogen. Consequently, hydrogen bond parameters are unnecessary.

Not all of input parameters are uncertain. For example, there is an atom-type parameter corresponding to atomic mass—a known value for all elements in the periodic table. Therefore, this parameter is fixed for every element. In Table 5.1 we summarize the input parameters for each QoI.

The input parameters are assumed to be independent, and uniformly distributed such that $\theta_j \sim \mathcal{U}(a_j, b_j)$ where a_j and b_j are the lower and upper bounds corresponding to parameter θ_j . The upper and lower bound for each parameter were determined by numerical experimentation. The interval for each θ_j was established around the published values defined in the

Table 5.1 Summary of the studied QoIs, corresponding x units, and involved parameters. Note that for QoIs B_{ij} , and A_{ijk} , $i, j, k \in \{1, 2\}$, the inclusion of certain subsets of θ_{ij}^{od} , θ_{ijk}^{ag} , and θ_{ijkl}^t in θ depends on the compound being modeled.

Symbol	QoI	x units	involved parameters
$S_i(\theta)$	single atom energy	none	$\theta = [\theta_i^a]^\top$
$B_{ij}(x, \theta)$	radial bond energy	Angstrom	$\theta = [\theta_i^a \theta_{ij}^b \theta_{ij}^{od}]^\top$
$A_{ijk}(x, \theta)$	angular bending energy	degree	$\theta = [\theta_i^a \theta_{ij}^b \theta_{ij}^{od} \theta_{ijk}^{ag} \theta_{ijkl}^t]^\top$

work of Pitman et al [81]. Then, the QoI functions were evaluated with parameters sampled from these intervals. Upper and lower bounds were modified until regions were found for which LAMMPS and ReaxFF did not error. The intention was to test the extent at which the parameter space is limited by the calculation done by LAMMPS and ReaxFF, rather than by the physical meaning of the parameters.

QoI overview. We consider three QoI types: isolated (single) atom energy, radial bond energy, and angular bending energy. We denote these QoIs as $S_i(\theta)$, $B_{ij}(x, \theta)$, and $A_{ijk}(x, \theta)$, respectively. The subscripts $i, j, k \in \{1, 2\}$, correspond to the element numbers. We assume a QoI depends on all possible relevant parameters. Assuming very little about which input parameters are relevant to a QoI allows us to develop a framework that can be applied to a wide range of QoIs. Note, the single atom energy is a function of the input parameters θ only, while the remaining two QoIs are also functions of an independent state variable x . A summary of the QoIs and corresponding input parameters is provided in Table 5.1. Note that the parameter type subsets required for a particular combination of QoI and compound can vary. Specifically, certain parameter subsets are only included if they have physical meaning. For example, there are no off-diagonal interactions in the B_{ij} when $i = j$. Therefore, θ_{jj}^{od} would not be included in θ in this instance.

We compare the following examples for clarity. Consider the radial bond energy between O and Si. This QoI is denoted by $B_{12}(x, \theta)$, where x corresponds to the distance between the two atoms measured in Angstroms. In this case $\theta = [\theta_1^a \theta_2^a \theta_{12}^b \theta_{12}^{od}]^\top$. We compare this with the radial bond energy between O and O. This QoI is denoted by $B_{11}(x, \theta)$, with $\theta = [\theta_1^a \theta_{11}^b]^\top$. Note that modeling more complex molecules will require even larger input parameter sets, leading to a rapid increase in parameter dimension. This emphasizes the need for efficient input dimension reduction.

We briefly describe the LAMMPS simulation for each QoI studied. For $S_i(\theta)$ a single atom is placed in a "box", and LAMMPS calculates the associated potential energy. For $B_{ij}(x, \theta)$, two atoms are placed 1 Angstrom apart and then separated to a distance of 14.9 Angstrom. LAMMPS calculates the potential energy of the bond at intervals of 0.1 Angstrom. For this QoI x represents distance. The simulation for $A_{ijk}(x, \theta)$ involves three atoms. The atoms are initialized with an angle of 10 degrees between them. Then, a radial atom is moved until the

angle between all three atoms is equal to 180 degrees. LAMMPS measures the angular energy at ten degree intervals. In this case, x corresponds to degrees.

5.3 Numerical results

We consider compounds combining the elements O and Si that involve up to four atoms. We use 1 to label O atoms and 2 to label Si atoms. and compute the derivative-based global sensitivity measures (DGSMs) for a variety of QoIs. (Definitions and properties for scalar DGSMs and functional DGSMs were covered in sections 2.2 and 4.3 of this thesis, respectively.) Parameters with DGSMs equal to zero are considered non-influential. Note, this is an extremely tight tolerance. Our intention was to eliminate only the parameters that had no impact on the studied QoIs. In future work, it would be possible to raise this tolerance and eliminate a larger subset of inputs. For all DGSM computations we use finite differences to approximate the partial derivatives, and for the function-valued QoIs we use the composite trapezoid rule to compute the integral over the state space. A summary of the studied QoIs, total number of parameters, non-influential parameter numbers, and total amount of QoI samples used is provided in Table 5.2. We denote the number of samples used to estimate the integral over the parameter space as N_s . Note that N_s varies slightly for some of the studied QoIs. This is because for some of the QoIs a small number of the simulations were abandoned due to timeout error.

Isolated (Single) Atom Energy. Recall, $S_j(\theta)$, $j = 1, 2$ is a scalar QoI, corresponding to the isolated (single) atom energy. We fix six of the atom-type parameters and assume $S_j(\theta)$ is a function of the remaining $N_p = 26$ atom-type parameters. Using a sample size of $N_s = 1,000$ we compute the DGSMs for both element 1 and element 2. Observe that from the original 26 input parameters, 24 are non-influential. This suggests that the single atom energy for both O and Si depends on the same two input parameters, only.

Radial Bond Energy. Next, we compute the functional DGSMs for the radial bond energy $B_{ij}(x, \theta)$. In the case of $i = j = 1, 2$ the radial bond energy is assumed to be a function of $N_p = 42$ atom-type and bond-type parameters. Recall, there are no off-diagonal-type parameters when $i = j$. We compute the functional DGSMs for B_{11} and B_{22} with $N_s = 1,000$. The QoI B_{11} has 12 non-influential parameters and B_{22} has 17 non-influential parameters. Therefore, the input parameter dimension of B_{11} and B_{22} can be reduced to 30 and 25, respectively. Note, there were several parameters that were influential for B_{11} that were non-influential for B_{22} . This could be due in part to the differences in the atomic structure of the two different elements, and the associated bonding behaviors.

We also compute the functional DGSMs for B_{12} with $N_s = 1,000$. This QoI is assumed to be a function of two sets of atom-type parameters, one set of bond-type parameters, and one set of off-diagonal-type parameters. After excluding fixed parameters the input parameter dimension for B_{12} is $N_p = 73$. There are 33 non-influential parameters, reducing the input

Table 5.2 List of studies performed in this work. Each quantity of interest (QoI), isolated (single) atom energy ($S_i(\theta)$) radial bond energy ($B_{ij}(x, \theta)$), angular bending energy ($A_{ijk}(x, \theta)$) is listed with their respective varied parameters, total number of samples (N_s), total non-influential parameters, and number of samples with LAMMPS errors (N_e). Subscripts denote atom types, where 1 represents O and 2 represents Si.

QoI	parameters	N_p	non-influential	N_s	N_e
$S_1(\theta)$	$[\theta_1^a]^T$	26	24	1000	0
$S_2(\theta)$	$[\theta_2^a]^T$	26	24	1000	0
$B_{11}(x, \theta)$	$[\theta_1^a \theta_{11}^b]^T$	42	12	1000	0
$B_{22}(x, \theta)$	$[\theta_2^a \theta_{22}^b]^T$	42	17	1000	0
$B_{12}(x, \theta)$	$[\theta_1^a \theta_2^a \theta_{12}^b \theta_{12}^{od}]^T$	73	33	1000	0
$A_{111}(x, \theta)$	$[\theta_1^a \theta_{11}^b \theta_{111}^{ag} \theta_{1111}^t]^T$	56	15	1000	0
$A_{222}(x, \theta)$	$[\theta_2^a \theta_{22}^b \theta_{222}^{ag}]^T$	49	12	991	9
$A_{122}(x, \theta)$	$[\theta_1^a \theta_2^a \theta_{11}^b \theta_{12}^b \theta_{12}^{od} \theta_{122}^{ag} \theta_{212}^{ag}]^T$	103	28	974	26
$A_{212}(x, \theta)$	$[\theta_1^a \theta_2^a \theta_{12}^b \theta_{22}^b \theta_{12}^{od} \theta_{122}^{ag} \theta_{212}^{ag}]^T$	103	27	980	20
$A_{121}(x, \theta)$	$[\theta_1^a \theta_2^a \theta_{11}^b \theta_{12}^b \theta_{12}^{od} \theta_{121}^{ag} \theta_{112}^{ag} \theta_{1111}^t]^T$	110	31	988	12
$A_{112}(x, \theta)$	$[\theta_1^a \theta_2^a \theta_{11}^b \theta_{12}^b \theta_{12}^{od} \theta_{121}^{ag} \theta_{112}^{ag} \theta_{1111}^t]^T$	110	21	984	16

dimension from 73 to 40.

Angular Bending Energy. Recall, $A_{ijk}(x, \theta)$ represents the angular bending energy. For the case when $i = j = k = 1$ A_{111} is a function of $N_p = 56$ atom-type, bond-type, angle-type, and torsion-type parameters. For $i = j = k = 2$ A_{222} is a function of $N_p = 49$ atom-type, bond-type, and angle-type parameters. We compute the DGSMs for A_{111} with $N_s = 1,000$ and determine there are 15 non-influential parameters. Similarly, we use $N_s = 991$ to compute the DGSM values for A_{222} . This QoI had 13 non-influential parameters. The 2 parameter difference between A_{111} and A_{222} could once again be a consequence of the atomic structure of the two different elements, and the associated bonding behaviors.

The QoIs A_{122} and A_{212} are functions of $N_p = 103$ atom-type, bond-type, off-diagonal-type, and angle-type, parameters. We use $N_s = 974$ and $N_s = 980$ samples to compute the DGSMs for A_{122} and A_{212} respectively. There are 28 non-influential parameters for A_{122} and 27 non-influential parameters for A_{212} . In this instance, the QoIs shared all the same non-influential parameters except one parameter corresponding to bond over-coordination energy. This difference could be a consequence of the structure of the compound.

For the QoIs A_{121} and A_{112} we have $N_p = 110$ parameters. We compute the DGSM values with $N_s = 988$ and $N_s = 984$ samples for A_{121} and A_{112} , respectively. The results are used to determine there are 31 non-influential parameters for A_{121} and 32 non-influential parameters for A_{112} . Similar to the previous mixed atom angular bending energy, this difference may be a consequence of the atomic structure.

5.4 Conclusions

A global sensitivity approach was utilized to identify non-influential parameters of the reactive potentials used by ReaxFF. We focused on energetic interactions between Si and O, and calculated DGSM values for single atom energy, radial bond energy, and angle bending energy, for a variety of atom combinations. The computed sensitivity measures indicated that several of input parameters are insignificant in this material system. This information could be used to inform the user of parameters that are non-influential during the optimization process for Si-based glass ReaxFF input parameters.

With respect to the parameter space, we made several simplifying assumptions, including parameter independence. Also, the parameter intervals were determined experimentally. Future efforts to better map out the parameter space and relationships between parameters is needed. Future work could also include comparing results for elements in similar periodic categories and compounds with similar structures in order to look for trends.

We observed DGSM values equal to zero for many parameters. In future studies, a nonzero importance threshold could be enforced on the DGSM values to reduce the input dimension to a size for which more informative, but computationally expensive GSA tools, can be applied. Once the input dimension is reduced, the accuracy of the reduced simulations can be evaluated by comparing to simulations computed in the full parameters space. Additionally, input parameter dimension reduction informs which parameters need precise estimation for different QoIs to achieve an accurate parameterization.

STRUCTURE EXPLOITING METHODS FOR FAST UNCERTAINTY QUANTIFICATION IN MULTIPHASE FLOW THROUGH HETEROGENEOUS MEDIA

The contents of this chapter is related to the research contained in [26]. The author of the present thesis is also lead author on this manuscript. We would like to give special thanks to our collaborator Bilal Saad.

6.1 Introduction

Low permeability argillites are considered as suitable host rocks for underground radioactive waste storage to retain radionuclides locally. However, hydrogen gas produced by corrosion of steel engineered barriers can represent a threat to the installation safety. A significant impact of this production is the overpressurization of hydrogen around alveolus leading to opening fractures in the surrounding host rock and inducing groundwater flow and transport of radionuclides outside of the geological repositories. This problem renews the mathematical interest in the equations describing multiphase multicomponent flows through porous media, within the present context. An important aspect of improving the prediction fidelity of such models is to account for the various sources of uncertainty in the governing equations.

Performing uncertainty analysis on the models under study using a direct Monte Carlo sampling approach is infeasible. This is due to the high cost of model simulations and the need for a large number of such simulations. Therefore, there is a need for quick-to-evaluate surrogate models that accurately capture the underlying physics and statistical properties of the quantities of interest (QoIs). Surrogate modeling, however, is a formidable task for the applications considered in the present work. Models describing flow through porous media

exhibit distinct challenges with regards to uncertainty quantification including expensive simulations, high-dimensional uncertain parameters, and function-valued outputs. Addressing these challenges effectively requires understanding and exploiting the problem structure. To this end, we propose a framework that deploys a sensitivity analysis approach to reduce the dimensionality of the input parameter and utilizes the spectral properties of the output QoI to generate an efficient surrogate model.

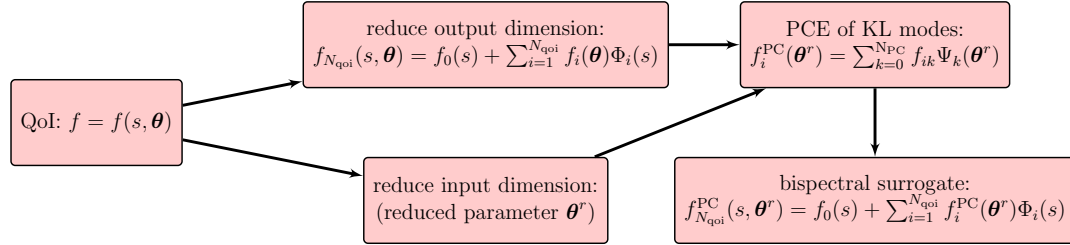


Figure 6.1 A schematic of the proposed *bispectral* surrogate modeling approach.

Related work. The modeling of underground radioactive waste storage involves simulating the coupled transport of multiphase multicomponent flow in porous medium. Equations governing this type of flow in porous media are nonlinear and involve simulation of complex phenomena such as the appearance and the disappearance of the gas phase leading to the degeneracy of the equations satisfied by the saturation. There have been significant research efforts dealing with mathematical and numerical models for simulating the transport migration of radionuclides. The articles [18, 19] present test-cases and set up benchmark examples to address some of the specific problems encountered when numerically simulating gas migration in underground nuclear waste repositories. In [8, 19, 76] different choices of primary variables have been proposed to tackle the degeneracy of the equations satisfied by the saturation. In [10], the authors study a two compressible and partially miscible phase flow model in porous media, applied to gas migration in an underground nuclear waste repository in the case where the velocity of the mass exchange between dissolved hydrogen and hydrogen in the gas phase is supposed finite. Also presented is a numerical scheme based on a two-step convection/diffusion-relaxation strategy to simulate the non-equilibrium model. There have also been efforts to quantify uncertainty in models of multiphase flow [22, 73, 74, 86, 97, 109].

The tools from uncertainty quantification that are relevant to the present work include global sensitivity analysis (GSA) and surrogate modeling. GSA provides insight into how uncertainties in model parameters influence model outputs by identifying the input parameters a QoI is sensitive to. This increases overall understanding of the underlying physics and guides parameter dimension reduction. The Sobol' indices [100], derivative-based global sensitivity measures (DGSMs) [57, 59, 101], and active subspace methods [27, 28] are examples of GSA tools widely used in practice. These concepts were originally conceived for scalar QoIs.

Recent works such as [6, 25, 114] generalize standard GSA tools to the case of vector- and function-valued QoIs. In particular, [6, 41] concern variance-based GSA using Sobol’ indices for such QoIs. The article [25] studies DGSMs for function-valued QoIs. A generalization of active subspace methods for vectorial outputs is presented in [114].

For expensive-to-compute QoIs calculating GSA measures such as Sobol’ indices is computationally expensive. A common method for mitigating the computational cost is to construct a cheap-to-evaluate surrogate model for the QoI and then apply GSA techniques to the surrogate. For example, polynomial chaos expansions (PCEs) have been a popular approach for accelerating the computation of Sobol’ indices; see, e.g., [4, 15, 31, 104]. Surrogate model construction, however, is itself a computationally challenging task, especially in the case of models with high-dimensional input parameters. For such models it is also possible to use a multilevel approach: initial parameter screening can be performed using cheap, but less precise, tools and further dimension reduction is performed through more rigorous methods such as a variance-based analysis using accurate surrogate models constructed in a reduced-dimensional parameter space; see e.g., [47].

For function-valued QoIs, a straightforward approach is to compute surrogate models for every grid point in a discretized computational domain. This approach, however, can be inefficient and ignores an important problem structure—the low-rank structure of the output. Specifically, in many applications, function-valued QoIs can be represented via a spectral representation, such as a Karhunen–Loève expansion (KLE), with a small number of terms. This problem structure can be exploited for surrogate modeling: instead of approximating a field quantity at every point in a computational grid, one can approximate a few dominant modes of the output QoI. Such surrogate models can also be used to accelerate GSA methods; see e.g., [6, 25, 45, 64].

Our approach and contributions. In the present work, we seek to construct surrogate models for fast analysis of computationally intensive models with high-dimensional parameters and function-valued QoIs. We consider QoIs of the form

$$f = f(s, \boldsymbol{\theta}), \quad s \in \mathcal{X}, \boldsymbol{\theta} \in \Theta,$$

where $\Theta \subseteq \mathbb{R}^{N_p}$ is the uncertain parameter domain and \mathcal{X} is compact subset of \mathbb{R}^d , with $d \in \{1, 2, 3\}$. In practice, s can represent a spatial or temporal point. Our focus in the present work is models of flow in porous media, and $f(s, \boldsymbol{\theta})$ is an observable in a multiphase flow problem. Our approach identifies and exploits low-dimensional structures in both input and output spaces. Specifically, we utilize approximate GSA measures for fast input parameter screening, and low-rank spectral representations of output fields.

We propose a fast-to-compute screening metric that utilizes ideas from active subspaces [27] to perform initial parameter dimension reduction. The proposed screening metrics do not require gradient computation in the parameter space. This makes the proposed methods applicable to a broad class of problems involving complex physics systems for which adjoint

solvers, which are essential for gradient computation in high dimensions, are not necessarily available. Following parameter screening, we combine two different spectral approaches—KLEs and PCEs—to generate an efficient surrogate model in a reduced-dimensional uncertain parameter space. The overall surrogate model constructed takes the form,

$$f_{N_{\text{qoi}}}^{\text{PC}}(s, \boldsymbol{\theta}^r) = f_0(s) + \sum_{i=1}^{N_{\text{qoi}}} f_i^{\text{PC}}(\boldsymbol{\theta}^r) \Phi_i(s),$$

where Φ_i 's are orthogonal basis functions in $L^2(\mathcal{X})$ obtained from a KLE of $f(s, \boldsymbol{\theta})$ and f_i^{PC} are approximate KL modes as functions of a reduced-dimensional parameter vector $\boldsymbol{\theta}^r \subseteq \mathbb{R}^{n_p}$; these KL modes are represented by PCEs,

$$f_i^{\text{PC}}(\boldsymbol{\theta}^r) = \sum_{k=0}^{N_{\text{PC}}} f_{ik} \Psi_k(\boldsymbol{\theta}^r),$$

where Ψ_k 's are a basis consisting of multivariate orthogonal polynomials in $L^2(\Theta)$ and N_{PC} is specified based on the choice of truncation strategy. Thus, the overall surrogate model can be expressed as

$$f(s, \boldsymbol{\theta}) \approx f_0(s) + \sum_{i=1}^{N_{\text{qoi}}} \sum_{k=0}^{N_{\text{PC}}} f_{ik} \Psi_k(\boldsymbol{\theta}^r) \Phi_i(s). \quad (6.1)$$

We refer to the class of surrogate models of the form (6.1) as *bispectral surrogates* due to the use of spectral representations in $L^2(\mathcal{X})$ and $L^2(\Theta)$. In Figure 6.1, we provide a schematic of the proposed bispectral surrogate modeling framework. We point out that the proposed approach is non-intrusive and requires only the ability to evaluate the governing model at a sample of uncertain inputs. See section 6.5 for details.

While computing a surrogate model from a truncated KLE by replacing the KL modes with PCEs (or other surrogates) is not new, see e.g., [6, 45, 64], we build upon this approach by including a gradient-free input dimension reduction approach as a first step. This enables the PCEs for the KL modes to be built in a lower-dimensional space. Thus, a major contribution of this chapter is a synergy of known techniques combined with a novel input dimension reduction strategy to furnish an integrated surrogate modeling approach. We also provide a detailed computational procedure for the proposed framework, making the present work a self-contained guide. We elaborate our approach on an intricate multiphase multicomponent flow model for which a comprehensive presentation is also given. In our numerical results, we implement the proposed approach for both spatially- and temporally-varying QoIs. Additionally, a variety of statistical studies are conducted with the constructed bispectral surrogate. These tests are intended to showcase the versatility of the surrogate model and explore the physical phenomenon under study. In particular, we perform model predictions, compute variance-based global sensitivity indices, and study statistical model response behavior. In addition to demonstrating the effectiveness of the proposed strategy, our computational re-

sults provide valuable insight regarding the response of complex porous media flow models to uncertainties in material properties.

Chapter overview. In section 6.2 we present a detailed overview of the multiphase multi-component flow model that is central to the present work. We also provide a description of our choice of numerical solver for the governing equations. In section 6.3, we discuss modeling the uncertainties in material properties, as well as give a brief explanation of the model response and relevant QoIs. We supply a concise overview of KLEs, PCEs, and bispectral surrogates in section 6.4. In section 6.5 we provide a detailed framework, including algorithms, for the proposed dimension reduction and surrogate modeling approach. Our computational results are presented in section 6.6. Finally, we provide closing comments in section 6.7.

6.2 Model description

6.2.1 Mathematical formulation of the continuous problem.

Here we state the physical model used in this work. We consider a porous medium saturated with a fluid composed of two phases, liquid (l) and gas (g), and a mixture of two components, water (w) and hydrogen (h). The spatial domain Ω a bounded open subset of \mathbb{R}^ℓ ($\ell = 1, 2$, or 3) and the problem is considered in the time interval $[0, T_f]$, where $T_f > 0$ is the final time. To define the physical model, we write the *mass conservation* of each component in each phase

$$\phi \partial_t (\rho_l^w S_l + \rho_g^w S_g) + \nabla \cdot (\rho_l^w \mathbf{V}_l + \rho_g^w \mathbf{V}_g + \mathbf{J}_l^w + \mathbf{J}_g^w) = f^w, \quad (6.2)$$

$$\phi \partial_t (\rho_l^h S_l + \rho_g^h S_g) + \nabla \cdot (\rho_l^h \mathbf{V}_l + \rho_g^h \mathbf{V}_g + \mathbf{J}_l^h + \mathbf{J}_g^h) = f^h, \quad (6.3)$$

where $\phi(x)$ is the given porosity of the medium, $S_\alpha(t, x)$ the saturation of the phase $\alpha \in \{l, g\}$, with the two saturations summing to one. Also, $p_\alpha(t, x)$ is the pressure of the phase α , ρ_α^β is the density of the component $\beta \in \{w, h\}$ in the phase α , and $\rho_\alpha = \rho_\alpha^h + \rho_\alpha^w$ is the density of the phase α . The velocity of each fluid, \mathbf{V}_α is given by Darcy's law

$$\mathbf{V}_\alpha = -\mathbf{K} \frac{k_{r_\alpha}(S_\alpha)}{\mu_\alpha} (\nabla p_\alpha - \rho_\alpha(p_\alpha) \mathbf{g}),$$

where $\mathbf{K}(x)$ is the intrinsic (given) permeability tensor of the porous medium, k_{r_α} the relative permeability of the α -phase, μ_α the constant α -phase's viscosity, p_α the α -phase's pressure, and \mathbf{g} , the gravity vector. For further details of the model we refer to the presentation of the benchmark [18, 19]. Following the Fick's law, the diffusive flux of a component β in the phase α is given by

$$\mathbf{J}_\alpha^\beta = -\phi S_\alpha \rho_\alpha D_\alpha^\beta \nabla \mathcal{X}_\alpha^\beta,$$

where coefficient D_α^β is the Darcy scale molecular diffusion coefficients of β -component in α -phase and $\mathcal{X}_\alpha^\beta = \rho_\alpha^\beta / \rho_\alpha$ is the component β molar fraction in phase α . Diffusive fluxes satisfy

$\sum_{\beta} J_{\alpha}^{\beta} = 0$ for each $\alpha \in \{l, g\}$.

The capillary pressure law, which links the jump of pressure of the two phases to the saturation, is

$$p_c(S_l) = p_g - p_l.$$

This function is decreasing ($\frac{dp_c}{dS_l}(S_l) < 0$ for all $S_l \in [0, 1]$), and satisfies $p_c(1) = 0$.

In the following, the water is supposed only present in the liquid phase (no vapor of water due to evaporation). Thus, (6.2)–(6.3) could be rewritten as

$$\phi \partial_t (S_l \rho_l^w) + \nabla \cdot (\rho_l^w \mathbf{V}_l) + \nabla \cdot (\phi S_l \rho_l D_l^h \nabla X_l^h) = f^w, \quad (6.4)$$

$$\phi \partial_t (S_l \rho_l^h + S_g \rho_g^h) + \nabla \cdot (\rho_l^h \mathbf{V}_l + \rho_g^h \mathbf{V}_g) - \nabla \cdot (\phi S_l \rho_l D_l^h \nabla X_l^h) = f^h. \quad (6.5)$$

The system (6.4)–(6.5) is not complete; to close the system, we use the ideal gas law and the Henry's law

$$\rho_g^h = \frac{M^h}{RT} p_g \quad \text{and} \quad \rho_l^h = M^h H^h p_g, \quad (6.6)$$

where the quantities M^h , H^h , R and T represent respectively the molar mass of hydrogen, the Henry's constant for hydrogen, the universal constant of perfect gases and T the temperature. By these formulation, the system (6.4)–(6.5) is closed and we choose the liquid pressure and the density of dissolved hydrogen as unknowns. From (6.6), the Henry's law combined to the ideal gas law, to obtain that the density of hydrogen gas is proportional to the density of hydrogen dissolved

$$\rho_g^h = C \rho_l^h \quad \text{where} \quad C = \frac{1}{H^h R T} = 52.51.$$

Note that the density of water ρ_l^w in the liquid phase is constant and from the Henry's law, we can write

$$\rho_l \nabla \mathcal{X}_l^h = \mathcal{X}_l^w \nabla \rho_l^h.$$

Then the system (6.4)–(6.5) can be written as

$$\phi \partial_t (S_l \rho_l^w) + \nabla \cdot (\rho_l^w \mathbf{V}_l) + \nabla \cdot (\phi S_l \mathcal{X}_l^w D_l^h \nabla \rho_l^h) = f^w, \quad (6.7)$$

$$\phi \partial_t (m(S_l) \rho_l^h) + \nabla \cdot (\rho_l^h \mathbf{V}_l + C \rho_l^h \mathbf{V}_g) - \nabla \cdot (\phi S_l \mathcal{X}_l^w D_l^h \nabla \rho_l^h) = f^h, \quad (6.8)$$

where $m(S_l) = S_l + C S_g$.

A van Genuchten-Mualem model with the parameters n , S_{ar} and p_r as given in Table

6.1 (left) is used for the relative permeabilities and capillary pressure:

$$\begin{aligned} p_c(S_{le}) &= p_r \left(S_{le}^{-1/v} - 1 \right)^{1/n}, \\ k_{rl}(S_{le}) &= \sqrt{S_{le}} \left(1 - \left(1 - S_{le}^{1/v} \right)^v \right)^2, \\ k_{rg}(S_{le}) &= \sqrt{1 - S_{le}} \left(1 - S_{le}^{1/v} \right)^{2v}, \end{aligned}$$

with the effective saturation

$$S_{le} = (S_l - S_{lr}) / (1 - S_{lr} - S_{gr}),$$

where S_{lr} and S_{gr} are the liquid and gas residual saturations, respectively, and $v = 1 - 1/n$.

6.2.2 Numerical solver

As is well known, the modeling of underground radioactive waste storage involves simulation of complex phenomena such as the appearance and the disappearance of the gas phase leading to the degeneracy of the equations satisfied by the saturation. This is mainly due to the migration of gas produced by the corrosion of nuclear waste packages within a complex heterogeneous domain. To overcome this difficulty, an important consideration, in the modelling of multiphase flow with mass exchange between phases, is the choice of the primary variables that define the thermodynamic state of the system. Different choices of primary variables have been proposed [8, 19, 76]. In this chapter, we consider pressure of the liquid phase and density of dissolved hydrogen the primary unknowns in the multiphase flow system.

A cell-centered finite volume scheme is used for the space discretization and an implicit Euler scheme for the temporal discretization. The nonlinear system is solved with a fixed point method.

In the following section, we present the numerical results on a test case dedicated to solve and understand of the main numerical problems concerning gas phase appearance produced by injecting of hydrogen in a one-dimensional homogeneous porous domain fully saturated with water (inspired from the MoMaS benchmark on multiphase flow in porous media [18] for more details).

6.2.3 Numerical experiment

We consider a one-dimensional domain with the benchmark setup described in [18]. The spatial domain Ω is the interval $(0, L)$, with $L = 200$ meters, and the final simulation time is $T_f = 10^6$ years. The parameters for porous medium, fluid characteristics, and initial and boundary conditions are presented in [18] and summarized in Table 6.1.

Initial conditions are uniform over the whole domain with pure liquid water at fixed

Table 6.1 Left: parameter values for the porous medium and fluid characteristics used in test case 1. Right: parameter values for domain size, boundary and initial conditions, total injection time and total simulation time.

<i>Parameter</i>	<i>Value</i>
ϕ [-]	0.15
\mathbf{K} [m^2]	5×10^{-20}
p_r [Pa]	2×10^6
n [-]	1.54
S_{lr} [-]	0.4
S_{gr} [-]	0
ρ_l^w [$\text{Kg} \cdot \text{mol}^{-3}$]	10^3
μ_l [$\text{Pa} \cdot \text{s}$]	1×10^{-3}
μ_g [$\text{Pa} \cdot \text{s}$]	9×10^{-6}
H^h [$\text{mol} \cdot \text{Pa}^{-1} \cdot \text{m}^{-3}$]	7.65×10^{-6}
M^h [$\text{Kg} \cdot \text{mol}^{-1}$]	2×10^{-3}
D_l^h [$\text{m}^2 \cdot \text{s}^{-1}$]	3×10^{-9}

<i>Parameter</i>	<i>Value</i>
L [m]	200
q_h [$\text{kg}/\text{m}^2/\text{year}$]	5.57×10^{-6}
p_{init} [Pa]	10^6
T_{inj} [years]	5×10^5
T_f [years]	10^6

liquid pressure and no hydrogen present,

$$p_l(0, x) = p_{init} \quad \text{and} \quad \rho_l^h(0, x) = 0, \quad x \in \Omega.$$

For boundary conditions, a constant flux of hydrogen and zero water flow rate were imposed on the left boundary

$$\begin{aligned} \rho_l^w V V_l - J_l^h &= 0, \\ \rho_l^h V V_l + \rho_g^h V V_g + J_l^h &= \begin{cases} q_h & 0 \leq t \leq T_{inj}, \\ 0 & t > T_{inj}. \end{cases} \end{aligned}$$

On the right boundary, Dirichlet boundary conditions the same as the initial conditions are imposed.

To validate our solver we ran simulations with the nominal parameters, and report the phase pressures and gas saturation at the inflow boundary. Our results are consistent with those reported in [8, 19, 76]. Figure 6.2 shows the gas saturation (left) and the phase pressures (right), with respect to time (years) during and after injection. For $0 < t < 13 \times 10^3$ years, the gas saturation remains zero, all injected hydrogen dissolves into the liquid phase, the whole domain is saturated with water, and the liquid pressure remains constant. At $t \approx 13 \times 10^3$ years, the maximum solubility is reached and the gas phase start to appears at the injection boundary. Gas saturation keeps growing along the period of hydrogen injection. When injection stops at $t = 5 \times 10^5$ years, gas saturation starts decreasing until it disappears. A negative water flux is observed (see Figure 6.3) as water comes from right to left to fill in

the empty space. At the end of the simulation, the gas pressure keeps decreasing and the liquid pressure gradient goes to zero, as the system reaches a steady state.

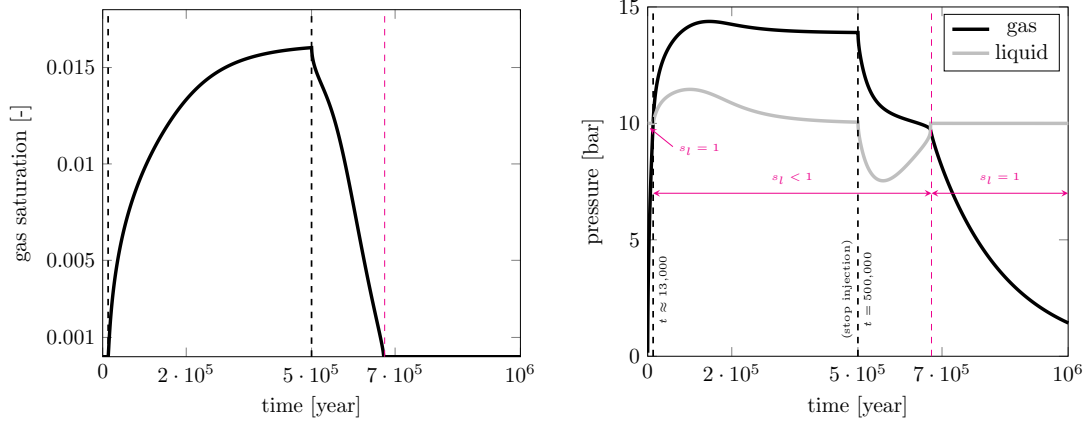


Figure 6.2 Gas saturation (left) and liquid and gas pressures (right) at the inflow boundary.

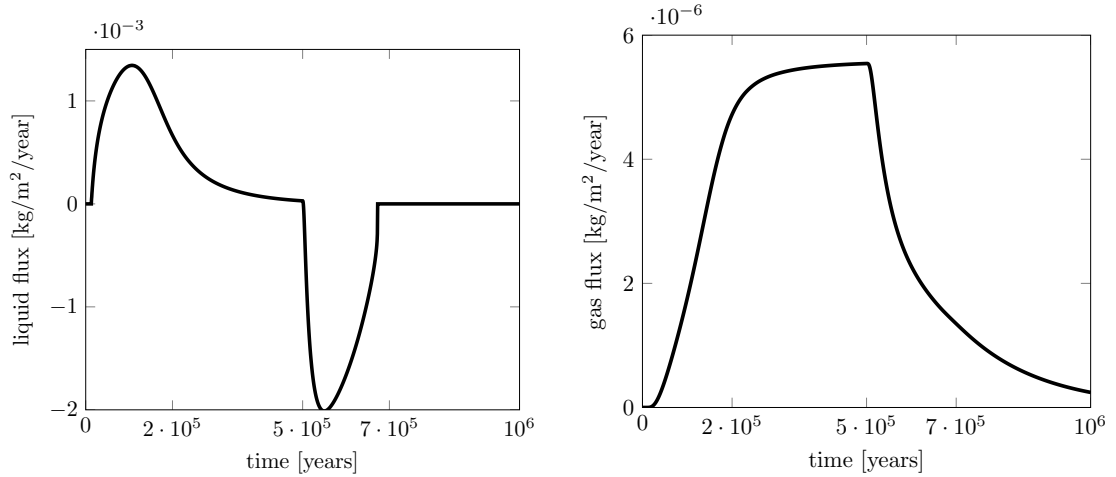


Figure 6.3 Liquid (left) and gas (right) flux at the outflow boundary.

6.3 Modeling under uncertainty

We seek to understand the impact of uncertainty in heterogeneous material properties on model predictions. Specifically, we focus on uncertainties in porosity and absolute permeability. Our goal is to understand the impact of uncertainties in material properties on the gas phase appearance/disappearance in a two phase flow produced by hydrogen injection

through a porous medium, which is initially fully saturated with water.

6.3.1 Modeling uncertainty in material properties

While in the setup of the benchmark problem constant values for porosity and permeability were used, allowing for spatially varying porosity and permeability provides a more realistic representation. This leads to representation of these quantities as random fields.

We model the porosity, ϕ , as a random field as follows. Let $Z(x, \omega)$ be a Gaussian process, with exponential covariance function $c(x, y) = e^{-|x-y|/\ell}$, where $\ell > 0$ is the correlation length. We chose $\ell = 10$ m (recall the length of the domain is 200 m). The covariance operator of Z is defined by

$$[\mathcal{C}_{\text{par}}u](x) = \int_{\Omega} c(x, y)u(y) dy, \quad u \in L^2(\Omega). \quad (6.9)$$

We define the random porosity field by

$$\phi(x, \omega) = F_B^{-1}(F_G(Z(x, \omega)); \alpha_{\text{beta}}, \beta_{\text{beta}}). \quad (6.10)$$

Here $F_B^{-1}(\cdot; \alpha_{\text{beta}}, \beta_{\text{beta}})$ is the inverse CDF of a $\text{Beta}(\alpha_{\text{beta}}, \beta_{\text{beta}})$ distribution and F_G is the CDF of a standard normal distribution. This ensures that for every $x \in \Omega$ the porosity is distributed according to $\text{Beta}(\alpha_{\text{beta}}, \beta_{\text{beta}})$. The random permeability field is obtained using a Kozeny–Carman relation [30, 65]:

$$K(\phi) \propto \frac{\phi^3}{(1 - \phi)^2}.$$

We set the proportionality constant in the above relation so that $K(\bar{\phi}) = \bar{K}$, where $\bar{\phi}$ and \bar{K} are the nominal porosity and permeability values listed in Table 6.1 (left). The values of α_{beta} and β_{beta} in (6.10) are set such that the mode of the porosity distribution (at each $x \in \Omega$) is the nominal porosity of $\bar{\phi} = 0.15$. Specifically, we chose $\alpha_{\text{beta}} = 20$ and found β_{beta} from the formula for the mode of a Beta distribution: $(\alpha_{\text{beta}} - 1)/(\alpha_{\text{beta}} + \beta_{\text{beta}} - 2) = \bar{\phi}$. We depict the distributions for pointwise porosity and permeability values along with the porosity permeability relation in Figure 6.4 (left). We note that the present setup provides a physically meaningful range of values for porosity and permeability, for the application problem under study.

To facilitate uncertainty quantification, we consider a truncated KLE of the Gaussian random field $Z(x, \omega)$ used in definition of $\phi(x, \omega)$ in (6.10). That is, we consider

$$Z(x, \omega) \approx \sum_{i=1}^{N_p} \sqrt{\lambda_i} \theta_i e_i(x), \quad (6.11)$$

where (λ_i, e_i) , $i = 1, \dots, N_p$ are the eigenpairs of the covariance operator of $Z(x, \omega)$; see e.g., [7, 13, 63] for details about the use of KL expansions for representing random fields in mathe-

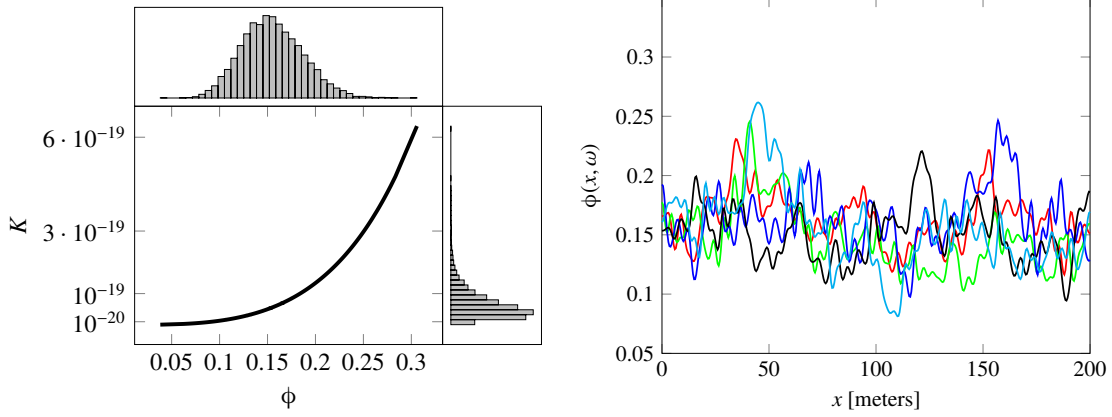


Figure 6.4 Left: the porosity permeability relation and the distributions of pointwise porosity and permeability. Right: a few realizations of the porosity field.

mathematical models. For the present problem, we let $N_p = 100$, which enables capturing over 96 percent of the average variance of the process. Notice that with the present setup, the uncertainty in the porosity field is fully captured by the vector $\boldsymbol{\theta} = [\theta_1 \ \theta_2 \ \dots \ \theta_{N_p}]^T$, where θ_i 's are the KLE coefficients in (6.11). As an illustration, we show a few realizations of the random porosity field in Figure 6.4 (right).

6.3.2 The QoIs under study

We focus on dynamics of hydrogen in gas phase by focusing on time evolution of gas saturation and pressure at the inflow boundary and gas flux at the outflow boundary. The units for gas pressure and gas flux are [bar] and [kg/m²/year], respectively. These time-dependent QoIs are indeed random field quantities due to randomness in porosity and permeability fields. Notice that since the uncertainty in porosity field is encoded in the coefficients $\boldsymbol{\theta}$ in (6.11), the randomness in these QoIs is also parameterized by the vector $\boldsymbol{\theta}$ of the KL coefficients. We denote the uncertain gas saturation at inflow boundary and gas flux at the outflow boundary by $S(t, \boldsymbol{\theta})$, and $Q(t, \boldsymbol{\theta})$, respectively. In Figure 6.5, we depict a few realizations of these uncertain QoIs.

We also consider the gas saturation throughout the domain, at various points in time. We denote this QoI by $S(x, \boldsymbol{\theta}; t^*)$, where t^* is a fixed time. Figure 6.6 (left) shows a few realizations of this QoI at $t^* = 300,091$ years. To further illustrate the impact of spatial heterogeneity on the flow model, we also report a plot of the gas saturation in the space-time domain in Figure 6.6 (right).

Performing statistical studies and predictions on the QoIs outlined above is challenging due to the high cost of solving the governing equations and the high-dimensionality of the input and output spaces. A major aim of this chapter is to present a surrogate modelling framework that approximates the time- or space-dependent QoIs efficiently by reducing the

input and output dimensions and using suitable approximations.

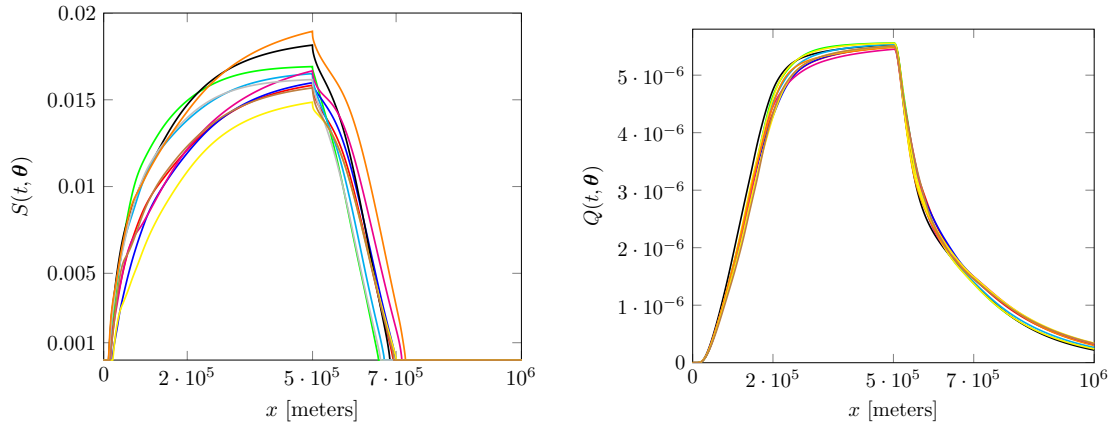


Figure 6.5 A few realizations of the time evolution of left: gas saturation at the inflow boundary, right: gas flux at the outflow boundary.

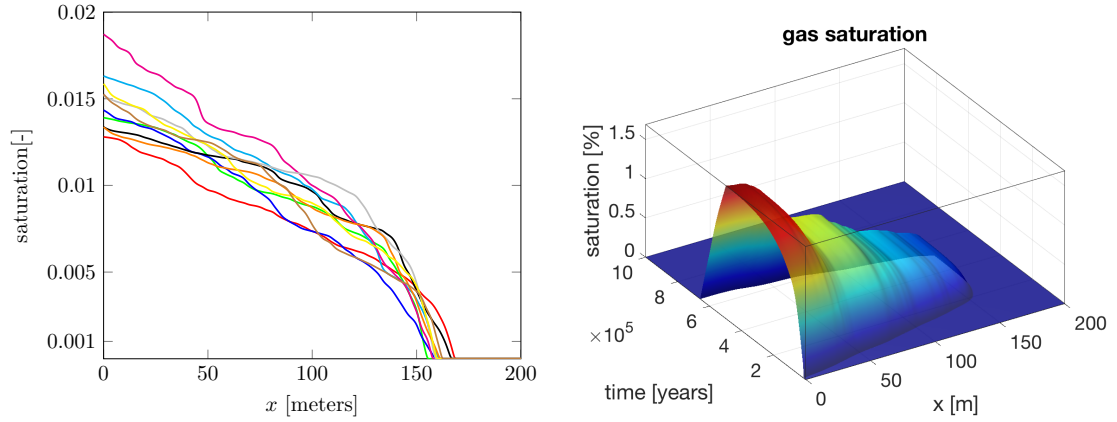


Figure 6.6 Left: gas saturation at $t^* = 300,091$ years, right: space time evolution of gas saturation.

6.4 Spectral representations of random processes

6.4.1 Karhunen Loève expansions

Here we briefly recall Karhunen Loève expansion (KLE) representation of a function-valued output $f(s, \theta)$. We assume f is a mean-square continuous random process. Such a processes

admits a KLE [63, 66] given as:

$$f(s, \boldsymbol{\theta}) = \bar{f}(s) + \sum_{i=1}^{\infty} \sqrt{\lambda_i} f_i(\boldsymbol{\theta}) \Phi_i(s). \quad (6.12)$$

Here $\bar{f}(s)$ is the mean of the process, (λ_i, Φ_i) are the eigenpairs of the covariance operator \mathcal{C}_{qoi} of the process, and $f_i(\boldsymbol{\theta})$ are the KL modes as defined in (2.8). An approximation $f_{N_{\text{qoi}}}(s, \boldsymbol{\theta})$ to $f(s, \boldsymbol{\theta})$ can be obtained by truncating (6.12) and retaining the first N_{qoi} terms in the series. In many physical and biological models the eigenvalues of \mathcal{C}_{qoi} decay rapidly. Consequently, such QoIs can be represented with sufficient accuracy by a truncated KLE with a small N_{qoi} . Such processes are referred to as “low-rank”.

Once again we rely on Nyström’s method to compute the KLE [56], using a sample average to approximate the covariance kernel. The steps for computing the truncated KLE of f are included in Algorithm 1.

Note that evaluating the truncated KLE of f requires computing the KL modes, which in turn requires a model evaluation. To convert the truncated KLE into an efficient surrogate model for f , we need a cheap-to-evaluate representation for the KL modes. This approach is similar to the one taken by [6, 64], in which PCE surrogates are constructed for the modes of the related spectral representations. In section 6.5, we modify this approach by first reducing the dimension of the input parameter and then constructing the KL modes surrogates in the reduced uncertain parameter space.

6.4.2 Polynomial chaos expansions for $f_i(\boldsymbol{\theta})$.

Recall, the polynomial chaos expansion of a square integrable function $g(\boldsymbol{\theta})$ is a series approximation of the form

$$g(\boldsymbol{\theta}) \approx \sum_{k=0}^{N_{\text{PC}}} c_k \Psi_k(\boldsymbol{\theta}), \quad (6.13)$$

where $\{\Psi_k\}_{k=0}^{N_{\text{PC}}}$ are a predetermined set of orthogonal polynomials, and $\{c_k\}_{k=0}^{N_{\text{PC}}}$ are the corresponding expansion coefficients [63]. Following a total order truncation [63], N_{PC} is given by

$$N_{\text{PC}} + 1 = \frac{(N_{\text{ord}} + N_{\text{p}})!}{N_{\text{ord}}! N_{\text{p}}!},$$

where N_{ord} is the maximum total polynomial degree and N_{p} is the dimension of $\boldsymbol{\theta}$. There are a variety of approaches for determining the expansion coefficients $\{c_k\}_{k=0}^{N_{\text{PC}}}$ including quadrature or regression based methods [63]. For this application, we implement sparse linear regression [37, 112]. In this method, the expansion coefficients are found by solving

$$\min_{\mathbf{c} \in \mathbb{R}^{N_{\text{PC}}}} \|\mathbf{\Lambda} \mathbf{c} - \mathbf{d}\|_2^2, \quad \text{subject to } \sum_{k=0}^{N_{\text{PC}}} |c_k| \leq \tau \quad (6.14)$$

where $\mathbf{\Lambda} \in \mathbb{R}^{N_s \times N_{PC}}$ is defined by $\Lambda_{ij} = \Psi_j(\boldsymbol{\theta}_i)$, $\mathbf{d} = (g(\boldsymbol{\theta}_1), g(\boldsymbol{\theta}_2), \dots, g(\boldsymbol{\theta}_{N_s}))^\top$ is a vector containing model evaluations, and τ is the sparsity control parameter. Determining N_{ord} and τ may be done with trial and error or with a cross-validation process, as detailed in section 6.6.

6.4.3 Bispectral surrogates

Earlier we broached the subject of utilizing PCEs to convert a truncated KLE into a surrogate model for f . Consider the truncated KLE of f ,

$$f_{N_{qoi}}(s, \boldsymbol{\theta}) = \bar{f}(s) + \sum_{i=1}^{N_{qoi}} \sqrt{\lambda_i} f_i(\boldsymbol{\theta}) \Phi_i(s). \quad (6.15)$$

By replacing the KL modes in (6.15) with PCEs we construct a surrogate model for f of the form

$$f_{N_{qoi}}^{PC}(s, \boldsymbol{\theta}) = \bar{f}(s) + \sum_{i=1}^{N_{qoi}} \sqrt{\lambda_i} f_i^{PC}(\boldsymbol{\theta}) \Phi_i(s), \quad (6.16)$$

where $f_i^{PC}(\boldsymbol{\theta})$ is the PCE for $f_i(\boldsymbol{\theta})$, $i = 1, \dots, N_{qoi}$. Once constructed, a bispectral surrogate can be used to characterize the statistical properties of the field QoI very efficiently.

To provide further insight, we also consider the approximation error for a bispectral surrogate.

Proposition 6.4.1. *Let $\|\cdot\|$ represent the L^2 norm on $\Theta \times \mathcal{X}$. The total error of the bispectral surrogate $f_{N_{qoi}}^{PC}$ can be bounded as follows:*

$$\begin{aligned} \|f - f_{N_{qoi}}^{PC}\|^2 &\leq \|f - f_{N_{qoi}}\|^2 + \|f_{N_{qoi}} - f_{N_{qoi}}^{PC}\|^2 = \\ &\sum_{i=N_{qoi}+1}^{\infty} \lambda_i + \sum_{i=1}^{N_{qoi}} \lambda_i \left[\sum_{k=0}^{N_{PC}} (c_{i,k} - \hat{c}_{i,k})^2 \|\Psi_k\|_{L^2(\Theta)}^2 \right] + \sum_{i=1}^{N_{qoi}} \lambda_i \left[\sum_{j=1+N_{PC}}^{\infty} c_{i,j}^2 \|\Psi_j\|_{L^2(\Theta)}^2 \right]. \end{aligned}$$

Proof. Consider the truncated KLE of f given by

$$f_{N_{qoi}}^{PC}(s, \boldsymbol{\theta}) = \bar{f}(s) + \sum_{i=1}^{N_{qoi}} \sqrt{\lambda_i} f_i^{PC}(\boldsymbol{\theta}) \Phi_i(s).$$

The total error in the product space is given by

$$\|f - f_{N_{qoi}}^{PC}\|^2 \leq \|f - f_{N_{qoi}}\|^2 + \|f_{N_{qoi}} - f_{N_{qoi}}^{PC}\|^2$$

We consider the first term

$$\|f - f_{N_{qoi}}\|^2$$

$$\begin{aligned}
&= \left\| \sum_{i=1}^{\infty} \sqrt{\lambda_i} f_i(\boldsymbol{\theta}) \Phi_i(s) - \sum_{i=1}^{N_{\text{qoi}}} \sqrt{\lambda_i} f_i(\boldsymbol{\theta}) \Phi_i(s) \right\|^2 \\
&= \int_{\Theta} \int_{\mathcal{X}} \left(\sum_{i=N_{\text{qoi}}+1}^{\infty} \sqrt{\lambda_i} f_i(\boldsymbol{\theta}) \Phi_i(s) \right)^2 ds \mu(d\boldsymbol{\theta}) \\
&= \sum_{i,j=N_{\text{qoi}}+1}^{\infty} \sqrt{\lambda_i} \sqrt{\lambda_j} \int_{\Theta} f_i(\boldsymbol{\theta}) f_j(\boldsymbol{\theta}) \int_{\mathcal{X}} \Phi_i(s) \Phi_j(s) ds \mu(d\boldsymbol{\theta}) \\
&= \sum_{i=N_{\text{qoi}}+1}^{\infty} \lambda_i \int_{\Theta} f_i(\boldsymbol{\theta})^2 \mu(d\boldsymbol{\theta}) = \sum_{i=N_{\text{qoi}}+1}^{\infty} \lambda_i.
\end{aligned}$$

Changing the order of infinite sums and integral is a consequence of the Dominated Convergence Theorem and reordering of integrals is justified by Fubini's Theorem. The orthogonality of the eigenfunctions in $L^2(\mathcal{X})$ justifies the simplification in the second to last line, and the last step is a consequence of the KL modes properties.

Next, we consider the second error term. Let

$$f_i^{\text{PC}} = \sum_{k=0}^{N_{\text{PC}}} \hat{c}_{i,k} \Psi_k(\boldsymbol{\theta}),$$

where $\hat{c}_{i,k}$ represents the numerical approximation of the exact PCE coefficients $c_{i,k}$ and recall, $f_i = \sum_{k=0}^{\infty} c_{i,k} \Psi_k(\boldsymbol{\theta})$ we have

$$\begin{aligned}
\|f_{N_{\text{qoi}}} - f_{N_{\text{qoi}}}^{\text{PC}}\|^2 &= \left\| \sum_{i=1}^{N_{\text{qoi}}} \sqrt{\lambda_i} f_i(\boldsymbol{\theta}) \Phi_i(s) - \sum_{i=1}^{N_{\text{qoi}}} \sqrt{\lambda_i} f_i^{\text{PC}}(\boldsymbol{\theta}) \Phi_i(s) \right\|^2 \\
&= \int_{\Theta} \int_{\mathcal{X}} \left(\sum_{i=1}^{N_{\text{qoi}}} \sqrt{\lambda_i} \Phi_i(s) [f_i(\boldsymbol{\theta}) - f_i^{\text{PC}}(\boldsymbol{\theta})] \right)^2 ds \mu(d\boldsymbol{\theta}) \\
&= \sum_{i,j=1}^{N_{\text{qoi}}} \sqrt{\lambda_i} \sqrt{\lambda_j} \int_{\Theta} (f_i - f_i^{\text{PC}})(f_j - f_j^{\text{PC}}) \int_{\mathcal{X}} \Phi_i(s) \Phi_j(s) ds \mu(d\boldsymbol{\theta}) \\
&= \sum_{i=1}^{N_{\text{qoi}}} \lambda_i \int_{\Theta} (f_i(\boldsymbol{\theta}) - f_i^{\text{PC}}(\boldsymbol{\theta}))^2 \mu(d\boldsymbol{\theta}) \\
&= \sum_{i=1}^{N_{\text{qoi}}} \lambda_i \int_{\Theta} \left(\sum_{k=0}^{\infty} c_{i,k} \Psi_k(\boldsymbol{\theta}) - \sum_{k=0}^{N_{\text{PC}}} \hat{c}_{i,k} \Psi_k(\boldsymbol{\theta}) \right)^2 \mu(d\boldsymbol{\theta}) \\
&= \sum_{i=1}^{N_{\text{qoi}}} \lambda_i \int_{\Theta} \left(\sum_{k=0}^{N_{\text{PC}}} (c_{i,k} - \hat{c}_{i,k}) \Psi_k(\boldsymbol{\theta}) + \sum_{k=1+N_{\text{PC}}}^{\infty} c_{i,k} \Psi_k(\boldsymbol{\theta}) \right)^2 \mu(d\boldsymbol{\theta}) \\
&= \sum_{i=1}^{N_{\text{qoi}}} \lambda_i \sum_{k=1}^{N_{\text{PC}}} (c_{i,k} - \hat{c}_{i,k})^2 \|\Psi_k\|_{L^2(\Theta)}^2 + \sum_{i=1}^{N_{\text{qoi}}} \lambda_i \sum_{j=1+N_{\text{PC}}}^{\infty} c_{i,j}^2 \|\Psi_j\|_{L^2(\Theta)}^2
\end{aligned}$$

The simplification in the third line is a consequence of the orthogonality of the PCE basis func-

tions.

Thus, we have a bound on the total error

$$\begin{aligned} \|f - f_{N_{\text{qoi}}}^{\text{PC}}\|^2 &\leq \|f - f_{N_{\text{qoi}}}\|^2 + \|f_{N_{\text{qoi}}} - f_{N_{\text{qoi}}}^{\text{PC}}\|^2 \\ &= \sum_{i=N_{\text{qoi}}+1}^{\infty} \lambda_i + \sum_{i=1}^{N_{\text{qoi}}} \lambda_i \sum_{k=1}^{N_{\text{PC}}} (c_{i,k} - \hat{c}_{i,k})^2 \|\Psi_k\|_{L^2(\Theta)}^2 + \sum_{i=1}^{N_{\text{qoi}}} \lambda_i \sum_{j=1+N_{\text{PC}}}^{\infty} c_{i,j}^2 \|\Psi_j\|_{L^2(\Theta)}^2. \quad \square \end{aligned} \quad (6.17)$$

■

The first term in the upper bound in (6.17) corresponds to KLE truncation error, the second term corresponds to error due to inexact PCE coefficients, and the third term corresponds to PCE truncation error. Controlling the total error involves a balance between computational cost, accuracy requirements, and the properties of the process. The KLE truncation error gets smaller as N_{qoi} increases. However, increasing the number of terms in the KLE increases the number of eigenpairs that need accurate approximations. Also, a larger N_{qoi} results in more KL modes, each of which requires a sufficiently accurate PCE. Similarly, the PCE error can be minimized by increasing the maximum polynomial degree, N_{ord} . However, this increases the total number of coefficients, which increases the number of unknowns in (6.13), resulting in increased computational cost.

The function-valued QoIs in the present work are low-rank processes with a high-dimensional input parameter. Therefore, a modest N_{qoi} will give a sufficiently small KLE truncation error. However, for large N_{p} , estimating the PCE coefficients for each KL mode with sufficient accuracy can become computationally expensive. Our approach for addressing this challenge is presented in the next section.

6.5 Method

In this section, we present our approach for reducing the dimensionality of the random vector $\boldsymbol{\theta} = [\theta_1 \ \theta_2 \ \dots \ \theta_{N_{\text{p}}}]^{\text{T}}$ and constructing a cheap-to-compute bispectral surrogate for function-valued QoIs under study. We begin by describing a screening procedure for input dimension reduction in section 6.5.1. Then, we discuss our surrogate modeling approach that uses a truncated KLE of the output (section 6.4.1) along with generalized PCEs for the output KL modes (section 6.5.2). We also show how the surrogate model can be used to efficiently compute the correlation function of the output, as well as cross-correlation of two function-valued QoIs.

6.5.1 Parameter screening

Consider a function-value QoI $f(s, \boldsymbol{\theta}) : \mathcal{X} \times \Theta \rightarrow \mathbb{R}$, where $\Theta \subseteq \mathbb{R}^{N_{\text{p}}}$ is the sample space of the uncertain parameters and $\mathcal{X} \subseteq \mathbb{R}^d$ is a compact set, which is the domain of an independent variable. The independent variable can be either time, in which case $d = 1$, or spatial

location in which case $d \in \{1, 2, 3\}$. Here we consider the case of $d = 1$, as it applies to our application problem, but the procedure below can be generalized to the case of $d \in \{2, 3\}$ in a straightforward manner.

Parameter screening can be done using functional derivative-based global sensitivity measures (DGSMs) given by [25]:

$$\mathfrak{N}_j(f) = \int_{\mathcal{X}} \int_{\Theta} \left(\frac{\partial f(s, \boldsymbol{\theta})}{\partial \theta_j} \right)^2 \mu(d\boldsymbol{\theta}) ds, \quad j = 1, \dots, N_p,$$

where μ is the law of the parameter vector $\boldsymbol{\theta}$. These DGSMs can be used to screen for “unimportant” inputs, which can be fixed at their respective nominal values. These functional DGSMs, however, require gradient evaluations. For complex models with high-dimensional parameters, such as the one considered in the present work, gradient computations is challenging. While adjoint-based gradient computation can overcome this, adjoint solvers are not always available for complex flow solvers and implementing them might be infeasible. Here we derive a screening indices based on ideas from active subspace methods [27] and activity scores [28] that approximate the functional DGSMs and circumvent gradient computation.

Let us briefly recall the concept of the active subspace and activity scores [28]. Fix $s \in \mathcal{X}$ and let $(\lambda_k, \mathbf{u}_k)$, $k = 1, \dots, N_p$ be the eigenpairs of the matrix

$$\mathbf{G} = \int_{\Theta} [\nabla f(s, \boldsymbol{\theta})][\nabla f(s, \boldsymbol{\theta})]^\top \mu(d\boldsymbol{\theta}), \quad (6.18)$$

where we assume the eigenvalues are sorted in descending order. In many cases there exists an M such that $\lambda_M \ll \lambda_{M+1}$, representing a gap in the eigenvalues. The *active subspace* corresponds to the subspace spanned by eigenvectors $\{\mathbf{u}_k\}_{k=1}^M$; this subspace captures the directions in the uncertain parameter space along which the QoI varies most. The case of a one-dimensional active subspace is surprisingly common [27]. The *activity scores* [28] utilize the active subspace structure to provide approximate screening indices, given by

$$\alpha_j[f(s, \cdot); M] = \sum_{k=1}^M \lambda_k \langle \mathbf{e}_j, \mathbf{u}_k \rangle^2, \quad j = 1, \dots, N_p, \quad M \leq N_p,$$

where $\langle \cdot, \cdot \rangle$ denotes the Euclidean inner product and \mathbf{e}_j is the j th coordinate vector in \mathbb{R}^{N_p} . One can use the activity scores to approximate functional DGSMs according to

$$\int_{\mathcal{X}} \alpha_j[f(s, \cdot); M] ds, \quad j = 1, \dots, N_p.$$

Note that with $M = N_p$, we recover the exact DGSMs [28]. Computing the activity scores still requires gradient computation, as seen in the definition of the matrix \mathbf{G} in (6.18). For cases where full model gradients are unavailable, [27] proposes constructing a linear model for $f(s, \boldsymbol{\theta})$ and using the gradient of the linear model to approximate the matrix \mathbf{G} . We build

on this idea to define a screening index for function-valued QoIs. First, we construct a global linear approximation \tilde{f} for the QoI

$$\tilde{f}(s, \boldsymbol{\theta}) = b_0(s) + \sum_{j=1}^{N_p} b_j(s) \theta_j. \quad (6.19)$$

Next, we use the activity scores for \tilde{f} as a “surrogate” for the scores of f . Note that $\nabla \tilde{f}(s, \boldsymbol{\theta}) = \mathbf{b}(s)$, where $\mathbf{b}(s) = [b_1(s) \ b_2(s) \ \cdots \ b_{N_p}(s)]^\top$. The matrix $\mathbf{G}(s)$ in (6.18), using \tilde{f} in place of f then simplifies to $\mathbf{G}(s) = \mathbf{b}(s)\mathbf{b}(s)^\top$. This rank one matrix can be written as

$$\mathbf{G}(s) = \lambda \mathbf{u}(s) \mathbf{u}(s)^\top,$$

where $\lambda = \|\mathbf{b}(s)\|_2^2$, and $\mathbf{u}(s) = \mathbf{b}(s) / \|\mathbf{b}(s)\|_2$. (Here $\|\cdot\|_2$ denotes the Euclidean vector norm.) Hence, the corresponding active subspace for \tilde{f} is 1-dimensional resulting in activity scores

$$\tilde{\alpha}_j(s) = b_j^2(s), \quad j = 1, \dots, N_p.$$

This gives rise to the following approximate functional DGSMs:

$$\mathfrak{N}_j(f) := \int_{\mathcal{X}} b_j^2(s) ds.$$

This relationship motivates the following normalized screening indices

$$s_j = \frac{\mathfrak{N}_j(f)}{\sum_{l=1}^{N_p} \mathfrak{N}_l(f)}, \quad j = 1, \dots, N_p.$$

Henceforth, we refer to s_j as the *screening index* of f with respect to parameters θ_j .

The purpose of the screening indices s_j is to inform input parameter dimension reduction. Let K_r be an ordered index set with cardinality $n_p < N_p$, corresponding to parameters with a screening index above some user-chosen tolerance $tol \in (0, 1)$. We denote the reduced input parameter vectors $\boldsymbol{\theta}^r$, where each component θ_i^r , $i = 1, \dots, n_p$ corresponds to the i th element of K_r .

Next, we discuss the computation of the global linear model for f . This is done by computing a linear model at each point $s \in \mathcal{X}$, which can be done efficiently using linear regression. Recall that \mathcal{X} is assumed to be a (compact) subset of \mathbb{R} (i.e., in one space dimension). Specifically, we assume $\mathcal{X} = [s_0, s_F]$. We discretize \mathcal{X} using a grid

$$s_0 = s_1 < s_2 < s_3 < \cdots < s_m = s_F.$$

Denote $\bar{\mathbf{b}}(s) = [b_0(s) \ b_1(s) \ b_2(s) \ \cdots \ b_{N_p}(s)]^\top$, with b_j , $j = 0, \dots, N_p$ as in (6.19). We require a set of model evaluations,

$$y_k^i = f(s_k, \boldsymbol{\theta}_i), \quad i = 1, \dots, N_s.$$

The number of samples required depends on computational budget as well as the application problem under study. We show in our numerical results that a modest N_s is adequate for the proposed approach, and the application problem considered herein.

Let $\mathbf{y}_k = [y_k^1 \ y_k^2 \ \dots \ y_k^{N_s}]^T \in \mathbb{R}^{N_s}$, and define the matrix

$$\mathbf{A} = \begin{bmatrix} 1 & \boldsymbol{\theta}_1^T \\ 1 & \boldsymbol{\theta}_2^T \\ 1 & \boldsymbol{\theta}_3^T \\ \vdots & \vdots \\ 1 & \boldsymbol{\theta}_{N_s}^T \end{bmatrix}. \quad (6.20)$$

The vectors $\bar{\mathbf{b}}(s_k)$ can be computed numerically by solving linear least squares problems

$$\bar{\mathbf{b}}(s_k) = \arg \min_{\mathbf{b} \in \mathbb{R}^{N_s+1}} \|\mathbf{A}\mathbf{b} - \mathbf{y}_k\|_2^2, \quad (6.21)$$

for $k = 1, \dots, m$. Note that here we assume \mathbf{A} has full column rank and we are in the over-terminated case, i.e. $N_s > N_p + 1$. Under these assumptions, the QR factorization $\mathbf{A} = \mathbf{Q}\mathbf{R}$ may be used to solve the linear regression problem in (6.21) by

$$\bar{\mathbf{b}}(s_k) = \mathbf{R}^{-1}\mathbf{Q}^T\mathbf{y}_k.$$

Then, for each $k = 1, \dots, m$, the cost of computing $\bar{\mathbf{b}}_k$ is one matrix-vector product with \mathbf{Q}^T and one triangular solve. The procedure for computing the global linear model is summarized in Algorithm 3. In the case where the dimension of $\boldsymbol{\theta}$ is larger than the number of available function evaluations, i.e. $N_s < N_p + 1$, other methods for solving the linear regression in Equation (6.21), e.g. using SVD, can be used.

6.5.2 Polynomial chaos surrogates for KL modes

To form a surrogate model, we construct a PC surrogate $f_i^{\text{PC}}(\boldsymbol{\theta}^r), i = 1, \dots, N_{\text{qoi}}$ in the *reduced* parameter space. Explicitly, we have the following training data for the KL mode surrogates: the input parameter samples $W = \{\boldsymbol{\theta}_j^r\}_{j=1}^{N_s}$ and, for each KL mode $f_i, i = 1, \dots, N_{\text{qoi}}$, we have the evaluations $F_i = \{f_i(\boldsymbol{\theta}_j)\}_{j=1}^{N_s}$. For each KL mode f_i , we use the corresponding training data to solve the optimization problem (6.14) for the coefficients \mathbf{c} ; see Algorithm 4 for more details. Observe that each input parameter sample $\boldsymbol{\theta}_j^r$ is the reduced version of the original input parameter sample, whereas the data points in F_i correspond to the KL mode f_i evaluated on the full parameter $\boldsymbol{\theta}_j$. Utilizing the data this way has two benefits. Firstly, we do not require more model evaluations. Secondly, the KL modes corresponding to the exact QoI capture the behavior of f more accurately than the KL modes corresponding to an f re-evaluated in the reduced parameter space. After the PCE for each KL mode is computed, we replace each $f_i(\boldsymbol{\theta})$

Algorithm 3 Computing the screening indices $s_j, j = 1, \dots, N_p$: the overdetermined case.

Input: Function evaluations $y_k^i = f(s_k, \theta_i), i = 1, \dots, N_s, k = 1, \dots, m$; quadrature weights $w_k, k = 1, \dots, m$.

Output: Sensitivity measures $s_j, j = 1, \dots, N_p$.

- 1: Form the matrix \mathbf{A} in (6.20) and compute its QR factorization, $\mathbf{A} = \mathbf{Q}\mathbf{R}$.
 - 2: **for** $k = 1$ to m **do**
 - 3: Compute $\mathbf{z}_k = \mathbf{Q}^\top \mathbf{y}_k$.
 - 4: Solve $\mathbf{R}\bar{\mathbf{b}}(s_k) = \mathbf{z}_k$.
 - 5: **end for**
 - 6: **for** $j = 1$ to N_p **do**
 - 7: Compute $\mathfrak{N}_j = \sum_{k=1}^{N_p} w_k b_j(s_k)^2$.
 - 8: **end for**
 - 9: **for** $j = 1$ to N_p **do**
 - 10: Compute $s_j = \mathfrak{N}_j / (\sum_k \mathfrak{N}_k)$.
 - 11: **end for**
-

in the KL expansion (2.6) with the corresponding f_i^{PC} to form a (reduced space) bispectral surrogate for f :

$$f(t, \boldsymbol{\theta}) \approx f_{N_{\text{qoi}}}^{\text{PC}}(t, \boldsymbol{\theta}^r) = \hat{f}(t) + \sum_{i=1}^{N_{\text{qoi}}} \sqrt{\lambda_i} f_i^{\text{PC}}(\boldsymbol{\theta}^r) \Phi_i(t). \quad (6.22)$$

In section 6.6 we demonstrate the proposed approach for dimension reduction and surrogate modeling for temporally varying QoI $S(t, \boldsymbol{\theta})$ and $Q(t, \boldsymbol{\theta})$, as well as spatially varying QoI $S(x, \boldsymbol{\theta})$.

Bispectral surrogates of the form (6.22) can be sampled efficiently to study the statistical properties of the QoI. As seen below, such surrogates can also be used to efficiently compute the correlation structure of function-valued outputs.

6.5.3 Correlation structure of the output

Let $f : \mathcal{X} \times \Theta \rightarrow \mathbb{R}$ be a random process with mean $\bar{f}(s)$ and assume f admits a surrogate $f_{N_{\text{qoi}}}^{\text{PC}}$ of the form in (6.22). It is straightforward to show that the covariance operator of $f_{N_{\text{qoi}}}^{\text{PC}}$ satisfies

$$\begin{aligned} c_f(s_1, s_2) &= \text{Cov}\{f_{N_{\text{qoi}}}^{\text{PC}}(s_1, \cdot), f_{N_{\text{qoi}}}^{\text{PC}}(s_2, \cdot)\} \\ &= \sum_{i=1}^{N_{\text{qoi}}} \sum_{j=1}^{N_{\text{qoi}}} \sum_{k=1}^{N_{\text{PC}}} \eta_i^k \eta_j^k \|\Psi_k\|_{L^2(\Theta)}^2 \Phi_i(s_1) \Phi_j(s_2), \end{aligned} \quad (6.23)$$

for $\eta_i^k = c_{i,k} \sqrt{\lambda_i}$ and $\|\cdot\|_{L^2(\Theta)}$ denotes the L^2 norm on Θ . Let us define

$$B_{ij} := \sum_{k=1}^m \eta_i^k \eta_j^k \|\Psi_k\|_{L^2(\Theta)}^2, \quad i, j = 1, \dots, N_{\text{qoi}},$$

Algorithm 4 Computing the surrogate model $f_{N_{\text{qoi}}}^{\text{PC}}$.

Input: Reduced input parameters $\boldsymbol{\theta}_j^r \in \mathbb{R}^{n_p}$, $j = 1, \dots, N_s$; KL mode evaluations $f_i^k = f_i(\boldsymbol{\theta}_j)$, $i = 1, \dots, N_{\text{qoi}}$, $j = 1, \dots, N_s$; highest polynomial degree N_{ord} ; sparsity parameter τ ; polynomial basis Ψ_k , $k = 1 \dots N_{\text{PC}}$.

Output: Surrogate model $f_{N_{\text{qoi}}}^{\text{PC}}(t, \boldsymbol{\theta}^r)$ and polynomial KL mode expansions $f_i^{\text{PC}}(\boldsymbol{\theta}^r)$, $i = 1, \dots, N_{\text{qoi}}$.

- 1: **for** $i = 1$ to N_{qoi} **do**
- 2: Let $\mathbf{d}_i = [f_i(\boldsymbol{\theta}_1), \dots, f_i(\boldsymbol{\theta}_{N_s})]$
 and $\boldsymbol{\Lambda}_{kj} = \Psi_k(\boldsymbol{\theta}_j^r)$.
- 3: Solve

$$\min_{\mathbf{c}_i \in \mathbb{R}^{N_{\text{PC}}}} \|\boldsymbol{\Lambda} \mathbf{c}_i - \mathbf{d}_i\|_2^2$$

- 4: **end for**
 - 5: Form $f_i(\boldsymbol{\theta}^r) = \sum_{k=1}^{N_{\text{PC}}} c_{i,k} \Psi_k(\boldsymbol{\theta}^r)$, $i = 1, \dots, N_{\text{qoi}}$.
 - 6: Form $f_{N_{\text{qoi}}}^{\text{PC}}(s, \boldsymbol{\theta}^r) = \sum_{k=1}^{N_{\text{qoi}}} \sqrt{\lambda_i(\mathbf{C})} f_i^{\text{PC}}(\boldsymbol{\theta}^r) \Phi_i(s)$.
-

and

$$\mathbf{p}(s) := [\Phi_1(s) \ \Phi_2(s) \ \dots \ \Phi_{N_{\text{qoi}}}(s)]^\top.$$

We can rewrite the expression in (6.23) as

$$c_f(s_1, s_2) = \langle \mathbf{p}(s_1), \mathbf{B} \mathbf{p}(s_2) \rangle,$$

where $\langle \cdot, \cdot \rangle$ denotes the Euclidean inner product. Using this, we can also obtain the *correlation function* of $f_{N_{\text{qoi}}}^{\text{PC}}$:

$$\rho_f(s_1, s_2) = \frac{c_f(s_1, s_2)}{\sqrt{c_f(s_1, s_1)} \sqrt{c_f(s_2, s_2)}}. \quad (6.24)$$

We can also compute the cross-covariance function of two random processes represented via bispectral surrogates. Consider a random process g approximated by the surrogate model

$$g_{M_{\text{qoi}}}^{\text{PC}} = \bar{g}(s) + \sum_{j=1}^{M_{\text{qoi}}} \sum_{k=0}^{M_{\text{PC}}} \sqrt{\gamma_j} d_{j,k} \Psi_k(\boldsymbol{\theta}^r) \tilde{\Phi}_j(s),$$

where M_{qoi} is the number of KL modes, $(\gamma_j, \tilde{\Phi}_j(s))$ are the eigenpairs corresponding to the covariance function of g , M_{PC} is the maximum polynomial degree, and $d_{i,k}$ are the PCE coefficients. A calculation similar to the one above gives the cross-covariance function of $f_{N_{\text{qoi}}}^{\text{PC}}$

and $g_{M_{\text{qoi}}}^{\text{PC}}$ as

$$c_{fg}(s_1, s_2) = \langle \mathbf{p}(s_1), \tilde{\mathbf{B}}\mathbf{q}(s_2) \rangle,$$

where

$$\begin{aligned} \mathbf{q}(s) &:= [\tilde{\Phi}_1(s) \ \tilde{\Phi}_2(s) \ \dots \ \tilde{\Phi}_{M_{\text{qoi}}}(s)]^T, \\ \tilde{B}_{i,j} &:= \sum_{k=1}^m \eta_i^k \tilde{\eta}_j^k \|\Psi_k\|_{L^2(\Theta)}^2, \quad i = 1, \dots, N_{\text{qoi}}, \ j = 1, \dots, M_{\text{qoi}}, \end{aligned}$$

with $\tilde{\eta}_j^k = d_{j,k} \sqrt{\gamma_j}$. We can also compute the cross-correlation function,

$$\rho_{fg}(s_1, s_2) = \frac{c_{fg}(s_1, s_2)}{\sqrt{c_f(s_1, s_1)} \sqrt{c_g(s_2, s_2)}}, \quad (6.25)$$

where c_g is the covariance function of $g_{M_{\text{qoi}}}^{\text{PC}}$.

6.6 Numerical results

In this section, we demonstrate the dimension reduction and surrogate modeling approach proposed in section 6.5 for temporally and spatially varying QoIs discussed in section 6.3. In section 6.6.1, we detail surrogate model construction for gas saturation at the inflow boundary. To provide further insight, we also consider surrogate modeling for gas flux at the outflow boundary in section 6.6.2 and for gas saturation across the spatial domain in section 6.6.3. Finally, in section 6.6.4, we use the surrogates constructed in section 6.6.1 and 6.6.2 to better understand the behavior and properties of the corresponding QoIs.

6.6.1 Gas saturation at the outflow boundary

Here we focus on gas saturation at the inflow boundary, i.e., $S(t, \boldsymbol{\theta})$. Recall that the input parameter $\boldsymbol{\theta}$ parameterizes the uncertainty in the porosity field, as described in section 6.3.1, and has dimension $N_p = 100$. For the present numerical study, we computed a database of 550 model evaluations, which we use for parameter screening and surrogate model construction.

Input parameter screening. We use Algorithm 3 with $N_s = 500$ full model evaluations to compute the screening indices s_j , $j = 1, 2, \dots, N_p$, for $S(t, \boldsymbol{\theta})$. The remaining 50 realizations were used for validation of the linear models computed as a part of the algorithm. In Figure 6.7 (left) and (middle), we report representative comparisons of the linear model versus the exact model, at the validation points at selected times. Note that the linear models capture the overall behavior of the model response. In Figure 6.7 (right), we report the screening indices that are above the importance threshold $tol = 0.002$. The parameters with screening indices below tol are considered unimportant. This reduces the input parameter dimension from $N_p = 100$ to $n_p = 10$ and the resulting reduced parameter is $\boldsymbol{\theta}^r = [\theta_1 \ \dots \ \theta_{10}]^T$.

Spectral representation of the QoI. Next, we compute the KLE of $S(t, \boldsymbol{\theta})$ using Algo-

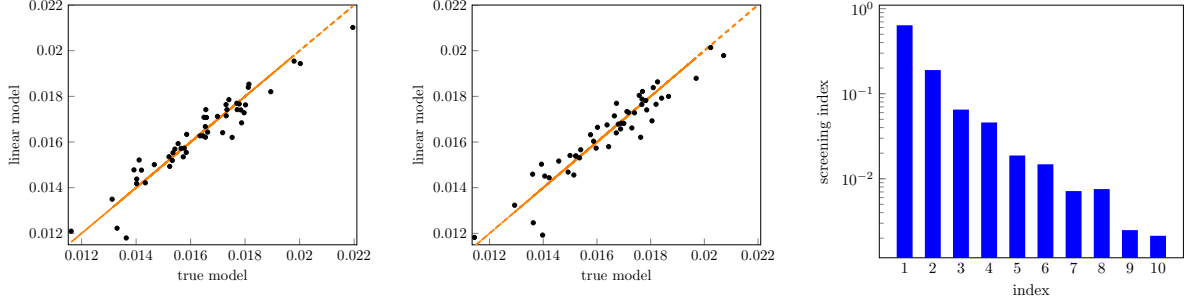


Figure 6.7 Fifty point comparison of the true model to the linear model for $S(t, \theta)$ at left: $t = 400,234$ years, middle: $t = 500,106$ years. Right: screening indices s_j for $S(t, \theta)$ calculated using Algorithm 3 with 500 full QoI samples. Scores above $tol = 0.002$ displayed only.

rithm 1. This requires solving the eigenvalue problem (2.7), with \mathcal{C}_{qoi} being the covariance operator of $S(t, \theta)$. We use a sample average approximation of \mathcal{C}_{qoi} with sample size $N_s \in \{100, 200, 350, 550\}$ exact QoI evaluations, as detailed in Algorithm 1. In Figure 6.8 (left), we show the computed (dominant) eigenvalues of \mathcal{C}_{qoi} . We note that the dominant eigenvalues are approximated well even with $N_s = 100$. We use the computations corresponding $N_s = 550$ in what follows. We note that the eigenvalues of the output covariance operator decay rapidly. We also report r_k from equation (2.9) in Figure 6.8 (right). Recall, r_k represents the fraction of the average variance of f captured by the first k eigenvalues. We note that r_k exceeds 0.99 for $k \geq 5$. This indicates that $S(t, \theta)$ is a low-rank process and a KL expansion with $N_{\text{qoi}} = 5$ provides a suitable approximation of the QoI. Consequently, we consider the truncated KL expansion of $S(t, \theta)$

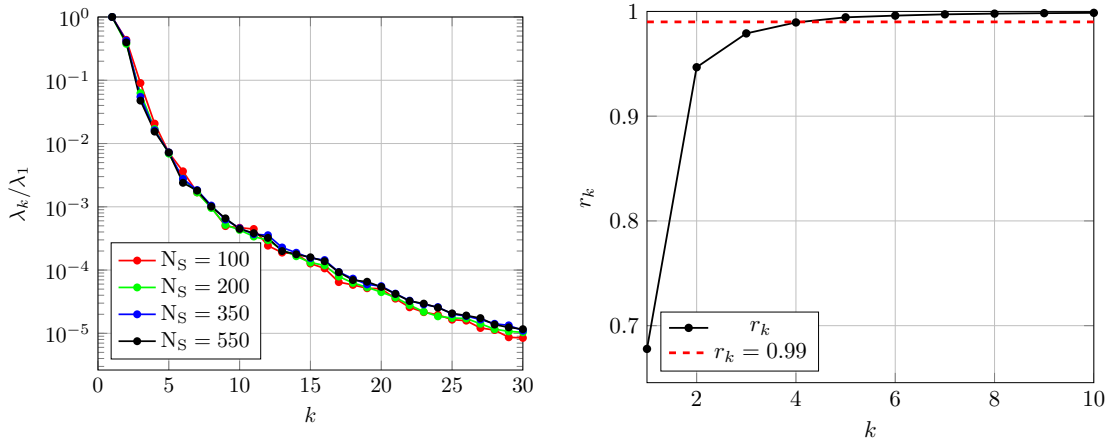


Figure 6.8 Left: comparison of ratio λ_k/λ_1 , $k = 1 \dots, 30$ for $\lambda_i(\mathcal{C}_{\text{qoi}})$ corresponding to $S(t, \theta)$ computed with various sample sizes, right: r_k as defined in (2.9), $k = 1, \dots, 10$, for $S(t, \theta)$. Dotted line corresponds to 0.99.

$$S_{N_{\text{qoi}}}(t, \boldsymbol{\theta}) = \bar{S}(t) + \sum_{i=1}^{N_{\text{qoi}}} \sqrt{\lambda_i(\mathcal{C}_{\text{qoi}})} S_i(\boldsymbol{\theta}) \Phi_i(t), \quad (6.26)$$

where $N_{\text{qoi}} = 5$. The next step is to compute PCEs for the KL modes $S_i(\boldsymbol{\theta})$, $i = 1, \dots, N_{\text{qoi}}$.

PCE surrogates of the KL modes. Next, we construct a bispectral surrogate for $S(t, \boldsymbol{\theta})$ which we denote $S_{N_{\text{qoi}}}^{\text{PC}}$. Recall that the components of $\boldsymbol{\theta}^r$ are sampled from a Gaussian distribution. Hence, we utilize the n_p -variate Hermite polynomials as the orthogonal basis for the PC expansions, with $n_p = 10$. We use the sparse-regression approach (see section 6.4.2) for computing PCEs of the output KL modes (see section 6.5.2). To determine suitable values for the maximum polynomial degree N_{ord} and the sparsity parameter τ , we use a 10-fold cross validation procedure, which we briefly explain next.

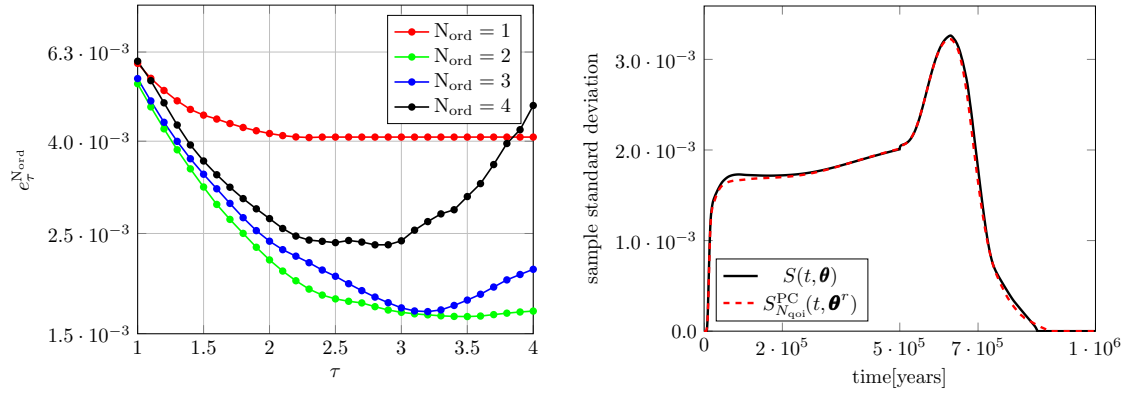


Figure 6.9 Left: cross validation results for $\tau = \{1, 1.1, \dots, 3.9, 4\}$ and $N_{\text{ord}} = \{1, 2, 3, 4\}$ for gas saturation, right: comparison of sample standard deviations of $S(t, \boldsymbol{\theta})$ and $S_{N_{\text{qoi}}}^{\text{PC}}(t, \boldsymbol{\theta}^r)$ computed on 200 sample points.

Note that for each evaluation of $S_{N_{\text{qoi}}}(t, \boldsymbol{\theta}_j)$, $j = 1, \dots, N_s$, there is a corresponding KL mode evaluation $S_i(\boldsymbol{\theta}_j)$, for $i = 1, \dots, N_{\text{qoi}}$. We separate the parameter samples into $W = \{\boldsymbol{\theta}_j^r\}_{j=1}^{350}$ and $\hat{W} = \{\boldsymbol{\theta}_j^r\}_{j=351}^{550}$. Similarly, for each $i = 1, \dots, N_{\text{qoi}}$, we have $F_i = \{S_i(\boldsymbol{\theta}_j)\}_{j=1}^{350}$ and $\hat{F}_i = \{S_i(\boldsymbol{\theta}_j)\}_{j=351}^{550}$.

We partition W and F_i , $i = 1, \dots, N_{\text{qoi}}$ 10 different ways, such that each data partition has a 35 point validation set and a 315 point training set. Let W^k and F_i^k , denote the k th such data partition, $k = 1, \dots, 10$. Next, for every combination of $N_{\text{ord}} \in \{1, \dots, 4\}$, $\tau \in \{1, 1.1, 1.2, \dots, 3.9, 4\}$, $k = 1, \dots, 10$, and $i = 1, \dots, N_{\text{qoi}}$ we solve the optimization problem (6.14); in our computations, we use the solver SPGL1 [12]. For the components of that data vector of \mathbf{d} in (6.14), we use the training set of F_i^k . Therefore, every combination of k , N_{ord} and τ results in a surrogate model denoted as $g_{N_{\text{ord}}, \tau}^k(s, \boldsymbol{\theta}^r)$.

To assess the accuracy of each bispectral surrogate we compute the average relative error

$$e_{\text{rel}}(g_{N_{\text{ord}},\tau}^k) = \left[\frac{\sum_{j=1}^M \int_{\mathcal{X}} [S(t, \theta_j) - g_{N_{\text{ord}},\tau}^k(s, \theta_j^r)]^2 ds}{\sum_{j=1}^M \int_{\mathcal{X}} S(t, \theta_j)^2 ds} \right]^{\frac{1}{2}}, \quad (6.27)$$

where $\mathcal{X} = [0, T_f]$, $M = 35$ and θ_j is the input parameter in the full space corresponding to θ_j^r in the validation set of W^k .

We repeat the process for each of the 10 partitions, and compute the average of e_{rel} across all partitions

$$e_{\tau}^{N_{\text{ord}}} = \frac{1}{10} \sum_{k=1}^{10} e_{\text{rel}}(g_{N_{\text{ord}},\tau}^k).$$

The cross validation errors corresponding to $S(t, \theta)$ are displayed in Figure 6.9 (left). The smallest $e_{\tau}^{N_{\text{ord}}}$ corresponds with $N_{\text{ord}} = 2$ and $\tau = 3.5$.

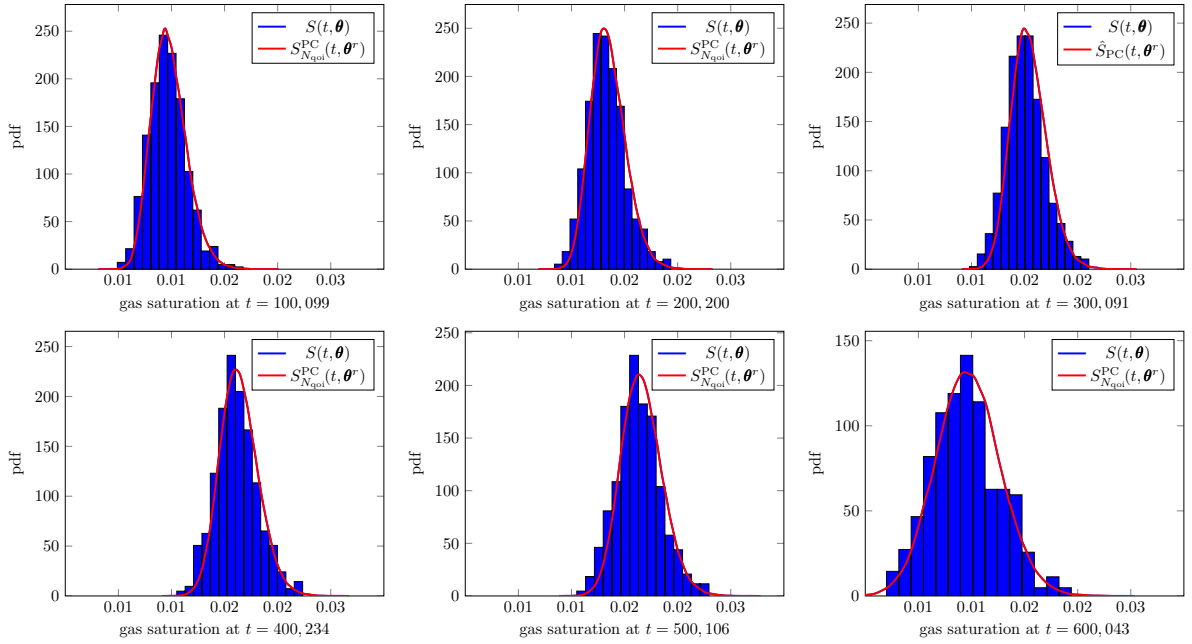


Figure 6.10 Comparison of normalized histograms for $S(t, \theta)$ and pdf estimates of the surrogate $S_{N_{\text{qoi}}}^{\text{PC}}(t, \theta^r)$ for a variety of times $t \in [0, T_f]$.

Computing the overall bispectral surrogate. Once we have determined appropriate values for N_{ord} and τ we follow Algorithm 4 to construct a surrogate model from the truncated KLE expansion of the function-valued QoI. To determine PCE for each KL mode $S_i(\theta)$, $i = 1, \dots, N_{\text{qoi}}$, we use the solver SPGL [12] to implement sparse linear regression over the entire 350 point data set F_i . We use the resulting expansions to form the overall bispectral

surrogate:

$$S_{N_{\text{qoi}}}^{\text{PC}} = \bar{S}(t) + \sum_{i=1}^{N_{\text{qoi}}} \sqrt{\lambda(\mathcal{C}_{\text{qoi}})} S_i^{\text{PC}}(\boldsymbol{\theta}^r) \Phi_i(t).$$

Note that in numerical computations, $\bar{S}(t)$ is the sample mean $\bar{S}(t) = \frac{1}{N_s} \sum_{j=1}^{N_s} S(t, \boldsymbol{\theta}_j)$.

Next, we assess the effectiveness of the bispectral surrogate to reflect the statistical properties of the true model. First, we compare the sample standard deviations of $S_{N_{\text{qoi}}}^{\text{PC}}(t, \boldsymbol{\theta}^r)$ and $S(t, \boldsymbol{\theta})$ computed over the testing set \hat{W} . The results are shown in Figure 6.9 (right). Note, the surrogate model does an excellent job capturing the behavior of $S(t, \boldsymbol{\theta})$. Then, we compute the pdf of $S_{N_{\text{qoi}}}^{\text{PC}}(t, \boldsymbol{\theta}^r)$ with 100,000 surrogate evaluations and compare with the normalized histograms of the 550 exact model evaluations. In Figure 6.10 clockwise from upper left we show the pdf estimates for a few representative simulation times. Note that pdf estimates closely match the distribution of the full model.

6.6.2 Gas flux at the outflow boundary

In this section, we study gas flux at the outflow boundary, denoted by $Q(t, \boldsymbol{\theta})$. A few realizations of $Q(t, \boldsymbol{\theta})$ are shown in Figure 6.5 (right). The global linear model is computed with 500 model realizations. A representation of the linear model at time $t = 500,106$ years is displayed in Figure 6.11 (left). Next, we compute the screening indices s_j . In Figure 6.11 (middle) we display s_j , $j = 1 \dots, 10$ above $\text{tol} = 0.02$ only. Therefore, dimension reduction results in the reduced input parameter $\boldsymbol{\theta}^r = [\theta_1 \dots \theta_{10}]^T$. Next, we compute the KLE and truncate at $N_{\text{qoi}} = 7$ terms. Then, we construct the surrogate model using the data sets W and F_i , where the F_i 's for this instance consist of the KL modes computed for $Q(t, \boldsymbol{\theta})$. We use the 10-fold cross validation technique described in section 6.6.1 to choose the sparse linear regression parameters $N_{\text{ord}} = 2$ and $\tau = 4$. Finally, we use these values to generate the bispectral surrogate $Q_{N_{\text{qoi}}}^{\text{PC}}(t, \boldsymbol{\theta}^r)$. As before, to assess the effectiveness of the surrogate to capture the statistical prop-

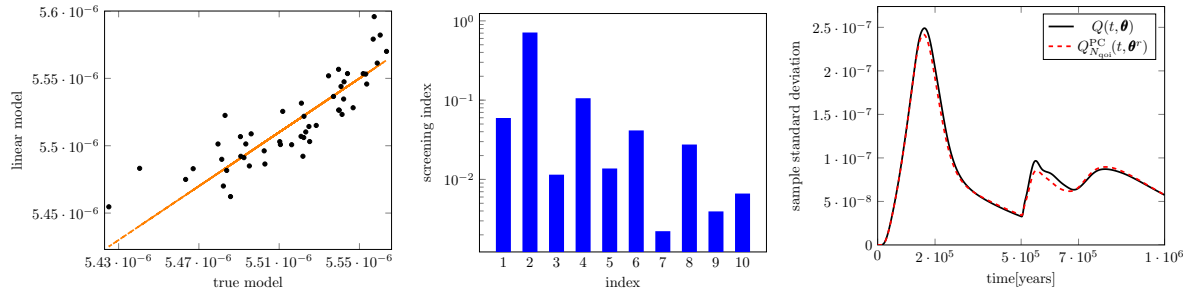


Figure 6.11 Left: comparison of the true model to the linear model for $Q(t, \boldsymbol{\theta})$ at $t = 500,106$ years, middle: screening indices for $Q(t, \boldsymbol{\theta})$, right: comparison of sample standard deviations of $Q(t, \boldsymbol{\theta})$ and $Q_{N_{\text{qoi}}}^{\text{PC}}(t, \boldsymbol{\theta}^r)$ computed with 200 sample points.

erties of the true model we compare the sample standard deviation of the full model $Q(t, \theta)$ and the surrogate $Q_{N_{\text{qoi}}}^{\text{PC}}(t, \theta^r)$, computed on 200 validation samples. Results are displayed in Figure 6.11 (right). Lastly, using 100,000 samples of $Q_{N_{\text{qoi}}}^{\text{PC}}(t, \theta^r)$ we compute pdf estimates at equally spaced points in time and compare to normalized histograms created with 550 full model evaluations; see Figure 6.12. The results in Figure 6.12 and Figure 6.13 (right) demonstrate that the constructed surrogate for gas flux approximates the distribution of the full model reliably.

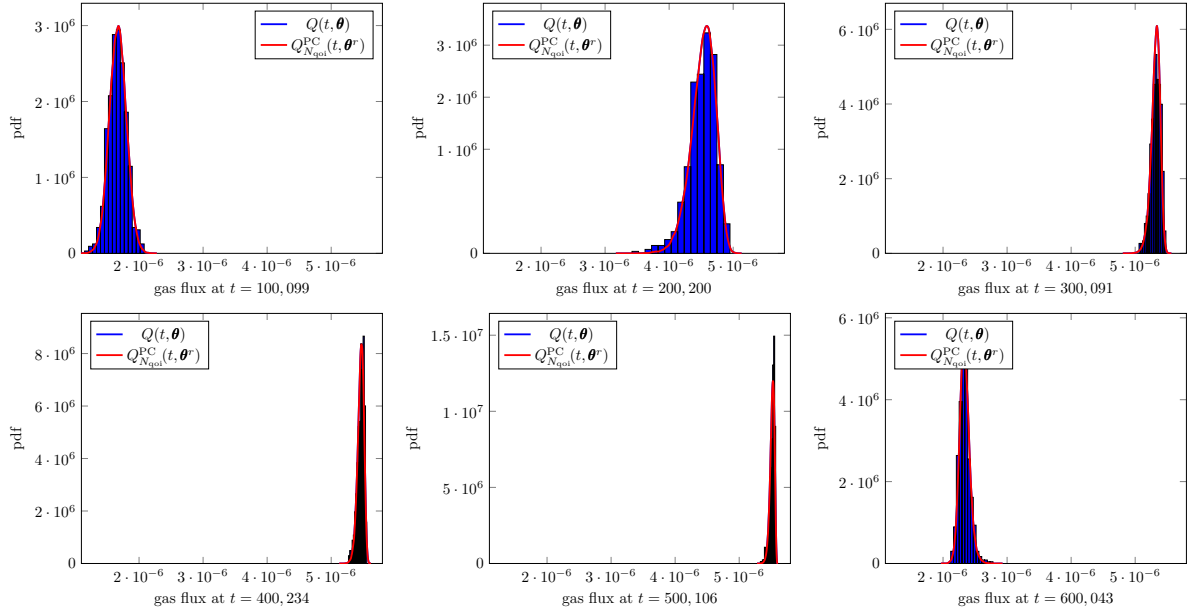


Figure 6.12 Comparison of normalized histograms for $Q(t, \theta)$ and pdf estimates of the surrogate $Q_{N_{\text{qoi}}}^{\text{PC}}(t, \theta^r)$ for a variety of times $t \in [0, T_f]$.

6.6.3 Gas saturation across the domain

In this section, we focus on a *spatially* varying QoI. Let $S(x, \theta; t^*)$ represent the QoI gas saturation across the spatial domain for a fixed time t^* . In particular, we include surrogate results at $t^* \in \{100,099, 300,091, 600,043\}$ years. We display several realizations for each QoI in Figure 6.14 (top). The surrogate models for spatial QoIs are computed via a similar procedure. Hence, for brevity, we include procedure details for $t^* = 600,043$ years only. The relevant parameter values for the other QoIs are included in Table 6.2.

We consider the (spatial) global linear model for $S(x, \theta; t^*)$. In Figure 6.13 (left) the linear model at $x = 65.5$ meters is displayed. The global linear model was observed to perform similarly at other values of x . Next, we compute the screening indices s_j and use the importance tolerance $tol = 0.002$ for dimension reduction resulting in the reduced input parameter

$\boldsymbol{\theta}^r = [\theta_1 \ \theta_2 \ \dots \ \theta_8]^\top$. In Figure 6.13 (middle) we display the screening indices corresponding to these parameters.

Next, we compute the KLE of $S(x, \boldsymbol{\theta}; t^*)$ using Nyström's method with 550 model evaluations. In Figure 6.13 (right) we report the normalized eigenvalues of the output covariance operator \mathcal{C}_{qoi} for $S(x, \boldsymbol{\theta}; t^*)$. This result is included to demonstrate that the gas saturation process is also low-rank in space. We truncate the KLE at $N_{\text{qoi}} = 5$ terms.

As before, the PCE for the KL modes are computed with sparse linear regression using 350 full model realizations. Once again, the cross validation procedure described in section 6.6.1 is used to determine $N_{\text{ord}} = 3$ and $\tau = 2.8$. Lastly, the computed PCEs for each KL mode is used to construct the bispectral surrogate $S_{N_{\text{qoi}}}^{\text{PC}}(x, \boldsymbol{\theta}^r)$. To evaluate the effectiveness of the

Table 6.2 Surrogate parameter values and e_{rel} errors for surrogate models.

surrogate	for fixed t or x	N_{qoi}	N_{ord}	error
$S_{N_{\text{qoi}}}^{\text{PC}}(t, \boldsymbol{\theta})$	$x = 0$ meters	5	2	$3.4813 \cdot 10^{-2}$
$Q_{N_{\text{qoi}}}^{\text{PC}}(t, \boldsymbol{\theta})$	$x = 200$ meters	7	2	$7.5019 \cdot 10^{-3}$
$S_{N_{\text{qoi}}}^{\text{PC}}(x, \boldsymbol{\theta})$	$t^* = 100,099$ years	7	2	$3.0397 \cdot 10^{-2}$
$S_{N_{\text{qoi}}}^{\text{PC}}(x, \boldsymbol{\theta})$	$t^* = 300,091$ years	11	2	$2.1690 \cdot 10^{-2}$
$S_{N_{\text{qoi}}}^{\text{PC}}(x, \boldsymbol{\theta})$	$t^* = 600,043$ years	5	3	$8.3110 \cdot 10^{-2}$

surrogate models for $t^* \in \{100,099, 300,091, 600,043\}$, we compare the sample standard deviation of $S(x, \boldsymbol{\theta}; t^*)$ and $S_{N_{\text{qoi}}}^{\text{PC}}(x, \boldsymbol{\theta}^r)$ for 200 sample points. These results are displayed in Figure 6.14 (bottom). Observe, for $t^* = 100,099$ and $t^* = 300,091$ years the surrogate model replicates the sample standard deviation well. For $t^* = 600,043$ years note that while we are underestimating the sample standard deviation, we are still capture the overall behavior of the full model. The capability of the computed bispectral surrogate to replicate true model behavior can also be tested by computing the average relative error defined in (6.27). Table 6.2 contains the values for e_{rel} computed over the validation set \hat{W} for each surrogate presented in this section, as well as those in sections 6.6.1 and 6.6.2. Note that for the spatially varying QoIs, we let $\mathcal{X} = [0, 200]$ and for temporally varying we let $\mathcal{X} = [0, T_f]$, in (6.27). Note, the error across all surrogates is less than 8%, and in four out the five surrogates is less than 4%. The largest e_{rel} corresponds to $S_{N_{\text{qoi}}}^{\text{PC}}(c, \boldsymbol{\theta})$ at $t = 600,043$ years, in which case we are also underestimating the standard deviation.

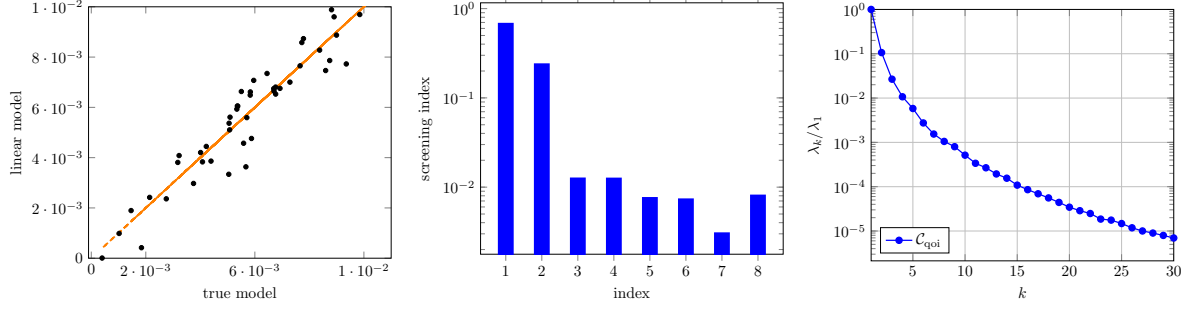


Figure 6.13 Results for $S(x, \theta; t^*)$ with $t^* = 600,043$ years. Left: comparison of the true model and the linear model for gas saturation across the domain, middle: screening indices for $S(x, \theta; t^*)$, right: ratio λ_k / λ_1 , $k = 1, \dots, 30$ for $\lambda_k(C_{qoi})$ corresponding to $S(x, \theta; t^*)$.

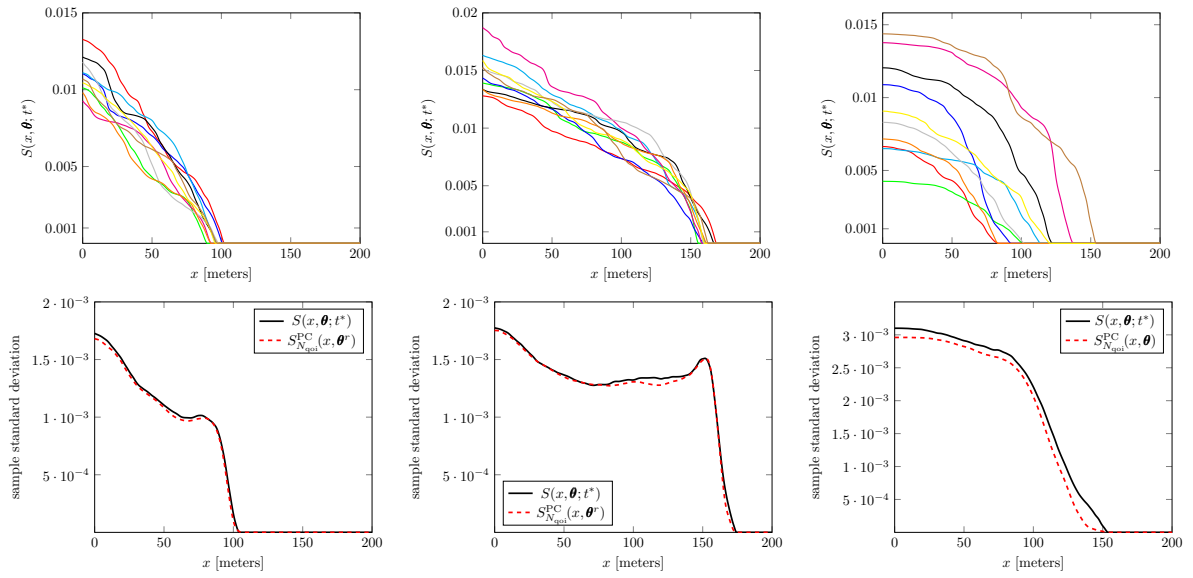


Figure 6.14 Top row, left to right: sample realizations of $S(x, \theta; t^*)$ for times 100,099, 300,091, and 600,043 years; bottom row, left to right: comparison of sample standard deviation of $S(x, \theta; t^*)$ and $S_{N_{qoi}}^{PC}(x, \theta; t^*)$ computed on 200 sample points.

6.6.4 Using the surrogate model

Here we illustrate the use of surrogates for temporally varying QoIs in performing statistical studies. In particular, we perform model prediction, variance-based global sensitivity analysis, and a study of output correlation structure.

Model prediction. We consider using $S_{N_{qoi}}^{PC}(t, \theta^r)$ and $Q_{N_{qoi}}^{PC}(t, \theta^r)$ for making predictions. Recall, these bispectral surrogates correspond to gas saturation at the inflow boundary and gas flux at the outflow boundary. We study three observables of interest: maximum gas saturation, denoted S_{\max} , maximum gas flux, denoted Q_{\max} , and the first time for which gas saturation rises above 20% of S_{\max} . We compute 100,000 realizations of each surrogate, extract the pertinent observables, and use the samples to compute pdf estimates. In Figure 6.15, we

compare the pdf estimates against the normalized histograms computed using exact model evaluations. These results indicate the utility of the surrogates for estimating the statistical properties of model observables.

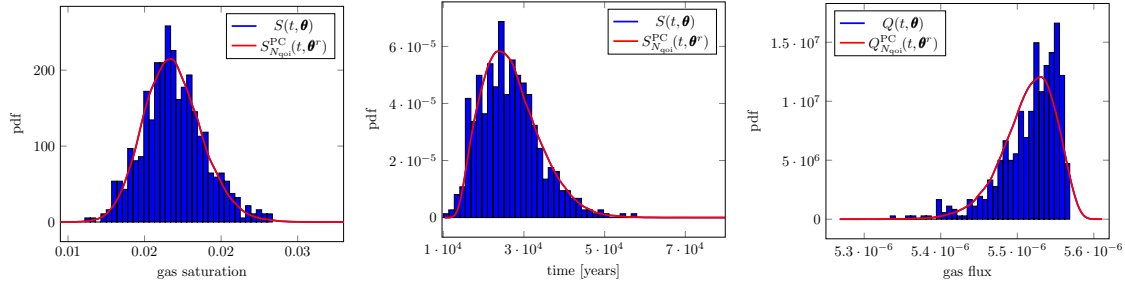


Figure 6.15 Comparison of normalized histograms and pdf estimates for left: max saturation value of S_{\max} , middle: first time $S_{N_{\text{qoi}}}^{\text{PC}}(t, \theta^r)$ is above 20% S_{\max} , right: max flux value Q_{\max} .

Variance based sensitivity analysis via Sobol' indices. total Sobol' indices provide an informative global sensitivity analysis tool that apportions percentages of QoI variance due to input parameter variations. While total Sobol' indices are traditionally applied to scalar QoIs [99, 100], there exist extensions for variance based analysis to function-valued QoIs [6, 41], referred to as *functional* total Sobol' indices.

In general, calculating Sobol' indices for computationally intensive models is challenging. This involves an expensive sampling procedure that requires a large number of model evaluations. An efficient-to-evaluate surrogate model can be used to accelerate this process. We use the temporal surrogates to compute total Sobol' indices for both function-valued and scalar QoIs. In particular, we compute the functional total Sobol' indices for $S_{N_{\text{qoi}}}^{\text{PC}}(t, \theta^r)$ and $Q_{N_{\text{qoi}}}^{\text{PC}}(t, \theta^r)$, both of which are functions in t , and we compute the total Sobol' indices for the scalar QoIs S_{\max} and Q_{\max} . In each case, we compute the total Sobol' indices via sampling, using a variety of samples sizes: $N_s = \{1,000, 10,000, 50,000\}$.

The results in the top row of Figure 6.16 show the functional Sobol' indices for $S_{N_{\text{qoi}}}^{\text{PC}}(t, \theta^r)$ and $Q_{N_{\text{qoi}}}^{\text{PC}}(t, \theta^r)$. Note that the magnitudes in the top row of Figure 6.16 are similar to those in Figure 6.7 (right) and Figure 6.11 (middle). This provides further support for the original input parameter importance ranking and subsequent dimension reduction. In the bottom row of Figure 6.16 we report the total Sobol' indices for S_{\max} and Q_{\max} . We also note that for the gas saturation QoIs Figure 6.16 (left: top and bottom), the importance ranking of the input parameters is similar. In contrast, there is more variability in ranking for gas flux QoIs Figure 6.16 (right: top and bottom).

Finally, we mention that for many applications, the total Sobol' indices can be used for further input parameter dimension reduction. For the present model however, we did not reduce the input parameter further because the surrogate model computed was already efficient and

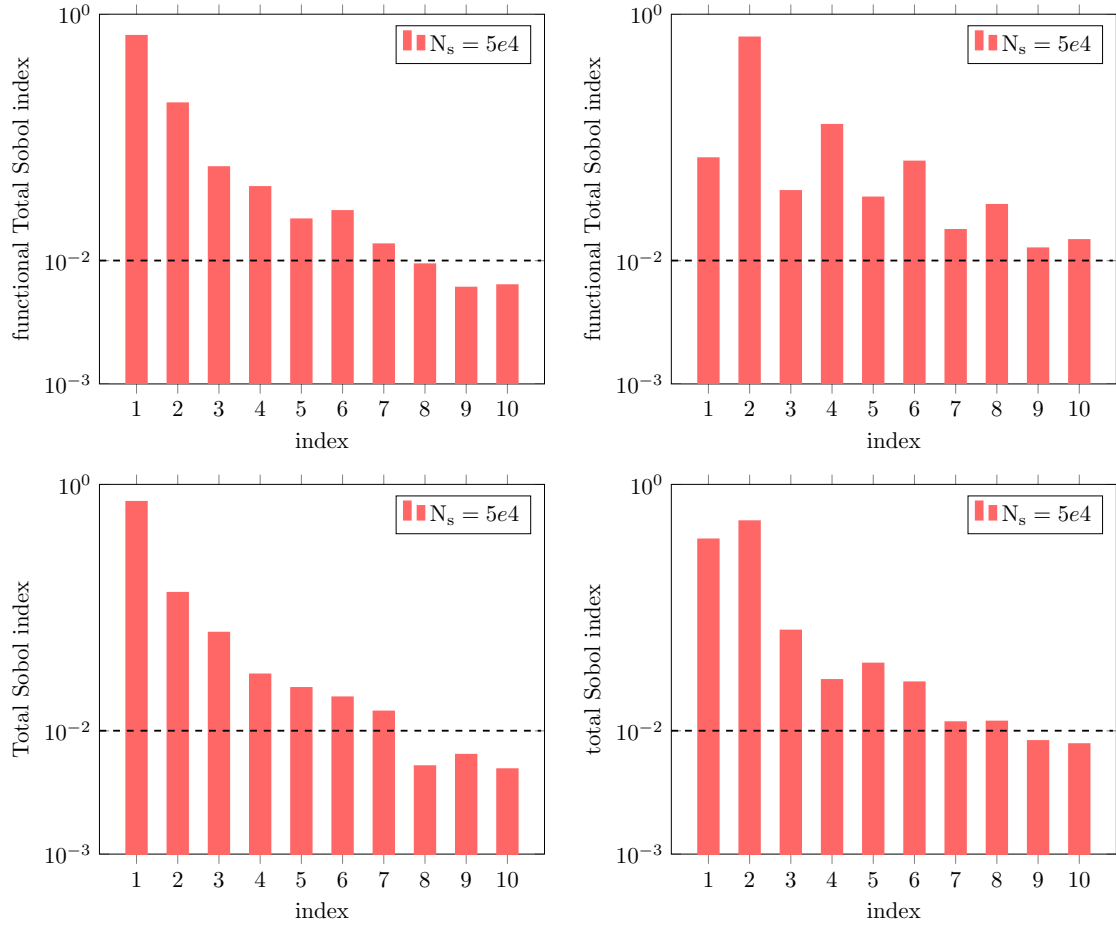


Figure 6.16 From top left counter clockwise: functional total Sobol' indices for $S_{N_{\text{qoi}}}^{\text{PC}}(t, \theta^r)$, functional total Sobol' indices for $Q_{N_{\text{qoi}}}^{\text{PC}}(t, \theta^r)$, total Sobol' indices for S_{max} , total Sobol' indices for Q_{max} .

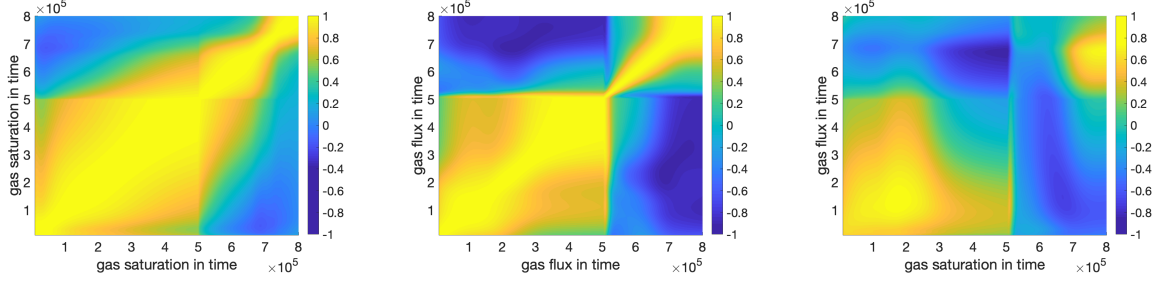


Figure 6.17 Left: correlation matrix for $S_{N_{qoi}}^{PC}(t, \theta^r)$ computed using the analytic formula in (6.24), middle: correlation matrix for $Q_{N_{qoi}}^{PC}(t, \theta^r)$ computed using the analytic formula in (6.24) right: cross-correlation structure of $S_{N_{qoi}}^{PC}(t, \theta^r)$ and $Q_{N_{qoi}}^{PC}(t, \theta^r)$ computed using the analytic formula in (6.25).

sufficiently accurate.

Correlation structure Lastly, we illustrate the use of the bispectral surrogates for computing the correlation structure of the output, which is a useful tool for understanding overall model dynamics. Using equation (6.24) we compute the correlation function of $S_{N_{qoi}}^{PC}(t, \theta^r)$ and $Q_{N_{qoi}}^{PC}(t, \theta^r)$. The resulting heat maps are shown in Figure 6.17 (left) and (middle), respectively. The results for $S_{N_{qoi}}^{PC}(t, \theta^r)$ suggest significant correlations across time. This behavior is also seen in the correlation function of $Q_{N_{qoi}}^{PC}(t, \theta^r)$, except the sudden shift in dynamics at the time $t = 500,000$ years; recall, this is the time gas injection stops. We also compute the cross-correlation between $S_{N_{qoi}}^{PC}(t, \theta^r)$ and $Q_{N_{qoi}}^{PC}(t, \theta^r)$ using the formula in (6.25); see Figure 6.17 (right). The heat map suggests there is large cross-correlation between the two QoI for both early and late times.

6.7 Conclusion

We have presented a structure exploiting non-intrusive framework for efficient dimension reduction and surrogate modeling for models with high-dimensional inputs and outputs. The proposed parameter screening metric utilizes approximate global sensitivity measures for function-valued outputs that rely on concepts from global sensitivity analysis and active subspace methods. An efficient bispectral surrogate model was constructed from a truncated KLE of the QoI by approximating the KL modes with PCEs. Note, these KL mode PCEs were constructed in the reduced parameter space.

We deployed our framework for fast uncertainty analysis in a multiphase multicomponent flow model. The efficiency and effectiveness of the surrogate model was demonstrated with a comprehensive set of numerical experiments, where we consider a number of function-valued (temporally or spatially distributed) QoIs. In particular, our results indicate that it is possible to use a modest amount of model realizations to reduce both the input and output dimensions and construct an efficient surrogate model. The proposed framework not only provides efficient surrogates, it also reveals and exploits the low-dimensional structures in model input and output spaces, which provides further insight into the behavior of the governing model.

Our approach relies on the screening metrics being sufficiently accurate surrogates for the derivative based global sensitivity measures for the function-valued QoIs under study. This in turn assumes the global linear model constructed within the parameter screening procedure leads to a sufficient approximation of the activity scores. It is observed that this global linear model can successfully capture one-dimensional active subspaces in a wide range of applications [27]. The success of this strategy for obtaining approximate activity scores was also observed in the present work, in the context of a complex nonlinear flow model. However, for models that exhibit highly nonlinear parameter dependence a linear model might fail to provide accurate global sensitivity information. In [43, 96], global quadratic models were used effectively to accelerate active subspace discovery for scalar-valued QoIs. Exploring quadratic models within our framework provides an interesting direction for future work and would allow application of the proposed strategy to a broader class of problems.

SENSITIVITY ANALYSIS FOR STOCHASTICALLY FORCED DIFFERENTIAL EQUATIONS

7.1 Introduction

The previous chapters have focused on global sensitivity analysis (GSA) for deterministic systems. In this chapter, we investigate GSA for stochastic systems of the form:

$$\dot{\mathbf{x}}(t, \boldsymbol{\theta}, \omega) = \mathbf{f}(\mathbf{x}; \boldsymbol{\theta}) + \mathbf{z}(t, \boldsymbol{\theta}, \omega), \quad (7.1)$$

where $\boldsymbol{\theta}$ is a vector sampled from an uncertain parameter space $\Theta \subseteq \mathbb{R}^{N_p}$, the function $\mathbf{f}(\mathbf{x}; \boldsymbol{\theta})$ corresponds to a deterministic process, and for every $\boldsymbol{\theta} \in \Theta$, we have $\mathbf{z}(t, \boldsymbol{\theta}, \omega) : \mathcal{T} \times \Omega \rightarrow \mathbb{R}^n$ is a vector-valued stochastic process, where ω is an element of a sample space Ω , and $t \in \mathcal{T} = [0, T_f]$, for some final time T_f .

Recall, GSA seeks to quantify the uncertainty in the model output as a consequence of the uncertainty in model inputs. While this is often straightforward for deterministic models, the intrinsic stochasticity in systems of the form (7.1) means there is an additional source of uncertainty to contend with. The intention of this chapter is to examine the behavior of derivative-based GSA in systems of the form (7.1). In particular, we focus our exploration on derivative-based global sensitivity measures (DGSMs) for solutions to random ordinary differential equations (RODEs) arising from stochastically forced ordinary differential equations. We will model the forcing term $\mathbf{z}(t, \boldsymbol{\theta}, \omega)$ in (7.1) via solutions to stochastic differential equations (SDEs) solved using the Stratonovich interpretation of the stochastic integral.

The contributions of this chapter are as follows. Two candidate derivative-based global sensitivity measures (DGSMs) are proposed and investigated. Each proposed DGSM is formulated to measure the sensitivity of a different aspect of the QoIs. Our results indicate the

need for careful treatment of this type of analysis. We demonstrate the behaviors of the two proposed DGSMs on a biological model describing the evolution of lead in the body [36]. Numerical and analytic tools are deployed in our exploration. We also include details regarding more practical concerns, such as the difference between RODEs and SDEs as well as the properties of \mathbf{z} for which the system in (7.1) is mathematically valid. We include details for generating realizations of the forcing term. This approach utilizes an easy-to-implement numerical framework for solving SDEs via smooth approximations to the stochastic process.

This chapter is organized as follows. In section 7.2, we provide relevant definitions for RODEs, SDEs, and emphasize key differences between the two. Also included in this section are definitions for Brownian motion, geometric Brownian motion, and the Ornstein-Uhlenbeck process.

In section 7.3, we provide details for a system of RODEs describing the movement of lead in the human body. The numerical scheme for generating realizations of the stochastic forcing term is described in section 7.4.1. Definitions of the explored DGSMs are provided in section 7.4.2. We compute and compare the proposed DGSMs in section 7.5 for a QoI extracted from the lead in the body model. In particular, we perform analysis of the QoI when the model is forced by geometric brownian motion and when it is forced by the Ornstein-Uhlenbeck process. Discussion and concluding remarks are provided in section 7.6.

7.2 Random ordinary differential equations

In this section, we cover background concepts including definitions for random ordinary differential equations (RODEs) and their distinction from stochastic differential equations (SDEs). We also discuss three random processes used in stochastically forced differential equations.

In general, RODEs are ordinary differential equations that have random coefficients, random initial conditions, random forcing terms, or a combination therein. Formally, consider definition 3.4 from [75],

Definition 7.2.1 (Random Ordinary Differential Equation). *A random ordinary differential equation on \mathbb{R}^d ,*

$$\frac{dX_t}{dt} = f(X_t(\omega), t, \omega), \quad X_t(\omega) \in \mathbb{R}^d, \quad (7.2)$$

is a non-autonomous ordinary differential equation for almost all $\omega \in \Omega$, where Ω is a sample space.

In the present work, we focus on stochastically forced RODEs of the form (7.1), and consider solutions *pathwise* in Ω . Specifically, we assume for almost all θ , $\mathbf{z}(t, \theta, \omega)$ is an almost surely path-continuous stochastic process (meaning for almost all $\omega \in \Omega$ we have $\mathbf{z}(t, \theta, \omega)$ is continuous in t). Therefore, *for a fixed realization of the forcing term*, the RODE in (7.1) simplifies to an equation whose solution can be analyzed with standard tools from ordinary differential equations.

SDEs versus RODEs. The difference between RODEs and SDEs is a common source of confusion we will briefly address. The differential form of an SDE is given by Definition 5.1.1 in [77]

Definition 7.2.2 (Stochastic Differential Equation). *The differential form of a stochastic differential equation is given by*

$$\frac{dX_t}{dt} = b(t, X_t) + \sigma(t, X_t) \frac{dB_t}{dt}, \quad b(t, x), \sigma(t, x) \in \mathbb{R}, \quad (7.3)$$

and $\frac{dB_t}{dt}$ is a white noise process.

A white noise process is a highly irregular random process that can be thought of as the continuous analog of a discrete random walk. Based on the formulation in (7.3), another common intuitive understanding of white noise is as the infinitesimal change in the Brownian motion, B_t (see Definition 7.2.3). The mathematically rigorous incorporation of white noise into differential equations is highly technical, and generates an entirely different interpretations of calculus. Yet another level of complexity arises from the fact that there are dissimilar, equally valid, interpretations of stochastic calculus. The two most common are Itô and the Stratonovich calculus. For more information on stochastic calculus see e.g., [55, 77]. In the present work, we will focus on the Stratonovich interpretation. This is partially a consequence of the chosen numerical method (see section 7.4.1).

At first glance, the formulation in (7.3) does not appear vastly dissimilar from the definition given for RODEs. However the mathematical interpretation of (7.3) and (7.2) are very different. Simply put, the solutions to RODEs have sample paths which are differentiable with respect to t and SDEs do not. That may sound contradictory. How can a solution to a differential equation *not* be differentiable? SDEs are often written in a differential form, but are understood as *stochastic integrals*. Thus, 7.3 can be written in the form [77]

$$X_t = \int_0^{T_f} b(t, X_t) dt + " \int_0^{T_f} \sigma(t, X_t) dB_t ", \quad b(t, x), \sigma(t, x) \in \mathbb{R}.$$

Note, the quotations around the second term are intentional. How we interpret this term determines the version of stochastic calculus we will be working in. This distinction is important because the different interpretations of stochastic integral will, in general, result in different answers. In the present work, we use the Stratonovich interpretation, which we denote $\int_0^{T_f} \sigma(t, X_t) \circ dB_t$.

The stochastic forcing term. There are many path-continuous stochastic processes that we can use as forcing terms to generate RODEs. In this section we give definitions for three such processes: the standard Brownian motion, the geometric Brownian motion (GBM), and the Ornstein-Uhlenbeck (OU) process.

We consider the following definition for the canonical Brownian motion [35] (also known as a standard Wiener process)

Definition 7.2.3. A one dimensional Brownian motion is a real-valued process $B(t) = B_t$, $t \geq 0$ with the following properties

- i If $t_0 < t_1 < \dots < t_n$, then $B(t_0), B(t_1) - B(t_0), \dots, B(t_n) - B(t_{n-1})$ are independent.
- ii If $s, t \geq 0$, then $B(s+t) - B(s) \sim \mathcal{N}(0, t)$.
- iii With probability one, $t \mapsto B_t$ is continuous.

The standard Brownian motion is a path-continuous, nowhere differentiable, random process. Arising in disciplines ranging from biology to economics, the Brownian motion is a fundamental component in stochastic analysis. The Brownian motion has mean zero and covariance $\text{Cov}(B_t, B_s) = t$, for $t \leq s$. Therefore, the long-term behavior of Brownian motion (i.e. behavior as $t \rightarrow \infty$) is a process with infinite variance and zero mean. This makes B_t a poor choice for modeling physical phenomena for which control over the long-term behavior is necessary.

Another path-continuous stochastic process considered in the present work is the geometric Brownian motion (GBM). Commonly used in stock market modeling, the GBM solves the following SDE [77]

$$dX_t = \mu X_t dt + \sigma X_t \circ dB_t \quad (7.4)$$

where B_t is the standard Brownian motion, $\mu \in \mathbb{R}$ and $\sigma > 0$. The Stratonovich solution to (7.4) is given by [77]

$$X_t = X_0 e^{\mu t + \sigma B_t}. \quad (7.5)$$

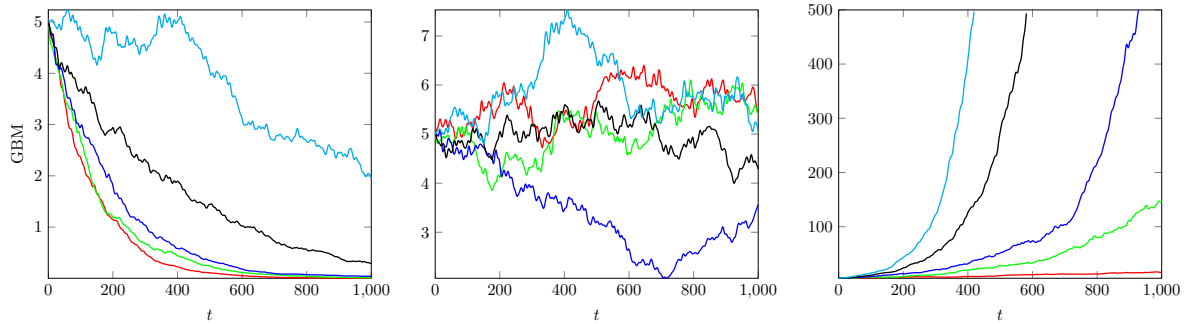


Figure 7.1 Left to right: GBM realizations when $\mu < -\sigma^2/2$, $\mu = -\sigma^2/2$, and $\mu > -\sigma^2/2$, with initial valued $X_0 = 5$.

The formulas for the mean and variance of the Stratonovich GBM are [77]:

$$\mathbb{E}\{X_t\} = X_0 e^{(\mu + \sigma^2/2)t}, \quad \text{and} \quad \text{Var}\{X_t\} = X_0^2 e^{(2\mu + \sigma^2)t} (e^{\sigma^2 t} - 1) \quad (7.6)$$

Different choices of σ and μ will change the long-term behavior of both the mean and variance of the process. Indeed, For $\mu < -\sigma^2/2$ The long-term mean of the process will decay to zero. In the case of $\mu = -\sigma^2/2$, the longterm mean of the GBM be the initial value X_0 . Lastly, the mean of the process will tend towards infinity when $\mu > -\sigma^2/2$. We display realizations of the GBM under these three conditions (left)-(right), respectively, in Figure 7.1.

Lastly, we consider the Ornstein-Uhlenbeck (OU) process. The OU process solves the following SDE [77]:

$$dX_t = k(\mu - X_t)dt + \sigma \circ dB_t, \quad (7.7)$$

where $\mu \in \mathbb{R}$, $\sigma > 0$, and $k > 0$. The solution is given by

$$X_t = X_0 e^{-kt} + \mu(1 - e^{-kt}) + \sigma \int_0^t e^{-k(t-s)} \circ dB_s. \quad (7.8)$$

The OU process is referred to as *mean-reverting* because as t grows, the solution in (7.8) drifts towards its long-term mean, μ . The rate at which mean-reversion occurs is controlled by the parameter k , the larger k is the faster the mean reversion happens. In Figure 7.2 we display several realizations of the OU process simulated with various k values sampled from the interval $[0.01 \ 0.5]$. All simulations were done with $\mu = 35$, $X_0 = 5$, and $\sigma = 1$.

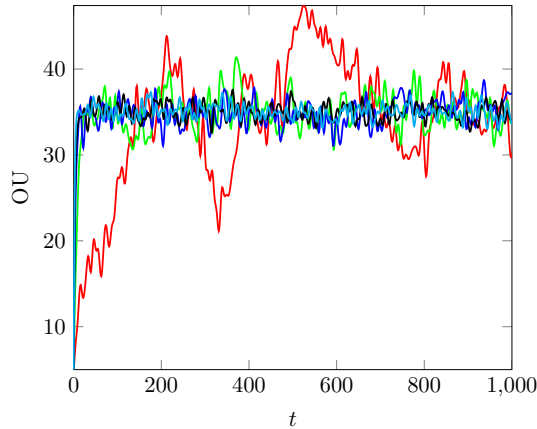


Figure 7.2 Realizations of the OU process for various k , and $\mu = 35$, $X_0 = 5$, and $\sigma = 1$.

The mean and variance of an OU process is as follows [95]:

$$\mathbb{E}\{X_t\} = X_0 e^{-kt} + \mu(1 - e^{-kt}), \quad \text{Var}\{X_t\} = \frac{\sigma^2}{2k}(1 - e^{-2kt}). \quad (7.9)$$

The long-term variance of the OU process is $\sigma^2/2k$. This, combined with the mean-reversion property allows easy control over the time evolution of the OU process. Therefore, (7.8) is

an ideal candidate for modeling random terms for which it is necessary to control long-term behavior.

7.3 Motivating application

Consider the compartment model displayed in Figure 7.3, that describes how lead enters the body, dissolves in the blood stream, and is absorbed by the surrounding tissue and bone. We investigate this linear model because it is an interesting application and its formulation allows for both easy numerical and analytic investigation. Details for this model are taken from [36, 113]. We denote the level of lead (in μg) in blood, tissue, and bone at time t by x_1 , x_2 , and x_3 ,

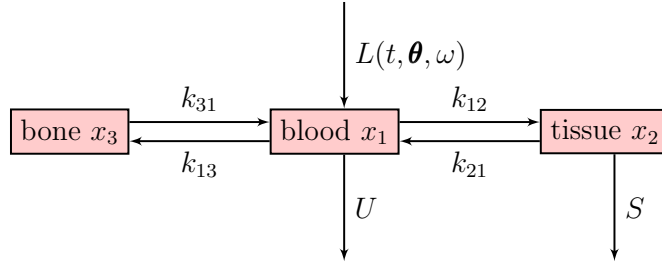


Figure 7.3 Flow of lead in and out of the human body.

respectively. The parameters U and S are the (constant) rates in micrograms/day ($\mu\text{g}/\text{day}$) at which lead is excreted from blood and tissue, respectively. The rate at which lead moves from compartment i to compartment j is denoted by k_{ij} and is measured in $\mu\text{g}/\text{day}$. The forcing term $L(t, \theta, \omega)$ corresponds to the amount of lead entering the body at time t and is measured in $\mu\text{g}/\text{day}$. In practice, the amount of lead entering the blood can fluctuate randomly in time. Thus, we model $L(t, \theta, \omega)$ with a path-continuous stochastic process to account for this behaviour. Consequently, the system in Figure 7.3 becomes a system RODEs of the form (7.1).

Modeling the stochastic forcing term We model the noise L via the GBM (7.5) or the OU process (7.8), and let $X_0 = L_0$ be the amount of lead entering the system at time $t = 0$. Note, we do not use the canonical Brownian motion B_t to force this model. Recall, we have no way of controlling the longterm behavior of B_t . Furthermore, the Brownian motion takes on negative values. Thus, from a modeling standpoint B_t does not make physical sense for the amount of lead entering the blood at time t .

Modeling the uncertainty in the input The numerical experiments conducted in the present work consider the following uncertain parameter vector

$$\theta = \left[U \quad k_{12} \quad k_{21} \quad k_{13} \quad k_{31} \quad S \quad L_0 \quad \sigma \right]^T, \quad (7.10)$$

Table 7.1 Model parameters for (7.11) [36].

Model parameter	Symbol	Units	Nominal Value
Rate of lead removed from blood	U	$\mu\text{g/day}$	0.021
Rate of lead transferred <i>from</i> blood <i>to</i> tissue	k_{12}	$\mu\text{g/day}$	0.011
Rate of lead transferred <i>from</i> tissue <i>to</i> blood	k_{21}	$\mu\text{g/day}$	0.012
Rate of lead transferred <i>from</i> blood <i>to</i> bone	k_{13}	$\mu\text{g/day}$	$3.5e - 5$
Rate of lead transferred <i>from</i> bone <i>to</i> blood	k_{31}	$\mu\text{g/day}$	0.0039
Rate of lead removed from tissue	S	$\mu\text{g/day}$	0.016
Amount of lead entering the blood at $t = 0$	L_0	μg	49.3

Table 7.2 Noise parameter values used to simulate $\mathbf{z}(t, \boldsymbol{\theta}, \omega)$ in (7.11).

Noise type	Parameter symbol	Units	Nominal Value
GBM	σ	unitless	0.1
GBM	μ	unitless	$-\sigma^2/2$
OU	σ	unitless	1.0
OU	μ	μg	35.0
OU	k	unitless	0.2

where $\theta_1, \dots, \theta_6$ correspond to the rates from the compartment model in Figure 7.3, $L_0 = L(0, \boldsymbol{\theta}, \omega)$, and σ is a noise parameter. Nominal values for $\boldsymbol{\theta}$ and the other noise parameters are given in Table 7.1. The uncertainties of the first seven entries of the parameter vector $\boldsymbol{\theta}$ are modeled according to $\theta_i = \hat{\theta}_i + 0.1\hat{\theta}_i a_i$ where $a_i \sim \mathcal{U}(-1, 1)$ with $\hat{\theta}_i$ corresponding to the nominal value for θ_i , for $i = 1 \dots 7$. For $i = 8$ we use $\theta_8 = \hat{\theta}_8 + 0.5\hat{\theta}_8 a_8$, with $a_8 \sim \mathcal{U}(-1, 1)$.

The linear system. The model described in Figure 7.3 translates into the following inhomogeneous system of linear differential equations:

$$\dot{\mathbf{x}} = \mathbf{A}(\boldsymbol{\theta})\mathbf{x} + \mathbf{z}(t, \boldsymbol{\theta}, \omega), \quad (7.11)$$

where

$$\mathbf{A}(\boldsymbol{\theta}) = \begin{bmatrix} -(U + k_{12} + k_{13}) & k_{21} & k_{31} \\ k_{12} & -(S + k_{21}) & 0 \\ k_{13} & 0 & -k_{31} \end{bmatrix} \quad \text{and} \quad \mathbf{z}(t, \boldsymbol{\theta}, \omega) = \begin{bmatrix} L(t, \boldsymbol{\theta}, \omega) \\ 0 \\ 0 \end{bmatrix},$$

with,

$$\mathbf{x}(0, \boldsymbol{\theta}, \omega) = \begin{bmatrix} 0 & 0 & 0 \end{bmatrix}^T.$$

7.4 Methods

In this section, we first present a numerical framework for approximating solutions to SDEs. The approach is adapted from the work presented in [38]. We then propose two possible derivative-based global sensitivity measures (DGSMs), each of which measures a different aspect of the QoI. Lastly, we analytically investigate the expectation of the solution of (7.11) with respect to ω in order to provide further insight into the behavior of the proposed sensitivity measures.

7.4.1 Smooth random functions for approximating noise in dynamical systems

We are solving RODEs arising from ODEs with stochastic forcing terms. The stochastic forcing terms are assumed to be almost-surely path-continuous. This means that for almost all ω we can implement traditional numerical techniques for solving differential equations. However, due to the possible low regularity of the incorporated stochastic process, the traditional numerical solution techniques do not retain their usual convergence rates when applied to RODEs. There are a variety of ways to cope with these irregularity, such as time averaging methods proposed in [44]. For the present work, we focus on a simple-to-implement alternative inspired by the approach taken in [38]. The article [38] considers solving SDEs using a truncated Fourier series with random coefficients to approximate the white noise. The authors refer to these approximations as *big smooth random functions*. Big smooth random functions refer to both *periodic big smooth random functions* and *non-periodic big smooth random functions*. Periodic big smooth random functions are defined as follows [38]:

Definition 7.4.1 (Periodic big smooth random function). *For some interval $[-\frac{M}{2}, \frac{M}{2}]$, a periodic big smooth random function approximation of a function f takes the form:*

$$f(x) \approx a_0 + \frac{2}{\sqrt{\pi}} \sum_{j=1}^m \left[a_j \cos\left(\frac{2\pi jx}{M}\right) + b_j \sin\left(\frac{2\pi jx}{M}\right) \right], \quad m = \left\lfloor \frac{M}{\lambda} \right\rfloor \quad (7.12)$$

where $\lambda > 0$ is the so-called "wave number" and the random coefficients are independent with $a_j, b_j, \sim \mathcal{N}(0, \frac{2}{2m+1})\lambda$.

Non-periodic big smooth random functions are handled by creating a periodic big smooth random function on a larger interval of length $M' \gg M$, and restricting the resulting series appropriately. The limiting behavior of the integrals of big smooth random functions are well-behaved. In particular, as $\lambda \rightarrow 0$ the solution of an SDE containing a big smooth random function approximation of the white noise will converge in probability to the Stratonovich solution (Theorem 5.1 in [38]).

Included in [38] is an introduction to using the software package Chebfun [34] to solve stochastic differential equations. Chebfun is an open-source MATLAB-based package. We use Chebfun to get smooth approximations of the stochastic processes defining the stochastic forcing term of the studied RODEs. Solving SDEs using big smooth random functions is not a new concept. However, the benefit of Chebfun is it provides an easy-to-implement approach for computing several smooth approximations to a stochastic process. In turn, this smooth approximations allows the use of traditional numerical ODE solution techniques, making it simple to generate many QoI realizations. The ability to easily sample the QoI is invaluable as the estimation of several GSA tools rely on sampling.

We numerically investigate the impact of the wave number λ on the QoI $x_1(t, \theta, \omega)$ from (7.11), which corresponds to the amount of lead in the blood at time t . For this study we used a Intel core i7 dual core processor along with MATLAB version R2018a. Timing results may vary for different machines and software versions.

Table 7.3 Columns left to right: noise type, wave number, seconds compute one smooth white noise sample, seconds to compute one realizations of noise term, seconds to solve one realization of x_1 from system in (7.11).

noise type	wave number	white noise	$L(t, \theta, \cdot)$	ODE solve
GBM	$\lambda = 0.1$	17.6	156.86	18.04
GBM	$\lambda = 10.0$	0.39	1.47	0.96
OU	$\lambda = 0.1$	16.50	183.49	22.47
OU	$\lambda = 10.0$	0.37	1.62	0.91

For $\lambda = 0.1$ and $\lambda = 10$ we compute $N_\Omega = 1,000$ samples of $x(t, \theta, \cdot)$ with the components of θ and noise parameters fixed at their nominal values (see Table 7.1). In Table 7.3 for OU and GBM noise types we report the amount of time in seconds it takes to simulate one sample of the white noise term, the stochastic forcing term, and the QoI solutions for both values of λ . In the top row of Figure 7.4 we compare different realizations of the QoI computed with the forcing term L modeled by GBM. In particular, compare the value of x_1 when the smooth approximation of the GBM is computed with $\lambda = 0.1$ (black) and $\lambda = 10$ (red). We observe

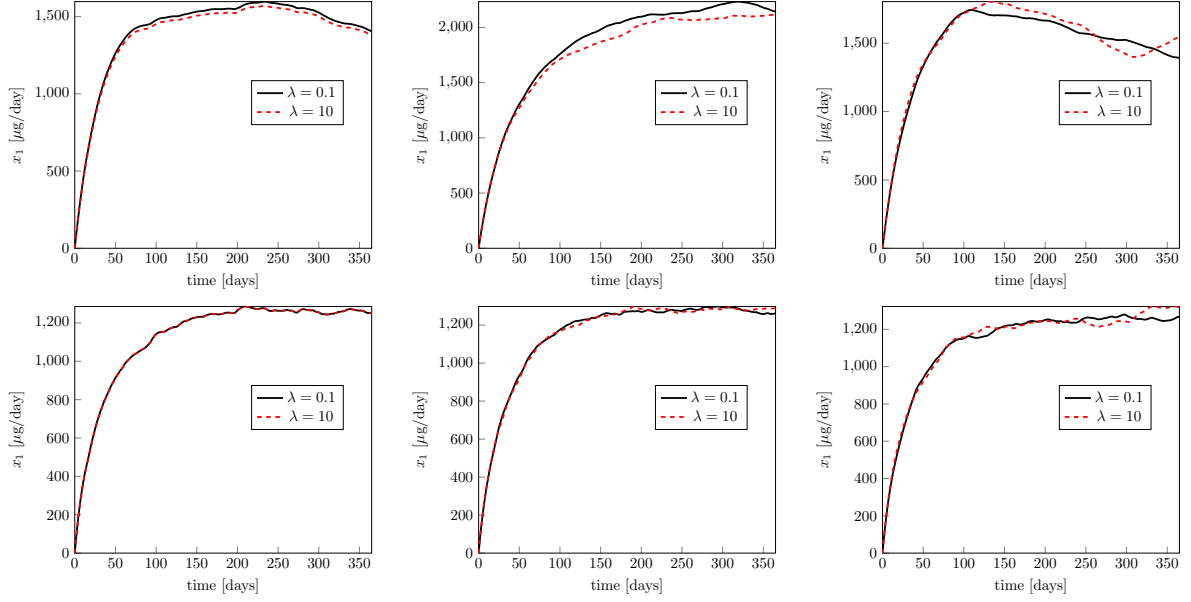


Figure 7.4 Top row: comparison of realizations for $x_1(t, \theta, \omega)$ with GBM noise computed with $\lambda = 0.1$ (black) and $\lambda = 10$ (red). Bottom row: comparison of realizations for $x_1(t, \theta, \omega)$ with OU noise computed with $\lambda = 0.1$ (black) and $\lambda = 10$ (red).

that the QoI behavior is very similar for both λ values. We repeat the same study for the case of OU forcing and display the results in the bottom row of Figure 7.4. Once again, we observe similar behavior of the two computed realizations of the QoI. In the top row of Figure 7.5, we display the mean (left) and standard deviation (right) over time of the QoI forced by GBM calculated with $N_\Omega = 1,000$. In Figure 7.5 (bottom left and right), we display the same values for the case of OU forcing. Observe, the QoI expectation and standard deviation of x_1 with $\lambda = 0.1$ is reasonably similar to the expectation and standard deviation computed with $\lambda = 10$ for both noise types. We also note that the amount of time to run the simulations is significantly less for $\lambda = 10$ than for $\lambda = 0.1$. Therefore, for the numerical studies in the present work we choose to simulate the stochastic forcing term with $\lambda = 10$.

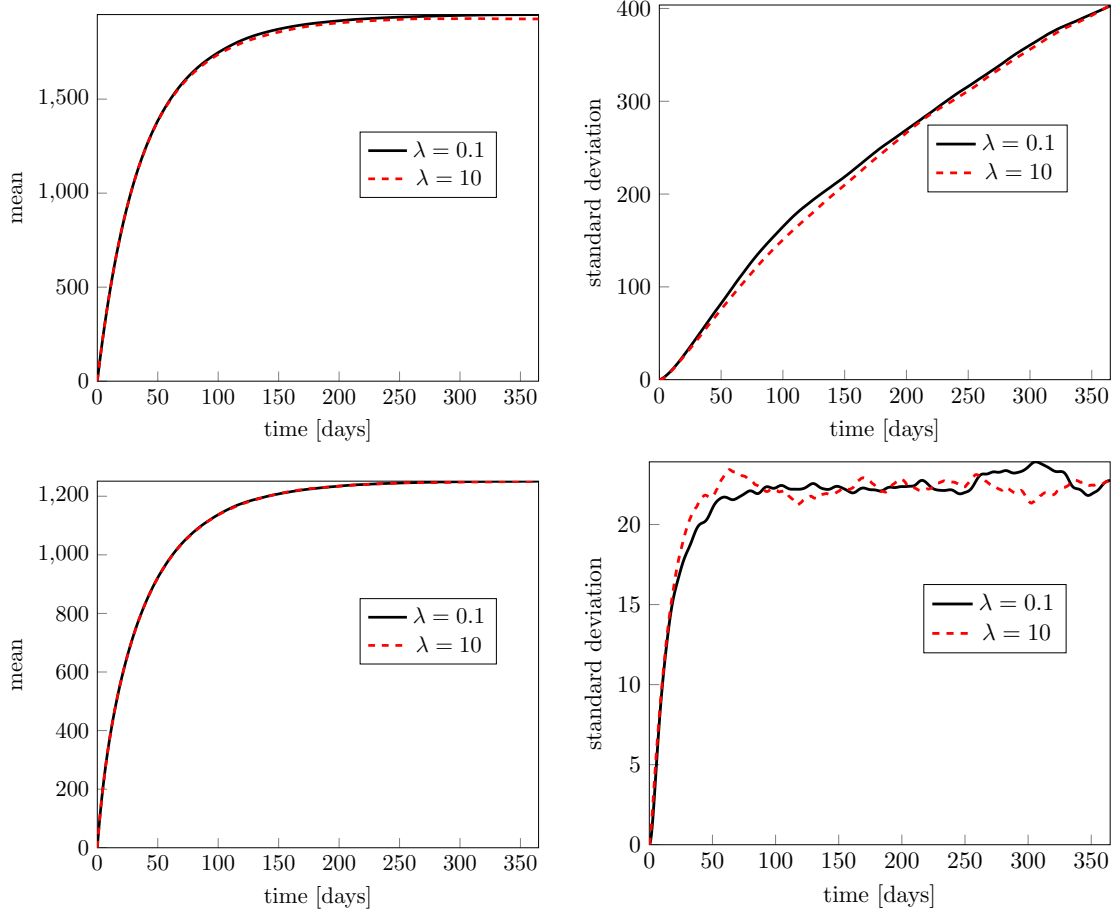


Figure 7.5 Top: mean (left) and standard deviation (right) comparison of $x_1(t, \boldsymbol{\theta}, \omega)$ with $N_\Omega = 1,000$ simulations of the GBM noise computed with $\lambda = 0.1$ (black) and $\lambda = 10$ (red). Bottom: mean (left) and standard deviation (right) comparison of $x_1(t, \boldsymbol{\theta}, \omega)$ with $N_\Omega = 1,000$ simulations of the OU noise computed with $\lambda = 0.1$ (black) and $\lambda = 10$ (red).

7.4.2 Derivative-based global sensitivity analysis

We want to understand how uncertainties in the vector of input parameters $\boldsymbol{\theta}$ impact QoIs extracted from the solutions of RODEs. To this end, we propose two derivative-based global sensitivity measures (DGSMs). Let $y(t, \boldsymbol{\theta}, \omega)$ represent the quantity of interest (QoI) and consider

1. Global-in-time DGSMs for ω -averaged model:

$$v_j^{(1)} = \int_0^T \int_{\Theta} \left(\frac{\partial Y}{\partial \theta_j} \right)^2 \mu(d\boldsymbol{\theta}) dt, \quad \text{where } Y(t, \boldsymbol{\theta}) = \int_{\Omega} y(t, \boldsymbol{\theta}, \omega) P(d\omega). \quad (7.13)$$

2. Global-in-time stochastic DGSMs:

$$v_j^{(2)}(\omega) = \int_0^T \int_{\Theta} \left(\frac{\partial y}{\partial \theta_j} \right)^2 \mu(d\theta) dt. \quad (7.14)$$

The proposed DGSMs consider the sensitivity of different properties of the QoI. In the case of $v_j^{(1)}$ we take partial derivatives *after* averaging over the stochastic variable. In other words, $v_j^{(1)}$ considers the sensitivity of the average stochastic behavior of the model. In contrast, $v_j^{(2)}$ considers the sensitivity of the process pathwise, i.e, ω by ω . In section 7.5 we compare the DGSMs numerically.

7.4.3 Analytical investigations of $v_j^{(1)}$

In this section, we analytically compute the expectation of the QoI $\mathbf{x}(t, \boldsymbol{\theta}, \omega)$ from (7.11) with respect to the stochastic variable. We then use the results to gain insight into the behavior of the proposed measure $v_j^{(1)}$.

We have [113],

$$\mathbf{x}(t, \boldsymbol{\theta}, \omega) = e^{t\mathbf{A}}\mathbf{X}_0 + e^{t\mathbf{A}} \int_0^t e^{-s\mathbf{A}} \mathbf{z}(s, \boldsymbol{\theta}, \omega) ds, \quad \text{where } \mathbf{X}_0 = \mathbf{x}(0) \quad (7.15)$$

Consider $E_{\Omega} \{\mathbf{x}(t, \boldsymbol{\theta}, \omega)\}$,

$$E_{\Omega} \{\mathbf{x}(t, \boldsymbol{\theta}, \omega)\} = \int_{\Omega} e^{t\mathbf{A}}\mathbf{X}_0 P(d\omega) + e^{t\mathbf{A}} \int_{\Omega} \int_0^t e^{-s\mathbf{A}} \mathbf{z}(s, \boldsymbol{\theta}, \omega) ds P(d\omega) \quad (7.16)$$

$$= e^{t\mathbf{A}}\mathbf{X}_0 + L_0 e^{t\mathbf{A}} \int_0^t e^{-s\mathbf{A}} \int_{\Omega} L(s, \boldsymbol{\theta}, \omega) \mathbf{e}_1 P(d\omega) ds, \quad (7.17)$$

where \mathbf{e}_1 is the canonical basis vector in \mathbb{R}^3 . The change in the order of the integrals is justified by the Fubini-Tonelli Theorem.

We continue our analytic exploration by substituting the expectation of the noise term with respect to Ω with the known mean of each of the processes. We first consider the case when $L(t, \boldsymbol{\theta}, \omega)$ is modeled via GBM (7.5). Let $b = \mu + \sigma^2/2$:

$$\begin{aligned} E_{\Omega} \{\mathbf{x}(t, \boldsymbol{\theta}, \omega)\} &= e^{t\mathbf{A}}\mathbf{X}_0 + e^{t\mathbf{A}} \int_0^t L_0 e^{bs} e^{-s\mathbf{A}} \mathbf{e}_1 ds \\ &= e^{t\mathbf{A}}\mathbf{X}_0 + L_0 e^{t\mathbf{A}} \int_0^t e^{-s(\mathbf{A}-b\mathbf{I})} \mathbf{e}_1 ds \\ &= e^{t\mathbf{A}}\mathbf{X}_0 + L_0 e^{t\mathbf{A}} \left[-(\mathbf{A}-b\mathbf{I})^{-1} e^{-s(\mathbf{A}-b\mathbf{I})} \Big|_0^t \mathbf{e}_1 \right] \\ &= e^{t\mathbf{A}}\mathbf{X}_0 + L_0 e^{t\mathbf{A}} \left[-(\mathbf{A}-b\mathbf{I})^{-1} e^{-t(\mathbf{A}-b\mathbf{I})} + (\mathbf{A}-b\mathbf{I})^{-1} \right] \mathbf{e}_1 \\ &= e^{t\mathbf{A}}\mathbf{X}_0 + -L_0 e^{t\mathbf{A}} \left[e^{-t(\mathbf{A}-b\mathbf{I})} (\mathbf{A}-b\mathbf{I})^{-1} - (\mathbf{A}-b\mathbf{I})^{-1} \right] \mathbf{e}_1 \end{aligned}$$

$$\begin{aligned}
&= e^{t\mathbf{A}}\mathbf{X}_0 + -L_0 e^{t\mathbf{A}} \left[e^{-t(\mathbf{A}-b\mathbf{I})} - \mathbf{I} \right] (\mathbf{A} - b\mathbf{I})^{-1} \mathbf{e}_1 \\
&= e^{t\mathbf{A}}\mathbf{X}_0 + -L_0 \left[e^{bt}\mathbf{I} - e^{t\mathbf{A}} \right] (\mathbf{A} - b\mathbf{I})^{-1} \mathbf{e}_1 \\
&= e^{t\mathbf{A}}\mathbf{X}_0 + -L_0 \left[e^{(\mu+\sigma^2/2)t}\mathbf{I} - e^{t\mathbf{A}} \right] (\mathbf{A} - (\mu + \sigma^2/2)\mathbf{I})^{-1} \mathbf{e}_1.
\end{aligned}$$

Now, consider the special case when $\mu = -\sigma^2/2$, i.e. no drift. We can then simplify further

$$\mathbb{E}_\Omega \{\mathbf{x}(t, \boldsymbol{\theta}, \omega)\} = e^{t\mathbf{A}}\mathbf{X}_0 - L_0 \left[\mathbf{I} - e^{t\mathbf{A}} \right] \mathbf{A}^{-1} \mathbf{e}_1. \quad (7.18)$$

Observe, in (7.18) the parameter σ has vanished from the expression completely.

Next, consider the case when $L(t, \boldsymbol{\theta}, \omega)$ is modeled via the OU process (7.8). Starting from line (7.17) and substituting the known mean of the OU process we have

$$\begin{aligned}
\mathbb{E}_\Omega \{\mathbf{x}(t, \boldsymbol{\theta}, \omega)\} &= \\
&e^{t\mathbf{A}}\mathbf{X}_0 + L_0 e^{t\mathbf{A}} \int_0^t e^{-s\mathbf{A}} \left(L_0 e^{-ks} + \mu(1 - e^{-ks}) \right) \mathbf{e}_1 ds \\
&= e^{t\mathbf{A}}\mathbf{X}_0 + L_0 e^{t\mathbf{A}} \left[L_0 \int_0^t e^{-ks} e^{-s\mathbf{A}} ds + \mu \int_0^t e^{-s\mathbf{A}} ds - \mu \int_0^t e^{-ks} e^{-s\mathbf{A}} ds \right] \mathbf{e}_1 \\
&= e^{t\mathbf{A}}\mathbf{X}_0 + L_0 e^{t\mathbf{A}} \left[L_0 \int_0^t e^{-s(k\mathbf{I} + \mathbf{A})} ds + \mu \int_0^t e^{-s\mathbf{A}} ds - \mu \int_0^t e^{-s(k\mathbf{I} + \mathbf{A})} ds \right] \mathbf{e}_1 \\
&= e^{t\mathbf{A}}\mathbf{X}_0 + L_0 e^{t\mathbf{A}} \left[L_0 \left(- (k\mathbf{I} + \mathbf{A})^{-1} e^{-t(k\mathbf{I} + \mathbf{A})} + (k\mathbf{I} + \mathbf{A})^{-1} \right) \right. \\
&\quad \left. + \mu \left(- \mathbf{A}^{-1} e^{-t\mathbf{A}} + \mathbf{A}^{-1} \right) - \mu \left(- (k\mathbf{I} + \mathbf{A})^{-1} e^{-t(k\mathbf{I} + \mathbf{A})} + (k\mathbf{I} + \mathbf{A})^{-1} \right) \right] \mathbf{e}_1 \\
&= e^{t\mathbf{A}}\mathbf{X}_0 + L_0 e^{t\mathbf{A}} \left[L_0 \left(- e^{-t(k\mathbf{I} + \mathbf{A})} (k\mathbf{I} + \mathbf{A})^{-1} + (k\mathbf{I} + \mathbf{A})^{-1} \right) \right. \\
&\quad \left. + \mu \left(- e^{-t\mathbf{A}} \mathbf{A}^{-1} + \mathbf{A}^{-1} \right) - \mu \left(- e^{-t(k\mathbf{I} + \mathbf{A})} (k\mathbf{I} + \mathbf{A})^{-1} + (k\mathbf{I} + \mathbf{A})^{-1} \right) \right] \mathbf{e}_1 \\
&= e^{t\mathbf{A}}\mathbf{X}_0 + L_0 \left[L_0 \left(- e^{-kt} (k\mathbf{I} + \mathbf{A})^{-1} + e^{t\mathbf{A}} (k\mathbf{I} + \mathbf{A})^{-1} \right) \right. \\
&= e^{t\mathbf{A}}\mathbf{X}_0 + L_0 \left[L_0 \left(- e^{-kt} (k\mathbf{I} + \mathbf{A})^{-1} + e^{t\mathbf{A}} (k\mathbf{I} + \mathbf{A})^{-1} \right) \right. \\
&\quad \left. - \mu \left(- e^{-kt} (k\mathbf{I} + \mathbf{A})^{-1} + e^{t\mathbf{A}} (k\mathbf{I} + \mathbf{A})^{-1} \right) - \mu \left(\mathbf{A}^{-1} - e^{t\mathbf{A}} \mathbf{A}^{-1} \right) \right] \mathbf{e}_1 \\
&= e^{t\mathbf{A}}\mathbf{X}_0 + L_0 \left[L_0 \left(- e^{-kt} (k\mathbf{I} + \mathbf{A})^{-1} + e^{t\mathbf{A}} (k\mathbf{I} + \mathbf{A})^{-1} \right) \right. \\
&\quad \left. + \mu \left(e^{-kt} (k\mathbf{I} + \mathbf{A})^{-1} - e^{t\mathbf{A}} (k\mathbf{I} - \mathbf{A})^{-1} \right) - \mu \left(\mathbf{A}^{-1} - e^{t\mathbf{A}} \mathbf{A}^{-1} \right) \right] \mathbf{e}_1
\end{aligned}$$

$$\begin{aligned}
&= e^{t\mathbf{A}}\mathbf{X}_0 + L_0 \left[\left((\mu - L_0)e^{-kt}\mathbf{I} + (L_0 - \mu)e^{t\mathbf{A}} \right) (k\mathbf{I} + \mathbf{A})^{-1} - \mu (\mathbf{I} - e^{t\mathbf{A}})\mathbf{A}^{-1} \right] \mathbf{e}_1 \\
&= e^{t\mathbf{A}}\mathbf{X}_0 + L_0 \left[\left((\mu - L_0) \left(e^{-kt}\mathbf{I} - e^{t\mathbf{A}} \right) \right) (k\mathbf{I} + \mathbf{A})^{-1} - \mu (\mathbf{I} - e^{t\mathbf{A}})\mathbf{A}^{-1} \right] \mathbf{e}_1. \quad (7.19)
\end{aligned}$$

Note, the parameter σ has been eliminated once again. The next step in computing $v_j^{(1)}$ is to evaluate the partial derivatives with respect to the uncertain parameters (7.10). In the case of both GBM and OU noise, it is straightforward to see that the partial derivative with respect to σ will be zero. This means, $v_j^{(1)}$ will *always* rank σ as unimportant.

7.5 Numerical results

In this section we investigate the DGSMs proposed in 7.4.2 to analyze their utility for identifying non-essential model variables. We consider the system in (7.11) describing lead transfer in the human body. We focus our investigation on the QoI $x_1(t, \boldsymbol{\theta}, \omega)$, which represents the amount of lead in the blood at time t . We estimate the DGSMs to analyze the sensitivity of x_1 in two different setups. Specifically, we consider the case when the stochastic forcing term $L(t, \boldsymbol{\theta}, \omega)$ is modeled with a GBM (section 7.5.1) and when $L(t, \boldsymbol{\theta}, \omega)$ is modeled with an OU process (section 7.5.2). In both cases The MATLAB package Chebfun is used to simulate realizations of the stochastic forcing term using a wave number of $\lambda = 10$ (section 7.4.1).

Estimating the proposed DGSMs. We first explain the different approaches implemented to numerically estimate the DGSMs. Let $Y(t, \boldsymbol{\theta}) = \int_{\Omega} x_1(t, \omega, \boldsymbol{\theta}) P(d\omega)$. To compute $v_j^{(1)}$ (7.13) we approximate Y using a Monte Carlo (MC) estimate with N_{Ω} samples of x_1 . All solutions for x_1 are computed via ode45. The partial derivatives $\frac{\partial Y}{\partial \theta_j}$, $j = 1, \dots, N_p$ are computed using a complex-step method with step size $h = 0.01$. Next, we use N_{Θ} samples to approximate the integral of Θ . Lastly, the composite trapezoid rule is used to evaluate the integral over the time domain $\mathcal{T} = [0 \ T_f]$. To estimate $v_j^{(2)}(\omega)$ (7.14) we construct the corresponding sensitivity equations [68, 93] to compute the partial derivatives $\frac{\partial x_1}{\partial \theta_j}$, $j = 1, \dots, N_p$. The resulting augmented system is solved using ode45. We utilize N_{Θ} samples of the input parameters to approximate the integral over the uncertain parameter space. Finally, we integrate over the time using composite trapezoid rule.

7.5.1 Derivative-based GSA for the GBM forcing term

We focus on simulations of the system in (7.11) forced by a GBM with $\mu = -\sigma^2/2$, i.e. no drift. Recall, the uncertain parameter is given as $\boldsymbol{\theta} \in \mathbb{R}^8$, with $\boldsymbol{\theta} = [U \ k_{12} \ k_{21} \ k_{13} \ k_{31} \ S \ L_0 \ \sigma]$. The model is simulated on the time interval $\mathcal{T} = [0 \ 365]$ days. A few realizations the GBM representations of the forcing term $L(t, \omega, \boldsymbol{\theta})$ are displayed in Figure 7.6 (left). The corresponding QoI realizations are displayed in Figure 7.6 (right). We utilize $N_{\Omega} = 1,000$ and $N_{\Theta} = 500$ to

estimate $\nu_j^{(1)}$ and $\nu_j^{(2)}$ and normalize the resulting values as follows

$$\bar{\nu}_j^{(i)} = \frac{\nu_j^{(i)}}{\sum_{k=1}^{N_p} \nu_k^{(i)}}, \quad i = 1, 2.$$

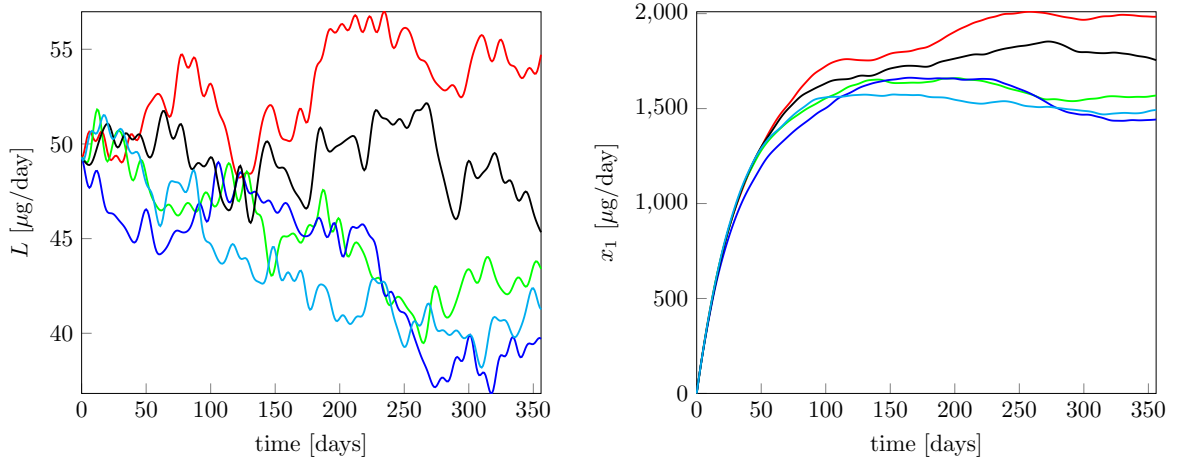


Figure 7.6 Left: a few realizations of the noise term L constructed with a GBM, right: corresponding trajectories of x_1 .

In Figure 7.7 we display pdf estimates for $\bar{\nu}_j^{(2)}$ computed with $N_\Omega = 1,000$ samples. Observe, all of the pdf estimates are skewed. In order to compare $\bar{\nu}_j^{(2)}$ with $\bar{\nu}_j^{(1)}$ we compute the median of the $\bar{\nu}_j^{(2)}$ pdfs as well as the 10th and 90th percentiles. We display these results alongside $\bar{\nu}_j^{(1)}$ in Figure 7.8. We choose an importance tolerance of $tol = 0.05$ and use the convention that a $\bar{\nu}_j^{(i)}$, $i = 1, 2$ value below tol implies the corresponding parameter θ_j is unimportant. We observe that in the case of θ_4 in Figure 7.8 the tol falls within the 90th percentile of $\bar{\nu}_j^{(2)}$. This means that $\bar{\nu}_j^{(2)}$ unimportance rankings of this parameter *changes with the realizations of ω* .

We also note the two DGSMs report similar values for every input parameter, *except* θ_8 . Recall, from the investigation in section 7.4.3 that the partial derivative of $Y(t, \theta)$ with respect to θ_8 is zero because Y does not depend on θ_8 . Thus, the result $\bar{\nu}_8^{(1)} = 0$ provides a numerical illustration of the analytic derivation from the previous section. In comparison, the median value for $\bar{\nu}_8^{(2)}$ is above 0.1. This disparity between $\bar{\nu}_8^{(1)}$ and $\bar{\nu}_8^{(2)}$ is further illustration of the subtleties involved in stochastic sensitivity analysis. By averaging over the stochastic variable first $\nu_j^{(1)}$ is reduced to the deterministic case when $L = E_\Omega \{L\}$. Therefore, with $\nu_j^{(1)}$ we are analyzing the impact of parameters on the average behavior of the QoI. In contrast, $\nu_j^{(2)}$ accounts the possible impact of the different realizations of the stochastic noise by returning

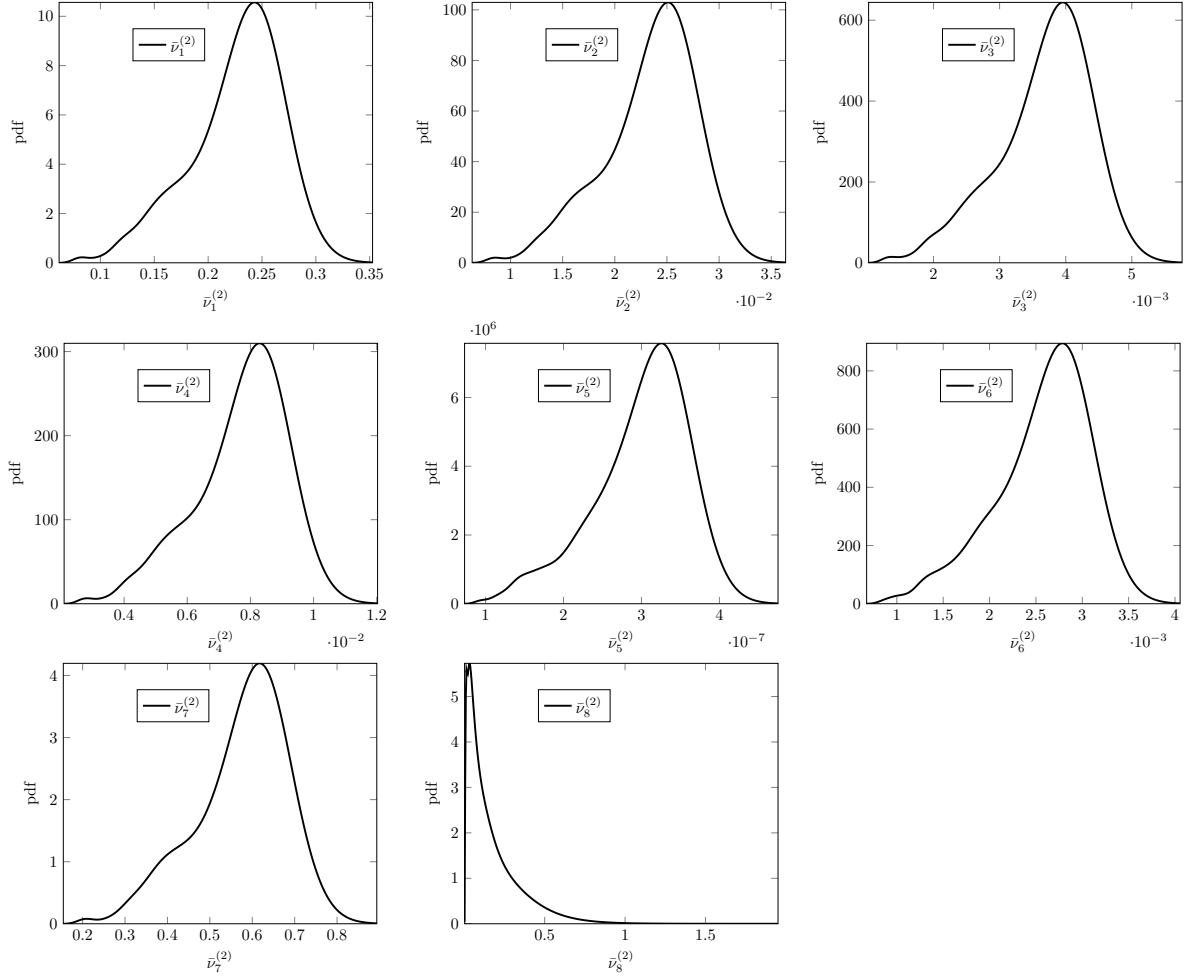


Figure 7.7 Estimated pdfs for $\bar{\nu}_j^{(2)}$, $j = 1, \dots, N_p$, computed with $N_\Omega = 1,000$ samples.

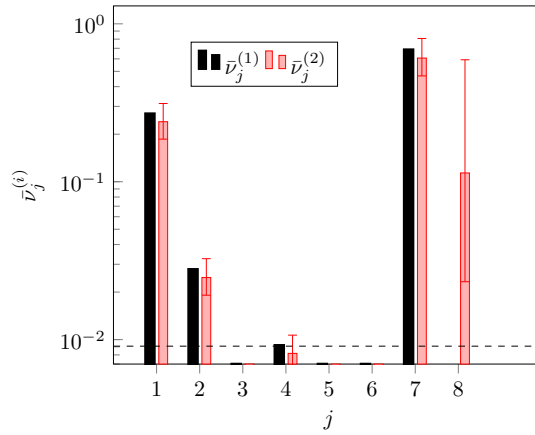


Figure 7.8 Comparison of normalized DGSMs $\bar{\nu}_j^{(1)}$ (black) and median of $\bar{\nu}_j^{(2)}$ (red) estimated for x_1 with GBM forcing term. Dashed line corresponds to $tol = 0.05$.

a distribution of parameter sensitivities. Put another way, $v_j^{(2)}$ tells us that the sensitivity of the QoI to σ depends on the realization of the noise, and $v_j^{(1)}$ tells us that the stochastic average value of the QoI is not sensitive to σ . Which DGSM we choose depends on the sensitivity information we are interested in.

7.5.2 Derivative-based GSA for the OU forcing term

In this section we consider the same uncertain parameter as the previous study in the case when the system in (7.11) is forced by an OU process (7.7), with noise parameter values $\mu = 35\mu\text{g}$ and $k = 0.2$. A few realization of the OU process and corresponding QoI are displayed in Figure 7.9 left and middle, respectively. No simplifying assumptions are made for the OU noise case.

For this study we modify the numerical approach utilized for $v_j^{(1)}$. Specifically, we replace the MC estimate of $Y(t, \theta)$ with the analytical formula given in (7.19). All other numerical procedures remain the same. We utilize sample sizes $N_\Omega = 500$ and $N_\Theta = 80$ for the computations of $v_j^{(1)}$ and $v_j^{(2)}$. In Figure 7.9 (right) we compare the normalized values of $\bar{v}_j^{(1)}$ (black) and the sample median of $\bar{v}_j^{(2)}$ (red). We use the importance tolerance $tol = 0.007$. Note, the two proposed DGSMs once again rank the first seven parameters similarly and disagree for θ_8 , as expected.

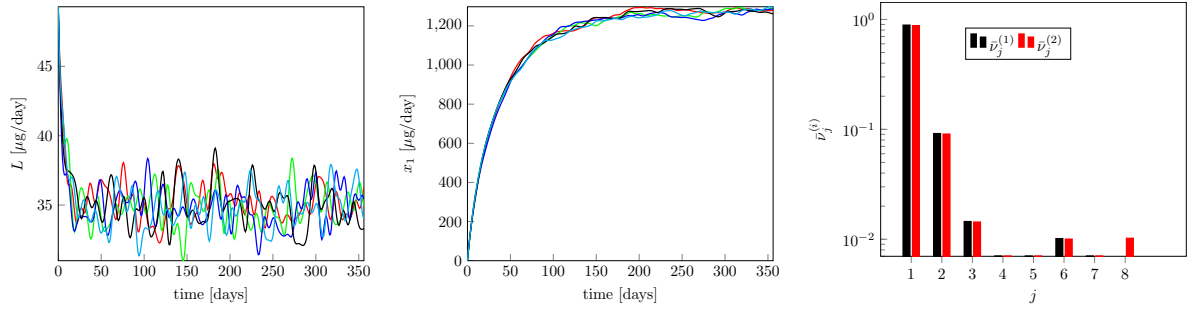


Figure 7.9 Left: a few realizations of the noise term L constructed with the OU process, middle: corresponding trajectories of x_1 , right: comparison of normalized DGSMs for $\bar{v}_j^{(1)}$ (black) and median of $\bar{v}_j^{(2)}$ (red) estimated for x_1 with OU forcing term. Results above 7×10^{-3} displayed only.

7.6 Conclusion

In this chapter we demonstrated the need for careful treatment of derivative-based global sensitivity analysis for stochastically forced ordinary differential equations. We also discussed a straight-forward, easy-to-implement numerical approach for solving RODEs that enables the use of traditional numerical methods for solving ordinary differential equations.

We proposed two different DGSMs, each considering the sensitivity of a different aspect

of the QoI. In the case of $\nu_j^{(1)}$, we are analyzing sensitivity of the *average* stochastic behavior of the QoI with respect to the uncertain parameters. Since we are averaging over the stochastic behavior first and then evaluating sensitivity, there is potential for loss of information. In comparison, $\nu_j^{(2)}$ considers sensitivity of the process to the uncertain parameters as a function of ω . This means that while we are analyzing the sensitivity of the full process, parameter importance can change depending on the noise realization. Therefore, the appropriate DGSM formulation depends on the QoI behavior we want to analyze. We computed and compared the two DGSMs for an RODE describing lead in the body. In spite of measuring different quantities, the proposed DGSMs gave similar rankings for many of the input variables. However, the DGSMs did not agree for every uncertain parameter.

Future work should seek to formalize under what circumstances $\nu_j^{(1)}$ parameter rankings are consistent with those of $\nu_j^{(2)}$. Analysis of other types of RODEs (random coefficients or random initial conditions), as well as a nonlinear system of RODEs would also provide further insight into derivative-based GSA for stochastic systems.

In this thesis we studied GSA methods for a variety of QoI types. In chapter 3, we generalized derivative-based GSA approaches and properties to the case of vector-valued outputs. In chapter 4, we presented methods for derivative-based global sensitivity measures (DGSMs) for functional QoIs. In chapter 6, we proposed a parameter screening metric inspired by active subspace methods for functional QoIs. Lastly, in chapter 7, we proposed and investigated two possible DGSMs for the case of stochastic QoIs.

Computational efficiency was central in the development of our numerical methods. In chapter 4, the truncated Karhunen–Loève expansion (KLE) is combined with adjoint-based gradient computation to obtain a numerical approach for computing the functional DGSMs for which the computational cost did not scale with the input parameter dimension. In chapter 6, we presented a structure exploiting, gradient-free, non-intrusive framework for efficient dimension reduction and surrogate modeling for models with high-dimensional inputs and outputs. In chapter 7, the proposed computational methods that used smooth approximations of the stochastic forcing terms which allowed traditional numerical ODE solutions methods to be used while retaining known convergence rates.

We utilized our proposed GSA methods by studying QoIs arising from a wide variety of applications, including disease modeling, subsurface flow, and biotransport. The presented numerical results illustrate that our proposed GSA methods and corresponding computational approaches are efficient and informative.

Future work for chapter 4 could develop extensions for derivative-based GSA for function-valued QoIs with correlated parameters. While the proposed numerical methods for estimating the functional DGSMs do not rely on parameter independence, the relationship between DGSMs and the total Sobol’ indices fails in the case of correlated parameters.

The computational approaches proposed in chapters 4 and 6 rely on effectively approxi-

imating the functional QoI with a low-rank KLE. However, in some cases, one might require considerably more terms in the truncated KLE to approximate the true process well. Future work should seek to develop numerical methods for computing the proposed GSA methods for QoIs that cannot be sufficiently estimated via low-rank KLEs.

A future direction for the parameter screening method proposed in chapter 6 could investigate different approaches for approximating the active subspace and activity scores. Additionally, the bispectral surrogates in chapter 6 model the KL modes using polynomial chaos expansions. One could explore alternative surrogate modeling techniques for the KL modes, such as multivariate adaptive regression splines (MARS) or neural networks, to determine their suitability.

BIBLIOGRAPHY

- [1] 2001 SPE Comparative Solution Project. <https://www.spe.org/web/csp/datasets/set02.htm>. Accessed: September 19, 2018. 2000.
- [2] R. J. Adler. *The geometry of random fields*. SIAM, 2010.
- [3] A. Alexanderian. “On spectral methods for variance based sensitivity analysis”. *Probab. Surv.* **10** (2013), pp. 51–68.
- [4] A. Alexanderian, J. Winokur, I. Sraj, A. Srinivasan, M. Iskandarani, W. Thacker & O. Knio. “Global Sensitivity Analysis in Ocean Global Circulation Models: A Sparse Spectral Projection Approach”. *Computational Geosciences* **16.3** (2012), pp. 757–778.
- [5] A. Alexanderian, L. Zhu, M. Salloum, R. Ma & M. Yu. “Investigation of biotransport in a tumor with uncertain material properties using a non-intrusive spectral uncertainty quantification method”. *J. Biomech. Eng.* (2017), pp. 091006–1–091006–11.
- [6] A. Alexanderian, P. Gremaud & R. Smith. “Variance-based sensitivity analysis for time-dependent processes”. *Reliability Engineering & System Safety* (2020).
- [7] A. Alexanderian, W. Reese, R. C. Smith & M. Yu. “Efficient uncertainty quantification for biotransport in tumors with uncertain material properties”. In: *ASME 2018 International Mechanical Engineering Congress and Exposition*. American Society of Mechanical Engineers. 2018, V003T04A033–V003T04A033.
- [8] O. Angelini, C. Chavant, E. Chénier, R. Eymard & S. Granet. “Finite volume approximation of a diffusion-dissolution model and application to nuclear waste storage”. *Math. Comput. Simul.* **81.10** (2011), pp. 2001–2017.
- [9] B. Auder & B. Iooss. “Global sensitivity analysis based on entropy”. In: *Safety, reliability and risk analysis-Proceedings of the ESREL 2008 Conference*. 2008, pp. 2107–2115.
- [10] M. S. B. Mansour Dia B. Saad. “Modeling and simulation of partially miscible two-phase flow with kinetics mass transfer”. *Mathematics and Computers in Simulation* (2020).
- [11] M. Bennett, D. Volfson, L. Tsimring & J. Hasty. “Transient Dynamics of Genetic Regulatory Networks”. *Biophysical Journal* **92.10** (2007), pp. 3501–3512.
- [12] E. van den Berg & M. P. Friedlander. *spg1: A solver for large-scale sparse reconstruction*. 2007.
- [13] W. Betz, I. Papaioannou & D. Straub. “Numerical methods for the discretization of random fields by means of the Karhunen–Loève expansion”. *Computer Methods in Applied Mechanics and Engineering* **271** (2014), pp. 109–129.
- [14] R. Bhatia & C. Davis. “A better bound on the variance”. *Amer. Math. Monthly* **107.4** (2000), pp. 353–357.

- [15] G. Blatman & B. Sudret. "Efficient computation of global sensitivity indices using sparse polynomial chaos expansions". *Reliability Engineering & System Safety* **95.11** (2010), pp. 1216–1229.
- [16] E. Borgonovo. "A new uncertainty importance measure". *Reliability Engineering & System Safety* **92.6** (2007), pp. 771–784.
- [17] E. Borgonovo & B. Iooss. "Moment independent and reliability-based importance measures" (2016).
- [18] A. Bourgeat, S. Granet & F. Smaï. "Compositional two-phase flow in saturated unsaturated porous media: benchmarks for phase appearance/disappearance". *Radon Series on Computational and Applied Mathematics: Simulation of Flow in Porous Media* (2012).
- [19] A. Bourgeat, M. Jurak & F. Smaï. "Two-phase, partially miscible flow and transport modeling in porous media; application to gaz migration in a nuclear waste repository". *Computational Geosciences* **6** (2009), pp. 309–325.
- [20] K. Campbell, M. D. McKay & B. J. Williams. "Sensitivity analysis when model outputs are functions". *Reliability Engineering & System Safety* **91.10-11** (2006), pp. 1468–1472.
- [21] K. Chenoweth, A. C. Van Duin & W. A. Goddard. "ReaxFF reactive force field for molecular dynamics simulations of hydrocarbon oxidation". *The Journal of Physical Chemistry A* **112.5** (2008), pp. 1040–1053.
- [22] M. Christie, V. Demyanov & D. Erbas. "Uncertainty quantification for porous media flows". *Journal of Computational Physics* **217.1** (2006), pp. 143–158.
- [23] W. H. Clark. "Tumour progression and the nature of cancer". *Br J Cancer* **64** (1991).
- [24] W. H. Clark. "Biphasic finite element model of solute transport for direct infusion into nervous tissue". *Annals of Biomedical Engineering* **35** (2007), pp. 2145–2158.
- [25] H. Cleaves, A. Alexanderian, H. Guy, R. C. Smith & M. Yu. "Derivative-Based Global Sensitivity Analysis for Models with High-Dimensional Inputs and Functional Outputs". *SIAM Journal on Scientific Computing* **41** (2019), A3524–A3551.
- [26] H. Cleaves, A. Alexanderian & B. Saad. "Structure exploiting methods for fast uncertainty quantification in multiphase flow through heterogeneous media". *arXiv preprint arXiv:2008.11274* (2020).
- [27] P. G. Constantine. *Active subspaces*. Vol. 2. SIAM Spotlights. Emerging ideas for dimension reduction in parameter studies. Society for Industrial and Applied Mathematics (SIAM), Philadelphia, PA, 2015.
- [28] P. G. Constantine & P. Diaz. "Global sensitivity metrics from active subspaces". *Reliability Engineering & System Safety* **162** (2017), pp. 1–13.

- [29] P. G. Constantine, E. Dow & Q. Wang. "Active subspace methods in theory and practice: applications to kriging surfaces". *SIAM Journal on Scientific Computing* **36.4** (2014), A1500–A1524.
- [30] A. Costa. "Permeability-porosity relationship: A reexamination of the Kozeny-Carman equation based on a fractal pore-space geometry assumption". *Geophysical research letters* **33.2** (2006).
- [31] T. Crestaux, O. Le Maître & J.-M. Martinez. "Polynomial chaos expansion for sensitivity analysis". *Reliability Engineering & System Safety* **94.7** (2009), pp. 1161–1172.
- [32] B. Debusschere. *Uncertainty Quantification Toolkit*. Tech. rep. Sandia National Lab.(SNL-NM), Albuquerque, NM (United States), 2017.
- [33] B. J. Debusschere, H. N. Najm, P. P. Pébay, O. M. Knio, R. G. Ghanem & O. P. Le Maître. "Numerical challenges in the use of polynomial chaos representations for stochastic processes". *SIAM journal on scientific computing* **26.2** (2004), pp. 698–719.
- [34] T. A. Driscoll, N. Hale, L. N. Trefethen & editors. *Chebfun Guide*. <https://www.chebfun.org/>. 2014.
- [35] R. Durrett. *Probability: theory and examples*. Vol. 49. Cambridge university press, 2019.
- [36] E. Batschelet, L. Brand & A. Steiner. "On the Kinetics of Lead in the Human Body". *Journal of Mathematical Biology* **8** (1979), pp. 15–23.
- [37] N. Fajraoui, S. Marelli & B. Sudret. "Sequential Design of Experiment for Sparse Polynomial Chaos Expansions". *SIAM/ASA Journal on Uncertainty Quantification* **5.1** (2017), pp. 1061–1085.
- [38] S. Filip, A. Javeed & L. N. Trefethen. "Smooth Random Functions, Random ODEs, and Gaussian Processes". *SIAM Review* **61** (2019), pp. 185–205.
- [39] G. B. Folland. *Real analysis*. Second. Pure and Applied Mathematics (New York). Modern techniques and their applications, A Wiley-Interscience Publication. John Wiley & Sons, Inc., New York, 1999.
- [40] J. H. Friedman. "Multivariate adaptive regression splines". *The Annals of Statistics* **19.1** (1991). With discussion and a rejoinder by the author, pp. 1–141.
- [41] F. Gamboa, A. Janon, T. Klein, A. Lagnoux, et al. "Sensitivity analysis for multidimensional and functional outputs". *Electronic Journal of Statistics* **8.1** (2014), pp. 575–603.
- [42] L. L. Gratiet, S. Marelli & B. Sudret. "Metamodel-based sensitivity analysis: polynomial chaos expansions and Gaussian processes". In: *Handbook of Uncertainty Quantification*. Ed. by R. Ghanem, D. Higdon & H. Owhadi. Springer, 2017.
- [43] Z. J. Grey & P. G. Constantine. "Active subspaces of airfoil shape parameterizations". *AIAA Journal* **56.5** (2018), pp. 2003–2017.

- [44] L. Grüne & P. E. Kloeden. "Pathwise Approximation of Random Ordinary Differential Equations". *BIT Numerical Mathematics* **41.4** (2001), pp. 711–721.
- [45] H. Guy, A. Alexanderian & M. Yu. "A distributed active subspace method for scalable surrogate modeling of function valued outputs". *Journal of Scientific Computing* **85.2** (2020), pp. 1–25.
- [46] J. Hart, A. Alexanderian & P. Gremaud. "Efficient computation of Sobol' indices for stochastic models". *SIAM J. Sci. Comput.* **39.4** (2017), A1514–A1530.
- [47] J. Hart, P. Gremaud & T David. "Global sensitivity analysis of high-dimensional neuroscience models: An example of neurovascular coupling". *Bulletin of mathematical biology* **81.6** (2019), pp. 1805–1828.
- [48] J. Hart & P. A. Gremaud. "An approximation theoretic perspective of Sobol' indices with dependent variables". *International Journal for Uncertainty Quantification* **8.6** (2018).
- [49] J. Hart & P. A. Gremaud. "Robustness of the Sobol' indices to distributional uncertainty". *International Journal for Uncertainty Quantification* **9.5** (2019).
- [50] J. L. Hart & P. A. Gremaud. "Robustness of the Sobol' indices to marginal distribution uncertainty". *SIAM/ASA Journal on Uncertainty Quantification* **7.4** (2019), pp. 1224–1244.
- [51] D. M. Hartley, J. G. J. Morris & D. L. Smith. "Hyperinfectivity: a critical element in the ability of *V. cholerae* to cause epidemics?" *PLoS medicine* **3.1** (2005).
- [52] T. Hsing & R. Eubank. *Theoretical foundations of functional data analysis, with an introduction to linear operators*. John Wiley & Sons, 2015.
- [53] B. Iooss & P. Lemaître. "A review on global sensitivity analysis methods". In: *Uncertainty management in simulation-optimization of complex systems*. Springer, 2015, pp. 101–122.
- [54] W. Ji, J. Wang, O. Zahm, Y. M. Marzouk, B. Yang, Z. Ren & C. K. Law. "Shared low-dimensional subspaces for propagating kinetic uncertainty to multiple outputs". *Combustion and Flame* **190** (2018), pp. 146–157.
- [55] P. E. Kloeden & E. Platen. *Numerical solution of stochastic differential equations*. Vol. 23. Springer Science & Business Media, 2013.
- [56] R. Kress. *Linear Integral Equations*. third. Springer-Verlag New York, 2014, pp. 224–449.
- [57] S Kucherenko, M. Rodriguez-Fernandez, C Pantelides & N. Shah. "Monte Carlo evaluation of derivative-based global sensitivity measures". *Reliability Engineering & System Safety* **94.7** (2009), pp. 1135–1148.
- [58] S. Kucherenko & I. Sobol. "A new derivative based importance criterion for groups of variables and its link with the global sensitivity indices". *Computer Physics Communications* **181.7** (2010), pp. 1212–1217.

- [59] S. Kucherenko & B. Iooss. "Derivative-based global sensitivity measures". In: *Handbook of Uncertainty Quantification*. Ed. by R. Ghanem, D. Higdon & H. Owhadi. Springer, 2017.
- [60] M. Lamboni, B. Iooss, A.-L. Popelin & F. Gamboa. "Derivative-based global sensitivity measures: General links with Sobol' indices and numerical tests". *Mathematics and Computers in Simulation* **87** (2013), pp. 45–54.
- [61] M. Lamboni, H. Monod & D. Makowski. "Multivariate sensitivity analysis to measure global contribution of input factors in dynamic models". *Reliability Engineering & System Safety* **96.4** (2011), pp. 450–459.
- [62] P. D. Lax. *Functional Analysis*. John Wiley & Sons, 2002.
- [63] O. Le Maître & O. Knio. *Spectral Methods for Uncertainty Quantification: With Applications to Computational Fluid Dynamics*. Springer, 2010.
- [64] G. Li, M. Iskandarani, M. Le Hénaff, J. Winokur, O. P. Le Maître & O. M. Knio. "Quantifying initial and wind forcing uncertainties in the Gulf of Mexico". *Computational Geosciences* **20.5** (2016), pp. 1133–1153.
- [65] K.-A. Lie. *An introduction to reservoir simulation using MATLAB/GNU Octave: User guide for the MATLAB Reservoir Simulation Toolbox (MRST)*. Cambridge University Press, 2019.
- [66] M. Loève. *Probability theory. I*. Fourth. Graduate Texts in Mathematics, Vol. 45. Springer-Verlag, New York-Heidelberg, 1977, pp. xvii+425.
- [67] R. Ma, D. Su & L. Zhu. "Multiscale simulation of nanoparticle transport in deformable tissue during an infusion process in hyperthermia treatments of cancers." In: *Nanoparticle Heat Transfer and Fluid Flow, Computational & Physical Processes in Mechanics & Thermal Science Series*. Ed. by W. J. Minkowycz, E. Sparrow & J. P. Abraham. Vol. 4. CRC Press, Taylor & Francis Group, 2012.
- [68] T. Maly & L. R. Petzold. "Numerical methods and software for sensitivity analysis of differential-algebraic systems". *Applied Numerical Mathematics* **20.1-2** (1996), pp. 57–79.
- [69] A. Marrel, N. Saint-Geours & M. De Lozzo. "Sensitivity analysis of spatial and/or temporal phenomena". In: *Handbook of Uncertainty Quantification*. Ed. by R. Ghanem, D. Higdon & H. Owhadi. Springer, 2017.
- [70] MATLAB. *version 8.6.0.267246 (R2015b)*. Natick, Massachusetts, 2015.
- [71] J. Mercer. "Functions of positive and negative type, and their connection with the theory of integral equations". *Philosophical Transactions of the Royal Society of London. Series A, Containing Papers of a Mathematical or Physical Character* (1909), pp. 415–446.
- [72] M. D. Morris. "Factorial sampling plans for preliminary computational experiments". *Technometrics* **33.2** (1991), pp. 161–174.

- [73] H. N. Najm. "Uncertainty quantification and polynomial chaos techniques in computational fluid dynamics". *Annual review of fluid mechanics* **41** (2009), pp. 35–52.
- [74] A. Namhata, S. Oladyshkin, R. M. Dilmore, L. Zhang & D. V. Nakles. "Probabilistic assessment of above zone pressure predictions at a geologic carbon storage site". *Scientific reports* **6.1** (2016), pp. 1–12.
- [75] T. Neckel & F. Rupp. *Random differential equations in scientific computing*. Walter de Gruyter, 2013.
- [76] R. Neumann, P. Bastian & O. Ippisch. "Modeling and simulation of two-phase two-component flow with disappearing nonwetting phase". *Computational Geosciences* **17.1** (2012), pp. 139–149.
- [77] B. Oksendal. *Stochastic Differential Equations*. Springer-Verlag Berlin Heidelberg, 1998.
- [78] A. B. Owen. "Better estimation of small Sobol' sensitivity indices". *ACM Transactions on Modeling and Computer Simulation (TOMACS)* **23.2** (2013), pp. 1–17.
- [79] A. B. Owen. "Sobol' indices and Shapley value". *SIAM/ASA Journal on Uncertainty Quantification* **2.1** (2014), pp. 245–251.
- [80] A. B. Owen & C. Prieur. "On Shapley value for measuring importance of dependent inputs". *SIAM/ASA Journal on Uncertainty Quantification* **5.1** (2017), pp. 986–1002.
- [81] M. C. Pitman & A. C. Van Duin. "Dynamics of confined reactive water in smectite clay–zeolite composites". *Journal of the American Chemical Society* **134.6** (2012), pp. 3042–3053.
- [82] S. Plimpton. "Fast parallel algorithms for short-range molecular dynamics". *Journal of computational physics* **117.1** (1995), pp. 1–19.
- [83] E. Plischke, E. Borgonovo & C. L. Smith. "Global sensitivity measures from given data". *European Journal of Operational Research* **226.3** (2013), pp. 536–550.
- [84] C. Prieur & S. Tarantola. "Variance-based sensitivity analysis: Theory and estimation algorithms". In: *Handbook of Uncertainty Quantification*. Ed. by R. Ghanem, D. Higdon & H. Owhadi. Springer, 2017, pp. 1217–1239.
- [85] A. Rushdi & e. M.L. Parks, eds. *Global sensitivity driven input dimensionality reduction for ReaxFF parameterizations of silica-based glasses*. Vol. Technical Report SAND2020-12580R. Sandia National Laboratories, 2020, pp. 240–245.
- [86] B. M. Saad, A. Alexanderian, S. Prudhomme & O. M. Knio. "Probabilistic modeling and global sensitivity analysis for CO₂ storage in geological formations: a spectral approach". *Applied Mathematical Modelling* **53** (2018), pp. 584–601.
- [87] M. Salloum, R. Ma, D. Weeks & L. Zhu. "Controlling nanoparticle delivery in magnetic nanoparticle hyperthermia for cancer treatment: experimental study in agarose gel". *International Journal of Hyperthermia* **24** (2008), pp. 337–345.

- [88] A. Saltelli. "Making best use of model evaluations to compute sensitivity indices". *Computer physics communications* **145.2** (2002), pp. 280–297.
- [89] A. Saltelli, P. Annoni, I. Azzini, F. Campolongo, M. Ratto & S. Tarantola. "Variance based sensitivity analysis of model output. Design and estimator for the total sensitivity index". *Computer physics communications* **181.2** (2010), pp. 259–270.
- [90] A. Saltelli, K. Chan, E. M. Scott, et al. *Sensitivity analysis*. Vol. 1. Wiley New York, 2000.
- [91] A. Saltelli, M. Ratto, T. Andres, F. Campolongo, J. Cariboni, D. Gatelli, M. Saisana & S. Tarantola. *Global sensitivity analysis: the primer*. John Wiley & Sons, 2008.
- [92] A. Saltelli, S. Tarantola & K.-S. Chan. "A quantitative model-independent method for global sensitivity analysis of model output". *Technometrics* **41.1** (1999), pp. 39–56.
- [93] A. Sandu, D. N. Daescu & G. R. Carmichael. "Direct and adjoint sensitivity analysis of chemical kinetic systems with KPP: Part I theory and software tools". *Atmospheric Environment* **37.36** (2003), pp. 5083–5096.
- [94] K. Sargsyan. "Surrogate models for uncertainty propagation and sensitivity analysis". In: *Handbook of uncertainty quantification*. Ed. by R. Ghanem, D. Higdon & H. Owhadi. Springer, 2017.
- [95] E. S. Schwartz. "The stochastic behavior of commodity prices: Implications for valuation and hedging". *The Journal of finance* **52.3** (1997), pp. 923–973.
- [96] P. Seshadri, S. Shahpar, P. Constantine, G. Parks & M. Adams. "Turbomachinery active subspace performance maps". *Journal of Turbomachinery* **140.4** (2018).
- [97] G. Severino, S. Leveque & G. Toraldo. "Uncertainty quantification of unsteady source flows in heterogeneous porous media". *Journal of Fluid Mechanics* **870** (2019), pp. 5–26.
- [98] R. C. Smith. *Uncertainty quantification: theory, implementation, and applications*. Vol. 12. SIAM, 2013. Chap. 13.
- [99] I. Sobol. "Estimation of the sensitivity of nonlinear mathematical models". *Matematicheskoe Modelirovanie* **2.1** (1990), pp. 112–118.
- [100] I. Sobol. "Global sensitivity indices for nonlinear mathematical models and their Monte Carlo estimates". *Mathematics and Computers in Simulation* **55.1–3** (2001). The Second IMACS Seminar on Monte Carlo Methods, pp. 271–280.
- [101] I. Sobol' & S. Kucherenko. "Derivative based global sensitivity measures and their link with global sensitivity indices". *Mathematics and Computers in Simulation* **79.10** (2009), pp. 3009–3017.
- [102] I. Sobol, S. Tarantola, D. Gatelli, S. Kucherenko & W. Mauntz. "Estimating the approximation error when fixing unessential factors in global sensitivity analysis". *Reliability Engineering & System Safety* **92.7** (2007), pp. 957–960.

- [103] E. Song, B. L. Nelson & J. Staum. "Shapley effects for global sensitivity analysis: Theory and computation". *SIAM/ASA Journal on Uncertainty Quantification* **4.1** (2016), pp. 1060–1083.
- [104] B. Sudret. "Global sensitivity analysis using polynomial chaos expansions". *Reliability Engineering & System Safety* **93.7** (2008), pp. 964–979.
- [105] S. Tarantola & T. A. Mara. "Variance-based sensitivity indices of computer models with dependent inputs: The Fourier Amplitude Sensitivity Test". *International Journal for Uncertainty Quantification* **7.6** (2017).
- [106] A. C. Van Duin, S. Dasgupta, F. Lorant & W. A. Goddard. "ReaxFF: a reactive force field for hydrocarbons". *The Journal of Physical Chemistry A* **105.41** (2001), pp. 9396–9409.
- [107] A. C. Van Duin, W. Goddard, M. Islam, H Van Schoot, T Trnka & A. Yakovlev. *ReaxFF 2019.3*, SCM.
- [108] H. Xiao & L. Li. "Discussion of paper by Matieyendou Lamboni, Hervé Monod, David Makowski Multivariate sensitivity analysis to measure global contribution of input factors in dynamic models, Reliab. Eng. Syst. Saf. 99 (2011) 450–459". *Reliability Engineering & System Safety* **147** (2016), pp. 194–195.
- [109] S Xiao, S Oladyshkin & W Nowak. "Reliability sensitivity analysis with subset simulation: application to a carbon dioxide storage problem". In: *IOP Conference Series: Materials Science and Engineering*. Vol. 615. IOP Publishing, 2019, p. 012051.
- [110] D. B. Xiu. *Numerical methods for stochastic computations. A spectral method approach*. Princeton University Press, Princeton, NJ, 2010, pp. xiv+127.
- [111] C. Xu & G. Z. Gertner. "Uncertainty and sensitivity analysis for models with correlated parameters". *Reliability Engineering & System Safety* **93.10** (2008), pp. 1563–1573.
- [112] L. Yan, L. Guo & D. Xiu. "Stochastic Collocation Algorithms Using L1-minimization". *International Journal for Uncertainty Quantification* **2.3** (2012), pp. 279–293.
- [113] E. K. Yeagers, R. W. Shonkwiler & J. V. Herod. "The Biological Disposition of Drugs and Inorganic Toxins". In: *An Introduction to the Mathematics of Biology: with Computer Algebra Models*. Springer, 1996, pp. 194–233.
- [114] O. Zahm, P. G. Constantine, C. Prieur & Y. M. Marzouk. "Gradient-based dimension reduction of multivariate vector-valued functions". *SIAM Journal on Scientific Computing* **42.1** (2020), A534–A558.